



Doctoral Thesis

Computer Aided Diagnosis system for prostatic biopsy guidance and follow-up fusing multi-modal imaging

Guillaume Lemaître

November 2016



Doctoral Thesis

Computer Aided Diagnosis system for prostatic biopsy guidance and follow-up fusing multi-modal imaging

Guillaume Lemaître

Supervised by:

Jordi Freixenet Bosch (ViCOROB - UdG), Fabrice Mériadeau (CISIR - UTP)
Robert Marí Marly (ViCOROB - UdG), Paul Michael Walker (LE2I - UBFC)

November 2016

Doctorate in Technology

Work submitted to the Universitat de Girona and Université de Bourgogne Franche-Comté in partial fulfillment
of the requirements for the degree of Doctor of Philosophy

Reviewers:

Su Ruan, Professor at Université de Rouen - LITIS

Reyer Zwiggelaar Ir, Professor at Aberystwyth University - Vision, Graphics, and Visualisation Group

Soumya Ghose, Research Associate at Case Western Reserve University

Day of the defense: December 2016

Signature from head of PhD committee:

Abstract

Put your abstract or summary here, if your university requires it.

To ...

Acknowledgements

I would like to acknowledge the thousands of individuals who have coded for the LaTeX project for free. It is due to their efforts that we can generate professionally typeset PDFs now.

Publications

Peer-Review Journals Papers

1. **G. Lemaitre, R. Marti, M. Rastgoo, J. Massich, F. Freixenet, J. C. Vilanova, and F. Meriaudeau**, “Automatic prostate cancer detection through DCE-MRI images: all you need is a good normalization”, *Medical Image Analysis*, Submitted.
2. **G. Lemaitre, F. Nogueira, and C. Aridas**, “Imbalanced-learn: A Python Toolbox to Tackle the Curse of Imbalanced Datasets in Machine Learning”, *Journal of Machine Learning Research*, Submitted.
3. **G. Lemaitre, M. Rastgoo, J. Massich, C. Y. Cheung, T. Y. Wong, E. Lamoureux, D. Milea, F. Meriaudeau, and D. Sidibe**, “Classification of SD-OCT Volumes using Local Binary Patterns: Experimental Validation for DME detection”, *Journal of Ophthalmology*, vol. 2016, May 2016.
4. **G. Lemaitre, R. Marti, J. Freixenet, J. C. Vilanova, P. M. Walker, and F. Meriaudeau**, “Computer-Aided Detection and Diagnosis for prostate cancer based on mono and multi-parametric MRI: A Review”, *Computer in Biology and Medicine*, vol. 60, pp 8 - 31, 2015.

Peer-Review International Conferences

1. **G. Lemaitre, M. Rastgoo, J. Massich, J. C. Vilanova, P. M. Walker, J. Freixenet, A. Meyer-Baese, F. Meriaudeau, and R. Marti**, “Normalization of T2W-MRI prostate images using Rician a priori”, *SPIE Medical Imaging 2016*. San Diego: USA (February 2016).
2. **G. Lemaitre, M. Rastgoo, J. Massich, S. Sankar, F. Meriaudeau, and D. Sidibe**, “Classification of SD-OCT volumes with LBP: Application to DME detection”, *Ophthalmic Medical Image Analysis Workshop (OMIA), Medical Image Computing and Computer Assisted Interventions (MICCAI) 2015*. Munich: Germany (Oct. 2015).
3. **G. Lemaitre, J. Massich, R. Marti, J. Freixenet, J. C. Vilanova, P. M. Walker, D. Sidibe, and F. Meriaudeau**, “A Boosting Approach for Prostate Cancer Detection using Multi-parametric MRI”, *International Conference on Quality Control and Artificial Vision (QCAV) 2015*. Le Creusot: France (Jun. 2015).
4. **G. Lemaitre, A. Bikfalvi, J. Llach, J. Massich, and F. Julian**, “Business Model Design for University Technology Valorisation”, *International Technology, Education and Development Conference (INTED) 2015*. Madrid: Spain (Mar. 2015).

Thesis

1. **G. Lemaitre, A. Bikfalvi, and J. Llach**, “Valorisation of Computerized Technology in the Health Care Sector”, *Thesis for Master in Science Business Innovation and Technology Management (BITM)*, 2014.

Contributed Peer-Review Journals Papers

1. **K. Alsaih, G. Lemaitre, J. Massich, M. Rastgoo, D. Sidibe, and F. Meriaudeau**, “Machine Learning Techniques for DME Classification on SD-OCT images”, *BioMedical Engineering OnLine*, Submitted.
2. **I. P. Houben, P. Van de Voorde, C. R. Jeukens, J. E. Wildberger, G. Lemaitre, I. A. Illan, A. Meyer-Baese, L. F. Kooreman, M. L. Smidt, and M. B. Lobbes**, “Contrast-enhanced spectral mammography as work-up tool in patients recalled from breast cancer screening: risks versus benefits”, *European Radiology*, Submitted.
3. **D. Sidibe, S. Sankar, G. Lemaitre, M. Rastgoo, J. Massich, C. Y. Cheung, G. S. Tan, D. Milea, E. Lamoureux, T. Y. Wong, and F. Meriaudeau**, “An anomaly detection approach for the identification of DME patients using spectral domain optical coherence tomography images”, *Computer Methods and Programs in Biomedicine*, Submitted.
4. **M. Belkacemi, C. Stolz, A. Mathieu, G. Lemaitre, J. Massich, and O. Aubreton**, “Non Destructive Testing based on a Scanning-From-Heating approach: Application to non-through Defect Detection and Fiber Orientation Assessment”, *Journal of Electronic Imaging*, vol. 24(6), pp 1-8, Nov/Dec 2015.

Contributed Peer-Review International Conferences Papers

1. **J. Massich, M. Rastgoo, G. Lemaitre, C. Cheung, T. Y. Wong, D. Sidibe, and F. Meriaudeau**, “Classifying DME vs normal SD-OCT volumes: A review”, *23rd International Conference on Pattern Recognition (ICPR) 2016*. Cancun: Mexico (December 2016).
2. **K. Alsaih, G. Lemaitre, J. Massich, M. Rastgoo, D. Sidibe, T. Y. Wong, E. Lamoureux, D. Milea, C. Leung, and F. Meriaudeau**, “Classification of SD-OCT volumes with multi-pyramids, LBP and HoG descriptors: Application to DME detection”, *38th International Conference of the IEEE Engineering in Medicine and Biology Society (EMBC) 2016*. Orlando: USA (August 2016).
3. **A. Pampouchidou, K. Marias, M. Tsiknakis, P. Simos, F. Yang, G. Lemaitre, and F. Meriaudeau**, “Video-based depression detection using local curvelet binary patterns in pairwise orthogonal planes”, *38th International Conference of the IEEE Engineering in Medicine and Biology Society (EMBC) 2016*. Orlando: USA (August 2016).
4. **S. Hoffmann, M. Lobbes, I. Houben, K. Pinker-Domenig, G. Wengert, B. Burgeth, U. Meyer-Baese, G. Lemaitre, and A. Meyer-Baese**, “Computer-aided diagnosis of diagnostically challenging lesions in breast MRI: a comparison between a radiomics and a feature-selective approach”, *SPIE Commercial+ Scientific Sensing and Imaging*. Baltimore: USA (July 2016).

5. **M. Belkacemi, C. Stolz, A. Mathieu, G. Lemaitre, and O. Aubreton**, “A combined three-dimensional digitisation and subsurface defect detection data using active infrared thermography”, *13th Quantitative Infrared Thermography Conference (QIRT)*. Gdansk: Poland (July 2016).
6. **M. Belkacemi, J. Massich, G. Lemaitre, C. Stolz, V. Daval, G. Pot, O. Aubreton, R. Collet, and F. Meriaudeau**, “Wood fiber orientation assessment based on punctual laser beam excitation: A preliminary study”, *13th Quantitative Infrared Thermography Conference (QIRT)*. Gdansk: Poland (July 2016).
7. **M. Rastgoo, G. Lemaitre, J. Massich, O. Morel, F. Marzani, R. Garcia, and F. Meriaudeau**, “Study of Data Imbalancing for Melanoma Classification”, *3rd International Conference on BIOIMAGING*. Rome: Italy (February 2016).
8. **M. Rastgoo, G. Lemaitre, O. Morel, J. Massich, F. Marzani, R. Garcia, and D. Sidibe**, “Classification of melanoma lesions using sparse coded features and random forests”, *SPIE Medical Imaging 2016*. San Diego: USA (February 2016).
9. **A. Meyer-Baese, J. Massich, G. Lemaitre, and M. Rastgoo**, “Real-Time Optical Flow with Theoretically Justified Warping Applied to Medical Imaging”, *Breast Image Analysis Workshop (BIA), Medical Image Computing and Computer Assisted Interventions (MICCAI) 2015*. Munich: Germany (Oct. 2015).
10. **J. Massich, G. Lemaitre, J. Marti and F. Meriaudeau**, “An Optimization Approach to Segment Breast Lesions in Ultra-Sound Images using Clinically Validated Visual Cues”, *Breast Image Analysis Workshop (BIA), Medical Image Computing and Computer Assisted Interventions (MICCAI) 2015*. Munich: Germany (Oct. 2015).
11. **J. Massich, G. Lemaitre, J. Marti, and F. Meriaudeau**, “Brest Ultra-Sound image Segmentation: an Optimization approach based on super-pixels and high-level descriptors”, *International Conference on Quality Control and Artificial Vision (QCAV) 2015*. Le Creusot: France (Jun. 2015).

Contents

List of Abbreviations	x
List of Figures	xv
List of Tables	xvii
1 Introduction	1
1.1 Prostate anatomy	1
1.2 Prostate carcinoma	3
1.3 CaP screening and imaging techniques	4
1.4 CAD systems for CaP	6
1.5 Research motivations and objectives	7
1.6 Thesis outline	7
2 MRI Imaging Techniques	9
2.1 T ₂ -W MRI	9
2.2 T ₂ map	11
2.3 DCE-MRI	11
2.4 DW-MRI	14
2.5 ADC map	16
2.6 MRSI	17
2.7 Summary and conclusions	19
3 Review of CAD systems for CaP	21
3.1 Image regularization framework	26
3.1.1 Pre-processing	26

CONTENTS

3.1.1.1	MRI modalities	26
3.1.1.2	MRSI modality	34
3.1.1.3	Summary	40
3.1.2	Segmentation	40
3.1.2.1	Summary	44
3.1.3	Registration	44
3.2	Image classification framework	50
3.2.1	CADe: ROIs detection/selection	50
3.2.2	CADx: Feature detection	52
3.2.2.1	Image-based features	55
3.2.2.2	DCE-based features	60
3.2.2.3	MRSI-based features	63
3.2.3	CADx: Feature selection and feature extraction	64
3.2.3.1	Feature selection	65
3.2.3.2	Feature extraction	67
3.2.4	CADx: Classification	71
3.2.5	Model validation	84
3.2.6	Evaluation measure	85
3.3	Discussion	87
3.3.1	Results reported	87
3.3.2	Comparison	87
3.4	Conclusion	93
4	Materials	95
5	Normalization/Standardization of T2W-MRI and DCE-MRI Images	97
5.1	Normalization of T ₂ Weighted (T ₂ -W)-magnetic resonance imaging (MRI) images	97
5.1.1	Methodology	98
5.1.1.1	Normalization using Rician <i>a priori</i>	98
5.1.1.2	Normalization using generative models in functional data analysis	100

CONTENTS

5.1.2	Experiments and results	101
5.1.2.1	Experiments	101
5.1.2.2	Results	102
5.1.3	Discussion and conclusion	105
5.2	Normalization of dynamic contrast-enhanced (DCE)-MRI images . .	105
5.2.1	Methodology	107
5.2.1.1	Normalization of DCE-MRI images	107
5.2.1.2	Quantification of DCE-MRI	112
5.2.2	Experiment and results	117
5.2.2.1	Goodness of model fitting	118
5.2.2.2	Detection of CaP using pharmacokinetic parameters	119
5.2.2.3	Classification of the entire enhanced DCE-MRI signal	122
5.2.3	Discussion and conclusion	122
References		125

CONTENTS

List of Abbreviations

ACM active contour model

ADC apparent diffusion coefficient

AIF arterial input function

ASM active shape model

AUC area under the curve

BoW Bag of Words

BPH benign prostatic hyperplasia

CAD computer-aided detection and diagnosis

CADe computer-aided detection

CADx computer-aided diagnosis

CaP prostate cancer

CART classification and regression tree

CG central gland

Chap. Chapter

CMI combined mutual information

CSE chemical shift effect

CZ central zone

DCE dynamic contrast-enhanced

DCT discrete cosine transform

DFT discrete fourier transform

DNA deoxyribonucleic acid

DW diffusion weighted

EES extravascular-extracellular space

Eq. equation

ERSSPC European randomized study of screening for prostate cancer

ES Evolution Strategy

ETL echo train length

Fig. figure

FOV field of view

FROC free-response receiver operating characteristic

FSE Fast Spin-Echo

GLCM gray-level co-occurrence matrix

GS Gleason score

***g*-scale** generalized scale

ID3 iterative dichotomiser 3

***k*-CV** *k*-fold cross-validation

***k*-NN** *k*-nearest neighbour

LBP local binary pattern

LDA linear discriminant analysis

LLE locally linear embedding

LOOCV leave-one-out cross-validation

CONTENTS

LOPO CV leave-one-patient-out cross-validation

MANTRA multi-attribute non-initializing texture reconstruction based active shape model

MAP maximum *a posteriori*

MI mutual information

ML maximum likelihood

MLE maximum likelihood estimation

MP Matching Pursuit

mp-MRI multiparametric MRI

MRF Markov random field

MRI magnetic resonance imaging

mRMR minimum redundancy maximum relevance

MRSI magnetic resonance spectroscopy imaging

MSE mean squared error

NMR nuclear magnetic resonance

OMP Orthogonal Matching Pursuit

PCA principal components analysis

PDF probability density function

PLCO prostate lung colorectal and ovarian

PSA prostate-specific antigen

PUN phenomenological universalities

PZ peripheral zone

RBF radial basis function

RF random forest

RMS root mean square

RMSD root-mean-square deviation

ROC receiver operating characteristic

ROI region of interest

SCF sparse coded features

SE sensitivity

Sect. section

SI signal intensity

SNR signal-to-noise

SP Specificity

SRSF square-root slope function

STAPLE simultaneous truth and performance level estimation

SVD singular value decomposition

SVM support vector machines

T₁-W T₁ Weighted

T₂-W T₂ Weighted

Table table

TE echo time

TPS thin plate spline

CONTENTS

TR repetition time

TRUS transrectal ultrasound

TZ transitional zone

US ultrasound

WERITAS weighted ensemble of regional image textures for active shape model segmentation

List of Figures

1.1	Sagittal anatomy of prostate.	2
1.2	Prostate anatomy.	2
2.1	Rendering of T ₂ -W-MRI prostate images.	10
2.2	Enhancement of DCE-MRI signal.	12
2.3	Example of DW-MRI and DCE map.	14
2.4	Illustration of healthy and cancerous MRSI spectrum.	17
3.1	Common CAD framework based on MRI images used to detect CaP.	22
3.2	Illustration of a Gaussian and Rayleigh distributions.	27
3.3	Non-homogeneity artifacts due to perturbation of the endorectal coil.	29
3.4	Example of piecewise linear normalization as proposed in [186].	34
3.5	Illustration of the two organs used in [181, 182] to normalize T ₂ -W-MRI and T ₁ Weighted (T ₁ -W)-MRI images.	35
3.6	Illustration of phase malignant in an MRSI spectra.	36
3.7	Illustration of water and fat residues in magnetic resonance spectroscopy imaging (MRSI) signal after suppression during acquisition.	37
3.8	Illustration of frequency misalignment in a MRSI spectra.	39
3.9	Registration framework.	45
3.10	Difference observed in joint histogram between aligned and misaligned images.	47
3.11	Illustration of 4 different Gabor filters.	55
3.12	Semi-quantitative features used for DCE-MRI.	61
3.13	Representation of the probabilistic boosting-tree.	77

LIST OF FIGURES

3.14	Representation of a neural network of the multilayer perceptron family.	81
3.15	Representation of a neural network of the probabilistic neural network family.	82
3.16	Comparison in terms of FROC of the methods using data from 3 T MRI scanner.	88
3.17	Results comparison from the state-of-the-art in terms of AUC.	89
3.18	Comparison of the state-of-the-art results in terms of SE and SP.	90
5.1	Visual evaluation of the goodness of fitting using Rician and Gaussian distribution.	99
5.2	Qualitative evaluation by visual inspection of the alignment of the probability density function (PDF)s for the full prostate and the prostate cancer (CaP).	103
5.3	Spectral evaluation using principal components analysis (PCA) decomposition: (a) evaluation considering the full prostate, (b) evaluation considering only the CaP.	104
5.4	Illustration of the inter-patient variations in 17 different patients, using the PDF representation.	107
5.5	Illustration of the heatmap in DCE-MRI images.	108
5.6	Illustration of the estimator found using the shortest-path through the graph.	109
5.7	Illustration of the correction of the time offset and the data dispersion.	111
5.8	Illustration of the segmentation of the area used to determine the AIF.	113
5.9	ROC analysis using a RF classifier with and without normalization DCE-MRI data for different pharmacokinetic models.	119
5.10	ROC analysis using the entire DCE-MRI signal with and without normalization in conjunction with a RF classifier.	121

List of Tables

2.1	Overview of the features associated with each MRI modality used for medical diagnosis by radiologists.	20
3.1	Overview of the different studies reviewed with their main characteristics.	24
3.2	Overview of the pre-processing methods used in CAD systems. . . .	40
3.3	Overview of the segmentation methods used in computer-aided detection and diangosis (CAD) systems.	44
3.4	Classification of the different registration methods used in the CAD systems reviewed.	49
3.5	Overview of the CADe strategies employed in CAD systems. . . .	51
3.6	Overview of the feature detection methods used in CAD systems. .	53
3.7	The 14 statistical features used in conjunction with GLCM analysis. .	57
3.8	Parameters used as features for a DCE semi-quantitative analysis in CAD systems.	61
3.9	Overview of the feature selection and extraction methods used in CAD systems.	64
3.10	Overview of the classifiers used in CAD systems.	72
3.11	Overview of the model validation techniques used in CAD systems. .	84
3.12	Overview of the evaluation metrics used in CAD systems.	85
5.1	Coefficient of determination R^2 (i.e., μ ($\pm\sigma$)), while fitting data with the different quantification models.	118
5.2	AUC (i.e., μ ($\pm\sigma$)) for each individual pharmacokinetic parameter using a RF classifier.	120

LIST OF TABLES

Chapter 1

Introduction

1.1 Prostate anatomy

The prostate is an exocrine gland of the male reproductive system having an inverted pyramidal shape, which is located below the bladder and in front of the rectum as shown in Fig. 1.1. It measures approximately 3 cm in height by 2.5 cm in depth and its weight is estimated from 7 g to 16 g for an adult [134]. The prostate size increases at two distinct stages during physical development: initially at puberty to reach its normal size, then again after 60 years of age leading to benign prostatic hyperplasia (BPH) [195].

A zonal classification of the prostate has been suggested by McNeal [170], as depicted in Fig. 1.2. Subsequently, this categorization has been widely accepted in the literature [46, 105, 195, 286] and is used during all medical examinations (e.g., biopsy, magnetic resonance imaging (MRI) screening). The classification is based on dividing the gland into 3 distinct regions: (i) the central zone (CZ) accounting for 20 % to 25 % of the whole prostate gland, (ii) the transitional zone (TZ) standing for 5 %, and (iii) the peripheral zone (PZ) representing the 70 %. In MRI images, tissues of CZ and TZ are difficult to distinguish and are usually merged into a common region, denominated central gland (CG). As part of this classification, the prostate is divided into 3 longitudinal portions depicted in Fig. 1.2(b): (i) base, (ii) median gland, and (iii) apex.

1. INTRODUCTION

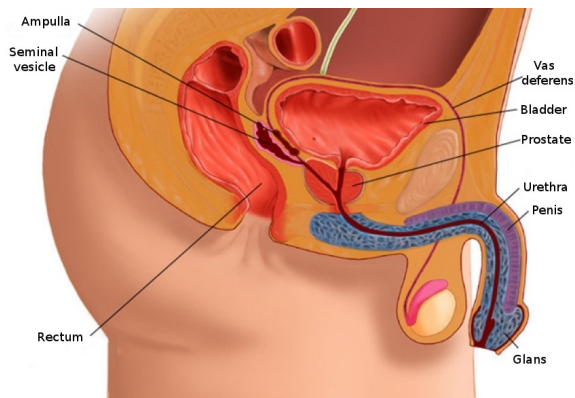
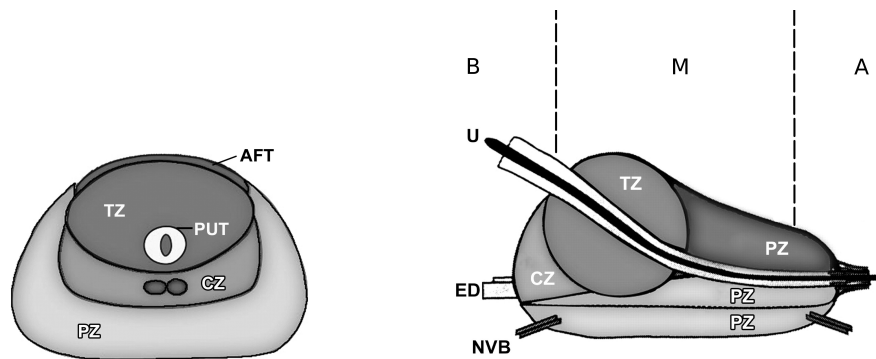


Figure 1.1: Sagittal anatomy scheme of the male reproductive system (copyright by [78]).



(a) Transverse anatomy of the prostate.

(b) Sagittal anatomy of the prostate.

Figure 1.2: Prostate anatomy with division in different zones. *AFT*: anterior fibromuscular tissue, *CZ*: central zone, *ED*: ejaculatory duct, *NVB*: neurovascular bundle, *PUT*: periurethral tissue, *PZ*: peripheral zone, *U*: urethra, *TZ*: transitional zone, *B*: base, *M*: median, *A*: apex (copyright by [43]).

1.2 Prostate carcinoma

Prostate cancer (CaP) has been reported on a worldwide scale to be the second most frequently diagnosed cancer of men accounting for 13.6 % [69]. Statistically, in 2008, the number of new diagnosed cases has been estimated to be 899,000 with no less than 258,100 deaths [69]. In United States, aside from skin cancer, CaP is declared to be the most commonly diagnosed cancer among men, implying that approximately 1 in 6 men will be diagnosed with CaP during their lifetime and 1 in 36 will die from this disease, causing CaP to be the second most common cause of cancer death among men [8, 241].

Despite active research to determine the causes of prostate cancer, a fuzzy list of risk factors has arisen [7]. The etiology has been linked to the following factors [7]: (i) family history [84, 252], (ii) genetic factors [1, 11, 72], (iii) race-ethnicity [84, 102], (iv) diet [5, 84, 161], and (v) obesity [84, 223]. This list of risk factors alone cannot be used to diagnose CaP and in this way, screening enables early detection and treatment.

CaP growth is characterized by two main types of evolution [253]: slow-growing tumours, accounting for up to 85 % of all CaPs [159], progress slowly and usually stay confined to the prostate gland. For such cases, treatment can be substituted with active surveillance. In contrast, the second variant of CaPs develops rapidly and metastasises from prostate gland to others organs, primarily the bones [189]. Bone metastases, being an incurable disease, significantly affects the morbidity and mortality rate [302]. Hence, the results of the surveillance have to be trustworthy in order to distinguish aggressive from slow-growing CaP.

CaP is more likely to come into being in specific regions of the prostate. In that respect, around 70 % to 80 % of CaPs originate in PZ whereas 10 % to 20 % in TZ [36, 171, 250]. Only about 5 % of CaPs occur in CZ [47, 171]. However, those cancers appear to be more aggressive and more likely to invade other organs due to their locations [47].

1. INTRODUCTION

1.3 CaP screening and imaging techniques

Current CaP screening consists of three different stages. First, prostate-specific antigen (PSA) control is performed to distinguish between low- and high-risk CaP. To assert such diagnosis, samples are taken during prostate biopsy and finally analyzed to evaluate the prognosis and the stage of CaP. In this section, we present a detailed description of the current screening as well as its drawbacks.

Since its introduction in mid-1980s, PSA is widely used for CaP screening [67]. A higher-than-normal level of PSA can indicate an abnormality of the prostate either as a BPH or a cancer [101]. However, other factors can lead to an increased PSA level such as prostate infections, irritations, a recent ejaculation, or a recent rectal examination [195]. PSA is found in the bloodstream in two different forms: free PSA accounting for about 10 % and linked to another protein for the remaining 90 %. A level of PSA higher than 10 ng mL^{-1} is considered to be at risk [195]. If the PSA level is ranging from 4 ng mL^{-1} to 10 ng mL^{-1} , the patient is considered as suspicious [17]. In that case, the ratio of free PSA to total PSA is computed; if the ratio is higher than 15 %, the case is considered as pathological [195].

A transrectal ultrasound (TRUS) biopsy is carried out for cases which are considered as pathological. At least 6 different samples are taken randomly from the right and left parts of the 3 different prostate zones: apex, median, and base. These samples are further evaluated using the Gleason grading system [86]. The scoring scheme to characterize the biopsy sample is composed of 5 different patterns which correspond to grades ranging from 1 to 5. A higher grade is associated with a poorer prognosis [66]. Then, in the Gleason system, 2 scores are assigned corresponding to (i) the grade of the most present tumour pattern, and (ii) the grade of the second most present tumour pattern [66]. A higher Gleason score (GS) indicates a more aggressive tumour [66]. Also, it should be noted that biopsy is an invasive procedure which can result in serious infection or urine retention [44, 94].

Although PSA screening has been shown to improve early detection of CaP [44], its lack of reliability motivates further investigations using MRI-based computer-aided detection and diagnosis (CAD). Two reliable studies — carried out in the United States [12] and in Europe [107, 236] — have attempted to assess the impact of early detection of CaP, with diverging outcomes [44, 98]. The study carried out

1.3 CaP screening and imaging techniques

in Europe¹ concluded that PSA screening reduces CaP-related mortality by 21 % to 44 % [107, 236], while the American² trial found no such effect [12]. However, both studies agree that PSA screening suffers from low specificity, with an estimated rate of 36 % [235]. Both studies also agree that over-treatment is an issue: decision making regarding treatment is further complicated by difficulties in evaluating the aggressiveness and progression of CaP [59].

Hence, new screening methods should be developed with improved specificity of detection as well as more accurate risk assessment (i.e., aggressiveness and progression). Current research is focused on identifying new biological markers to replace PSA-based screening [25, 28, 179]. Until such research comes to fruition, these needs can be met through active-surveillance strategy using multiparametric MRI (mp-MRI) techniques [101, 178]. An MRI-CAD system, which is an area of active research and forms the focus of this thesis, can be incorporated into this screening strategy allowing a more systematic and rigorous follow-up.

Another weakness of the current screening strategy lies in the fact that TRUS biopsy does not provide trustworthy results. Due to its “blind” nature, there is a chance of missing aggressive tumours or detecting microfocal “cancers”, which influences the aggressiveness-assessment procedure [183]. As a consequence, over-diagnosis is estimated at up to 30 % [91], while missing clinically significant CaP is estimated at up 35 % [258]. In an effort to solve both issues, alternative biopsy approaches have been explored. MRI/ultrasound (US)-guided biopsy has been shown to outperform standard TRUS biopsy [58]. There, mp-MRI images are fused with US images in order to improve localization and aggressiveness assessment to carry out biopsies. Human interaction plays a major role in biopsy sampling which can lead to low repeatability; by reducing potential human errors at this stage, the CAD framework can be used to improve repeatability of examination. CaP detection and diagnosis benefit from the use of CAD and MRI techniques.

In an effort to improve the current stage of CaP diagnosis and detection, this thesis is intended to provide a mp-MRI-CAD system. The different MRI modalities

¹The European randomized study of screening for prostate cancer (ERSSPC) started in the 1990s in order to evaluate the effect of PSA screening on mortality rate.

²The prostate lung colorectal and ovarian (PLCO) cancer screening trial is carried out in the United States and intends to ascertain the effects of screening on mortality rate.

1. INTRODUCTION

are presented in Chap. 2.

1.4 CAD systems for CaP

During the last century, physicists have focused on constantly innovating in terms of imaging techniques assisting radiologists to improve cancer detection and diagnosis. However, human diagnosis still suffers from low repeatability, synonymous with erroneous detection or interpretations of abnormalities throughout clinical decisions [83, 93]. These errors are driven by two major causes [83]: observer limitations (e.g., constrained human visual perception, fatigue or distraction) and the complexity of the clinical cases themselves, for instance due to imbalanced data — the number of healthy cases is more abundant than malignant cases — or overlapping structures.

Computer vision has given rise to many promising solutions, but, instead of focusing on fully automatic computerized systems, researchers have aimed at providing computer image analysis techniques to aid radiologists in their clinical decisions [83]. In fact, these investigations brought about both concepts of computer-aided detection (CADe) and computer-aided diagnosis (CADx) grouped under the acronym CAD. Since those first steps, evidence has shown that CAD systems enhance the diagnosis performance of radiologists. Chan et al. reported a significant 4 % improvement in breast cancer detection [38], which has been confirmed in later studies [57]. Similar conclusions have been drawn in the case of lung nodule detection [141], colon cancer [202], or CaP as well [93]. Chan et al. also hypothesized that CAD systems will be even more efficient assisting inexperienced radiologists than senior radiologists [38]. That hypothesis has been tested by Ham-brock et al. and confirmed in case of CaP detection [93]. In this particular study, inexperienced radiologists obtained equivalent performance to senior radiologists, both using CAD whereas the accuracy of their diagnosis was significantly poorer without CAD's help.

In contradiction with the aforementioned statement, CAD for CaP is a young technology due to the fact that it is based on a still young imaging technology: MRI [97]. Indeed, four distinct MRI modalities are employed in CaP diagnosis

which have been mainly developed after the mid-1990s: (i) T_2 Weighted (T_2 -W)-MRI [104], (ii) dynamic contrast-enhanced (DCE)-MRI [106], (iii) magnetic resonance spectroscopy imaging (MRSI) [126], and (iv) diffusion weighted (DW)-MRI [233]. In addition, the increase of magnetic field strength in clinical settings, from 1.5 T to 3 T, and the development of endorectal coils, both improved image spatial resolution [257] needed to perform more accurate diagnosis. It is for this matter that the development of CAD for CaP is still lagging behind the fields stated above.

The further chapters aim at first, to provide an overview of the current state-of-the-art of CAD for CaP and later, according to the drawn conclusions, to propose a CAD which takes advantages of mp-MRI modalities. A review of the current proposed CAD for CaP is presented in Chap. 3.

1.5 Research motivations and objectives

- Design and develop the first mp-MRI CAD system using all available MRI modalities.
- Pay particular attention to non investigated area: pre-processing.
- Open-source and open-data: acquire and make available the first mp-MRI dataset for prostate imaging and release source code.

1.6 Thesis outline

1. INTRODUCTION

Chapter 2

MRI Imaging Techniques

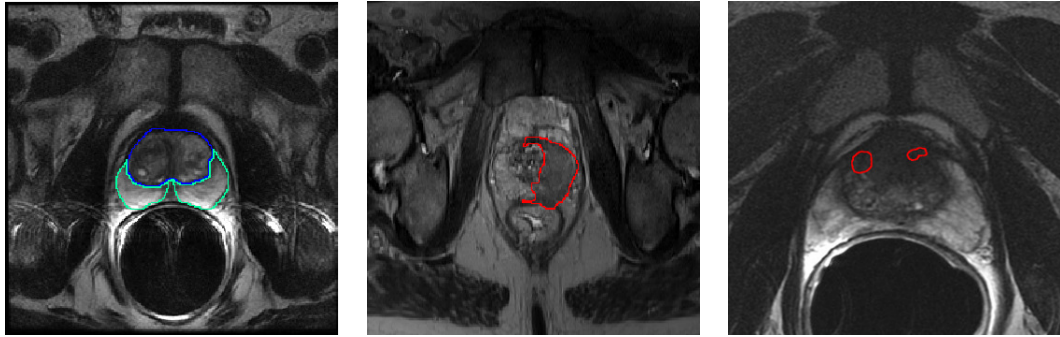
MRI provides promising imaging techniques to overcome the drawbacks of current clinical screening techniques mentioned in Sect. 1. Unlike TRUS biopsy, MRI examination is a non-invasive protocol and has been shown to be the most acute and harmless technique available currently [277]. In this section, we review different MRI imaging techniques developed for CaP detection and diagnosis. Features strengthening each modality will receive particular attention together with their drawbacks. Commonly, these features form the basis for developing analytic tools and automatic algorithms. However, we refer the reader to Sect. 3.2.2 for more details on automatic feature detection methods since they are part and parcel of the CAD framework.

2.1 T_2 -W MRI

T_2 -W-MRI has been the first MRI-modality used to perform CaP diagnosis using MRI [104]. Nowadays, radiologists make use of it for CaP detection, localization, and staging purposes. This imaging technique is well suited to render zonal anatomy of the prostate [17].

This modality relies on a sequence based on setting a long repetition time (TR), reducing the T_1 effect in nuclear magnetic resonance (NMR) signal measured, and fixing the echo time (TE) to sufficiently large values in order to enhance the T_2 effect of tissues. Thus, PZ and CG tissues are well perceptible in these images.

2. MRI IMAGING TECHNIQUES



(a) T₂-W-MRI slice of a healthy prostate acquire with a 1.5 T MRI with an endorectal coil. The blue contour represents the CG while the PZ corresponds to the green contour.

(b) T₂-W-MRI slice of a prostate with a CaP highlighted in the PZ using a 3 T MRI scanner without an endorectal coil.

(c) T₂-W-MRI slice of a prostate with a CaP highlighted in the CG using a 1.5 T MRI scanner with an endorectal coil.

Figure 2.1: Rendering of T₂-W-MRI prostate image with both 1.5 T and 3 T MRI scanner.

The former is characterized by an intermediate/high-signal intensity (SI) while the latter is depicted by a low-SI [105]. An example of a healthy prostate is shown in Fig. 2.1(a).

In PZ, round or ill-defined low-SI masses are synonymous with CaPs [104] as shown in Fig. 2.1(b). Detecting CaP in CG is more challenging. In fact both normal CG tissue and malignant tissue, have a low-SI in T₂-W-MRI, reinforcing difficulties to distinguish one among them. However, CaPs in CG appear often as homogeneous mass possessing ill-defined edges with lenticular or “water-drop” shapes [4, 17] as depicted in Fig. 2.1(c).

CaP aggressiveness has been shown to be inversely correlated with SI. Indeed, CaPs assessed with a GS of 4-5 implied lower SI than the one with a GS of 2-3 [299].

In spite of the availability of these useful and encouraging features, the T₂-W modality lacks reliability [101, 123]. Sensitivity is affected by the difficulties in detecting cancers in CG [123] while specificity rate is highly affected by outliers [17]. In fact, various conditions emulate patterns of CaP such as BPH, post-biopsy hemorrhage, atrophy, scars, and post-treatment [17, 53, 105, 213, 233]. These issues

are partly addressed using more innovative and advanced modalities.

2.2 T₂ map

As previously mentioned, T₂-W-MRI modality shows low sensitivity. Moreover, T₂-W-MRI images are a composite of multiple effects [97]. However, T₂ values alone have been shown to be more discriminative [156] and highly correlated with citrate concentration, a biological marker in CaP [147, 148].

T₂ values are computed using the characteristics of transverse relaxation which is formalized as in Eq. (2.1).

$$M_{x,y}(t) = M_{x,y}(0) \exp\left(-\frac{t}{T_2}\right) , \quad (2.1)$$

where $M_{x,y}(0)$ is the initial value of $M_{x,y}(t)$ and T_2 is the relaxation time.

By rearranging Eq. (2.1), T₂ map is computed by performing a linear fitting on the model presented in Eq. (2.2) using several TE, $t = \{TE_1, TE_2, \dots, TE_m\}$.

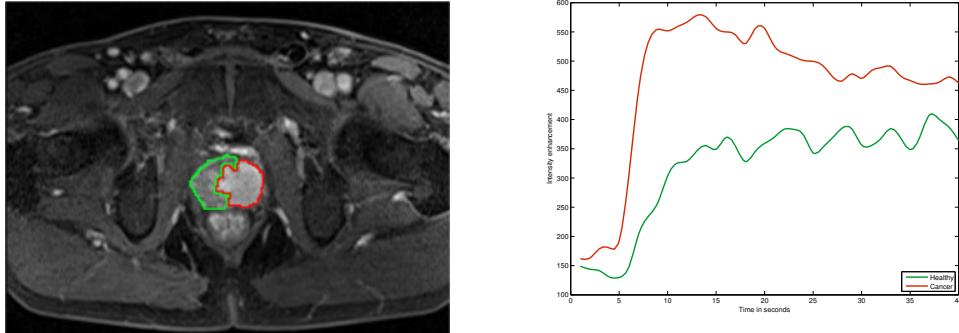
$$\ln\left[\frac{M_{x,y}(t)}{M_{x,y}(0)}\right] = -\frac{t}{T_2} . \quad (2.2)$$

The Fast Spin-Echo (FSE) sequence has been shown to be particularly well suited in order to build a T₂ map and obtain accurate T₂ values [146]. Similar to T₂-W-MRI, T₂ values associated with CaP are significantly lower than those of healthy tissues [82, 147].

2.3 DCE-MRI

DCE-MRI is an imaging technique which exploits the vascularity characteristic of tissues. Contrast media, usually gadolinium-based, is injected intravenously into the patient. The media extravasates from vessels to extravascular-extracellular space (EES) and is released back into the vasculature before being eliminated by the kidneys [89]. Furthermore, the diffusion speed of the contrast agent may vary due to several parameters: (i) the permeability of the micro-vessels, (ii) their surface area, and (iii) the blood flow [193].

2. MRI IMAGING TECHNIQUES



(a) T₁-W-MRI image where the cancer is delimited by the red contour. The green area was still not invaded by the CaP

(b) Enhancement curve computed during the DCE-MRI analysis. The red curve is typical from CaP cancer while the green curve is characteristic of healthy tissue.

Figure 2.2: Illustration of typical enhancement signal observed in DCE-MRI analysis collected with a 3 T MRI scanner.

Healthy PZ is mainly made up of glandular tissue, around 70 % [43], which implies a reduced interstitial space restricting exchanges between vessels and EES [31, 279]. Normal CG has a more disorganized structure, composed of mainly fibrous tissue [43, 101], which facilitates the arrival of the contrast agent in EES [280]. To understand the difference between contrast media kinetic in malignant tumours and the two previous behaviours mentioned, one has to focus on the process known as angiogenesis [35]. In order to ensure growth, malignant tumours produce and release angiogenic promoter substances [35]. These molecules stimulate the creation of new vessels towards the tumour [35]. However, the new vessel networks in tumours differ from those present in healthy tissue [89]. They are more porous due to the fact that their capillary walls have a large number of “openings” [43, 89]. In contrast to healthy cases, this increased vascular permeability results in increased contrast agent exchanges between vessels and EES [284].

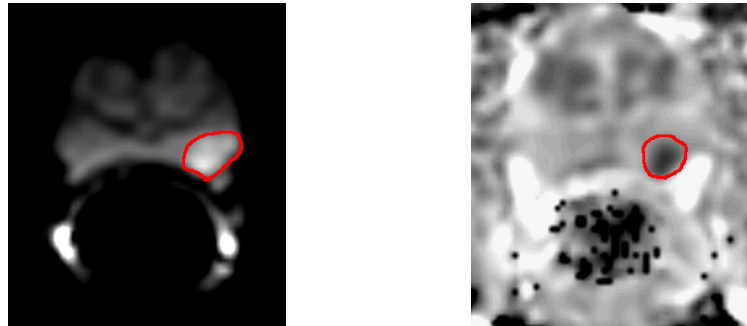
By making use of the previous aspects, DCE-MRI is based on an acquisition of a set of T₁ Weighted (T₁-W)-MRI images over time. The gadolinium-based contrast agent shortens T₁ relaxation time enhancing contrast in T₁-W-MRI images. The aim is to post-analyze the pharmacokinetic behaviour of the contrast media concentration in prostate tissues [284]. The image analysis is carried out in two

dimensions: (i) in the spatial domain on a pixel-by-pixel basis and (ii) in the time domain corresponding to the consecutive images acquired with the MRI. Thus, for each spatial location, a signal linked to contrast media concentration is measured as shown in Fig. 2.2(b) [268].

By taking the above remarks into account, CaPs is characterized by a signal having an earlier and faster enhancement and an earlier wash-out — i.e, the rate of the contrast agent flowing out of the tissue — as shown in Fig. 2.2(b) [284]. Three different approaches exist to analyze these signals with the aim of labelling them as corresponding to either normal or malignant tissues.

Qualitative analysis is based on a qualitative assessment of the signal shape [101]. Quantitative approaches consist of inferring pharmacokinetic parameter values [268]. Those parameters are part of mathematical-pharmacokinetic models which are directly based on physiological exchanges between vessels and EES. Several pharmacokinetic models have been proposed such as the Kety model [120], the Tofts model [269], and mixed models [129, 249]. The last family of methods mixed both approaches and are grouped together under the heading of semi-quantitative methods. They rely on shape characterization using mathematical modelling to extract a set of parameters such as wash-in gradient, wash-out, integral under the curve, maximum signal intensity, time-to-peak enhancement, and start of enhancement [101, 284]. These parameters are depicted in Fig. 3.12. It has been shown that semi-quantitative and quantitative methods improve localization of CaP when compared with qualitative methods [224]. Sect. 3.2.2.2 provides a full description of quantitative and semi-quantitative approaches.

DCE-MRI combined with T₂-W-MRI has shown to enhance sensitivity compared to T₂-W-MRI alone [113, 122, 234, 303]. Despite this fact, DCE-MRI possesses some drawbacks. Due to its “dynamic” nature, patient motions during the image acquisition lead to spatial mis-registration of the image set [284]. Furthermore, it has been suggested that malignant tumours are difficult to distinguish from prostatitis located in PZ and BPH located in CG [101, 284]. These pairs of tissues tend to have similar appearances. Later studies have shown that CaPs in CG do not always manifest in homogeneous fashion. Indeed, tumours in this zone can present both hypo-vascularization and hyper-vascularization which illustrates the challenge of CaP detection in CG [280].



(a) DW-MRI image acquired with a 1.5 T MRI scanner. The cancer corresponds to the high SI region highlighted in red.

(b) ADC map computer after acquisition of DW-MRI images with 1.5 T MRI scanner. The cancer corresponds to the low SI region highlighted in red.

Figure 2.3: Illustration of DW-MRI and ADC map. The signal intensity corresponding to cancer are inversely correlated on these modalities.

2.4 DW-MRI

As previously mentioned in the introduction, DW-MRI is the most recent MRI imaging technique aiming at CaP detection and diagnosis [233]. This modality exploits the variations in the motion of water molecules in different tissues [125, 132].

The distinction between healthy and CaP in DW-MRI is based on the following physiological bases. On the one hand, PZ, as previously mentioned, is mainly a glandular and tubular structure allowing water molecules to move freely [43, 101]. On the other hand, CG is made up of muscular or fibrous tissue causing the motion of the water molecules to be more constrained and heterogeneous than in PZ [101]. Then, CaP growth leads to the destruction of normal glandular structure and is associated with an increase in cellular density [101, 125, 245]. Furthermore, these factors both have been shown to be inversely correlated with water diffusion [125, 245]: higher cellular density implies a restricted water diffusion. Thus, water diffusion in CaP will be more restricted than both healthy PZ and CG [101, 125].

From the NMR principle side, DW-MRI sequence produces contrasted images due to variation of water molecules motion. The method is based on the fact that the signal in DW-MRI images is inversely correlated to the degree of random motion of water molecules [110]. In fact, gradients are used in DW MRI modality to encode spatial location of nuclei temporarily. Simplifying the problem in only one direction, a gradient is applied in that direction, dephasing the spins of water nuclei. Hence, the spin phases vary along the gradient direction depending of the gradient intensity at those locations. Then, a second gradient is applied aiming at cancelling the spin dephasing. Thus, the immobile water molecules will be subject to the same gradient intensity as the initial one while moving water molecules will be subject to a different gradient intensity. Thus, spins of moving water molecules will stay dephased whereas spins of immobile water molecules will come back in phase. As a consequence, a higher degree of random motion results in a more significant signal loss whereas a lower degree of random motion is synonymous with lower signal loss [110]. Under these conditions, the MRI signal is measured as:

$$M_{x,y}(t, b) = M_{x,y}(0) \exp\left(-\frac{t}{T_2}\right) S_{\text{ADC}}(b) , \quad (2.3)$$

$$S_{\text{ADC}}(b) = \exp(-b \times \text{ADC}) , \quad (2.4)$$

where S_{ADC} refers to signal drop due to diffusion effect, ADC is the apparent diffusion coefficient, and b is the attenuation coefficient depending only on the gradient pulses parameters: (i) gradient intensity and (ii) gradient duration [131].

By using this formulation, image acquisition with a parameter b equal to 0 s mm^{-2} corresponds to a T_2 -W-MRI acquisition. Then, increasing the attenuation coefficient b — i.e., increase gradient intensity and duration — enhances the contrast in DW-MRI images.

To summarize, in DW-MRI images, CaPs are characterized by high-SI compared to normal tissues in PZ and CG as shown in Fig. 2.3(a) [17]. However, some tissues in CG can look similar to CaP with higher SI [17].

Diagnosis using DW-MRI combined with T_2 -W-MRI has shown a significant improvement compared with T_2 -W-MRI alone and provides highly contrasted images [43, 194, 240]. As drawbacks, this modality suffers from poor spatial resolution

2. MRI IMAGING TECHNIQUES

and specificity due to false positive detection [43]. With a view to eliminate these drawbacks, radiologists use quantitative maps extracted from DW-MRI, which is presented in the next section.

2.5 ADC map

The NMR signal measured for DW-MRI images is not only affected by diffusion as shown in Eq. (2.3). However, the signal drop — Eq. (2.4) — is formulated such that the only variable is the acquisition parameter b [131]. The ADC is considered as a “pure” diffusion coefficient and is extracted to build a quantitative map known as the ADC map. From Eq. (2.3), it is clear that performing multiple acquisitions only varying b will not have any effect on the term $M_{x,y}(0) \exp\left(-\frac{t}{T_2}\right)$. Thus, Eq. (2.3) can be rewritten as:

$$S(b) = S_0 \exp(-b \times \text{ADC}) . \quad (2.5)$$

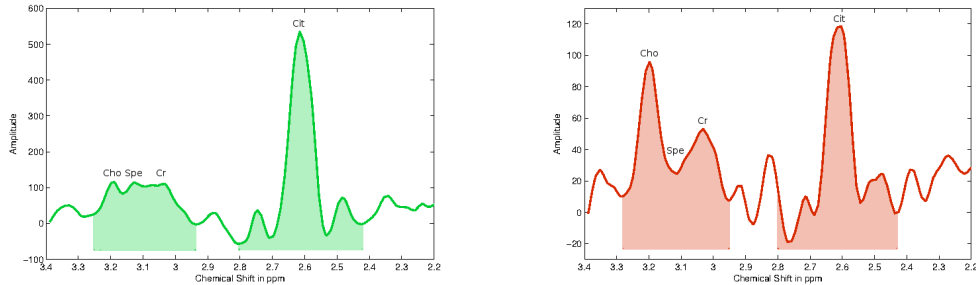
To compute the ADC map, a minimum of two acquisitions are necessary: (i) for b equal to 0 s mm^{-2} where the measured signal is equal to S_0 , and (ii) b_1 greater than 0 s mm^{-2} , typically 1000 s mm^{-2} . Then, the ADC map can be computed as:

$$\text{ADC} = -\frac{\ln\left(\frac{S(b_1)}{S_0}\right)}{b_1} . \quad (2.6)$$

More accurate ADC map are computed by acquiring a set of images with different values for the parameter b and fitting linearly a semi-logarithm function using the model presented in Eq. (2.5).

Regarding the appearance of the ADC maps, it has been previously stated that by increasing the value of b , the signal of CaP tissue increases significantly. Considering Eq. (2.6), the tissue appearance in the ADC map is the inverse of DW-MRI images. Then, CaP tissue is associated with low-SI whereas healthy tissue appears brighter as depicted in Fig. 2.3(b) [17].

Similar to the gain achieved by DW-MRI, diagnosis using ADC map combined with T_2 -W-MRI significantly outperforms T_2 -W-MRI alone [43, 62]. Moreover, it has been shown that ADC coefficient is correlated with GS [92, 112, 201].



(a) Illustration of an MRSI spectrum of a healthy voxel acquired with a 3 T MRI.

(b) Illustration of an MRSI spectrum of a cancerous voxel acquired with a 3 T MRI.

Figure 2.4: Illustration of an MRSI spectrum both healthy and cancerous voxel with a 3 T MRI. The highlighted areas corresponds to the related concentration of the metabolites which is computed by integrating the area under each peak. Acronyms: choline (Cho), spermine (Spe), creatine (Cr) and citrate (Cit).

However, some tissues of the CG mimic CaP with low-SI [123] and image distortion can arise due to hemorrhage [43]. It has also been noted that a high variability of the ADC occurs between different patients making it difficult to define a static threshold to distinguish CaP from non-malignant tumours [43].

2.6 MRSI

CaP induces metabolic changes in the prostate compared with healthy tissue. Thus, CaP detection can be carried out by tracking changes of metabolite concentration in prostate tissue. MRSI is an NMR-based technique which generates spectra of relative metabolite concentration in a region of interest (ROI).

In order to track changes of metabolite concentration, it is important to know which metabolites are associated with CaP. To address this question, clinical studies identified three biological markers: (i) citrate, (ii) choline, and (iii) polyamines composed mainly of spermine, and in less abundance of spermidine and putrescine [16, 52, 85].

Citrate is involved in the production and secretion of the prostatic fluid, and the glandular prostate cells are associated with a high production of citrate enabled

2. MRI IMAGING TECHNIQUES

by zinc accumulation by these same cells [52]. However, the metabolism allowing the accumulation of citrate requires a large amount of energy [52]. In contrast, malignant cells do not have high zinc levels leading to lower citrate levels due to citrate oxidization [52]. Furthermore, this change results in a more energy-efficient metabolism enabling malignant cells to grow and spread [52].

An increased concentration of choline is related to CaP [16]. Malignant cell development requires epigenetic mechanisms resulting in metabolic changes and relies on two mechanisms: deoxyribonucleic acid (DNA) methylation and phospholipid metabolism which both result in choline uptake, explaining its increased level in CaP tissue [16]. Spermine is also considered as a biological marker in CaP [85, 278]. In CaP, reduction of the ductal volume due to shifts in polyamine homeostasis might lead to a reduced spermine concentration [278].

To determine the concentration of these biological markers, one has to focus on the MRSI modality. In theory, in presence of a homogeneous magnetic field, identical nuclei precesses at the same operating frequency known as the Larmor frequency [90]. However, MRSI is based on the fact that identical nuclei will slightly precess at different frequencies depending on the chemical environment in which they are immersed [90], a phenomenon known as the chemical shift effect (CSE) [195]. Given this property, metabolites are identified and their concentrations are determined. In this regard, the Fourier transform is used to obtain the frequency spectrum of the NMR signal [90, 195]. In this spectrum, each peak is associated with a particular metabolite and the area under each peak corresponds to the relative concentration of this metabolite, as illustrated in Fig. 2.4 [195].

Two different quantitative approaches are used to decide whether or not the spectra of a ROI is associated with CaP: (i) relative quantification or (ii) absolute quantification [135]. In relative quantification, the ratio of choline-polyamines-creatine to citrate is computed. The integral of the signal is computed from choline to creatine — i.e., from 3.21 ppm to 3.02 ppm — because the peaks in this region can be merged at clinical magnetic field strengths [101, 278], as depicted in Fig. 2.4. Considering the previous assumptions that choline concentration rises and citrate concentration decreases in the presence of CaP, the ratio computed should be higher in malignant tissue than in healthy tissue.

In contrast with relative quantification, absolute quantification measures molar concentrations by normalizing relative concentrations using water as reference [135]. In this case, “true” concentrations are directly used to differentiate malignant from healthy tissue. However, this method is not commonly used as it requires an additional step of acquiring water signals, inducing time and cost acquisition constraints.

MRSI allows examination with high specificity and sensitivity compared to other MRI modalities [43]. Furthermore, it has been shown that combining MRSI with MRI improves detection and diagnosis performance [116, 232, 285]. Citrate and spermine concentrations are inversely correlated with the GS allowing us to distinguish low- from high- grade CaPs [85]. However, choline concentration does not provide the same properties [85].

Unfortunately, MRSI also presents several drawbacks. First, MRSI acquisition is time consuming which prevents this modality from being used in daily clinical practise [17]. In addition, MRSI suffers from low spatial resolution due to the fact that signal-to-noise (SNR) is linked to the voxel size. However, this issue is addressed by developing new scanners with higher magnetic field strengths such as 7.5 T [85]. Finally, a high variability of the relative concentrations between patients has been observed [43]. The same observation has been made depending on the zones studied (ie., PZ, CG, base, mid-gland, apex) [135, 298]. Due to this variability, it is difficult to use a fixed thresholds in order to differentiate CaP from healthy tissue.

2.7 Summary and conclusions

Table 2.1 provides an overview of the different modalities presented in the previous section. Indeed, each MRI modality alone provides different discriminative level to distinguish CaP from healthy tissue. A recurrent statement in the literature is, however, the ability to combine these MRI modalities which lead to the best diagnosis performance. In this regard, we will present in the next chapter automatic tools which have been developed to design mp-MRI CAD systems for the detection of CaP.

Table 2.1: Overview of the features associated with each MRI modality used for medical diagnosis by radiologists. Acronyms: prostate cancer (CaP) - signal intensity (SI) - Gleason score (GS).

Modality	Significant features	CaP	Healthy tissue	GS correlation
T ₂ -W-MRI	SI	low-SI in PZ [105]	intermediate to high-SI in PZ [105]	+ [299]
	Shape	round or ill-defined mass in PZ [104]		0
	SI	low-SI in CG [4, 17]	low-SI in CG [4, 17]	0
	Shape	homogeneous mass with ill-defined edges in CG [4, 17]		0
T ₂ map	SI	low-SI [82, 147]	intermediate to high-SI [82, 147]	+ [147, 148, 156]
DCE MRI	Semi-quantitative features [284]:			
	• wash-in	faster	slower	0
	• wash-out	faster	slower	0
	• integral under the curve	higher	lower	0
	• maximum signal intensity	higher	lower	0
	• time-to-peak enhancement	faster	slower	0
	Quantitative features (Tofts' parameters [268]):			
	• k _{ep}	higher	lower	0
	• K ^{trans}	higher	lower	0
DW MRI	SI	higher-SI [17, 110]	lower-SI [17, 110]	+
ADC map	SI	low-SI [17]	high-SI [17]	+ [92, 112, 201]
MRSI	Metabolites:			
	• citrate (2.64 ppm) [283]	lower concentration [16, 52, 278]	higher concentration [16, 52, 278]	+ [85]
	• choline (3.21 ppm) [283]	higher concentration [16, 52, 278]	lower concentration [16, 52, 278]	0 [85]
	• spermine (3.11 ppm) [283]	lower concentration [16, 52, 278]	higher concentration [16, 52, 278]	+ [85]

Notes:

+ = significantly correlated;

0 = no correlation.

Chapter 3

Review of CAD systems for CaP

As previously mentioned Sect. 1.4, CADs are developed to advise and backup radiologists in their tasks of CaP detection and diagnosis, but not to provide fully automatic decisions [83]. CADs can be divided into two different sub-groups: either as CADe, with the purpose to highlight probable lesions in MRI images, or CADx, which focuses on differentiating malignant from non-malignant tumours [83]. Moreover, an intuitive approach, motivated by developing a framework combining detection-diagnosis, is to mix both CADe and CADx by using the output of the former mentioned as a input of the latter named. Although the outcomes of these two systems should differ, the framework of both CAD systems is similar. A general CAD work-flow is presented in Fig. 3.1.

MRI modalities mentioned in Chap. 2 are used as inputs of CAD for CaP. These images acquired from the different modalities show a large variability between patients: the prostate organ can be located at different positions in images — due to patient motion, variation of acquisition plan — and the SI can be corrupted with noise or artifacts during the acquisition process caused by the magnetic field non-homogeneity or the use of endorectal coil. To address these issues, the first stage of CAD is to pre-process mp-MRI images to reduce noise, remove artifacts, and standardize the SI. Subsequently, most of the later processes are only focusing on the prostate organ; therefore it is necessary to segment the prostate in each MRI modality to define it as a ROI. However, data may suffer from misalignment due to patient motions or different acquisition parameters. Therefore, a registration step is usually performed so that all the previously segmented MRI images are in the

3. REVIEW OF CAD SYSTEMS FOR CAP

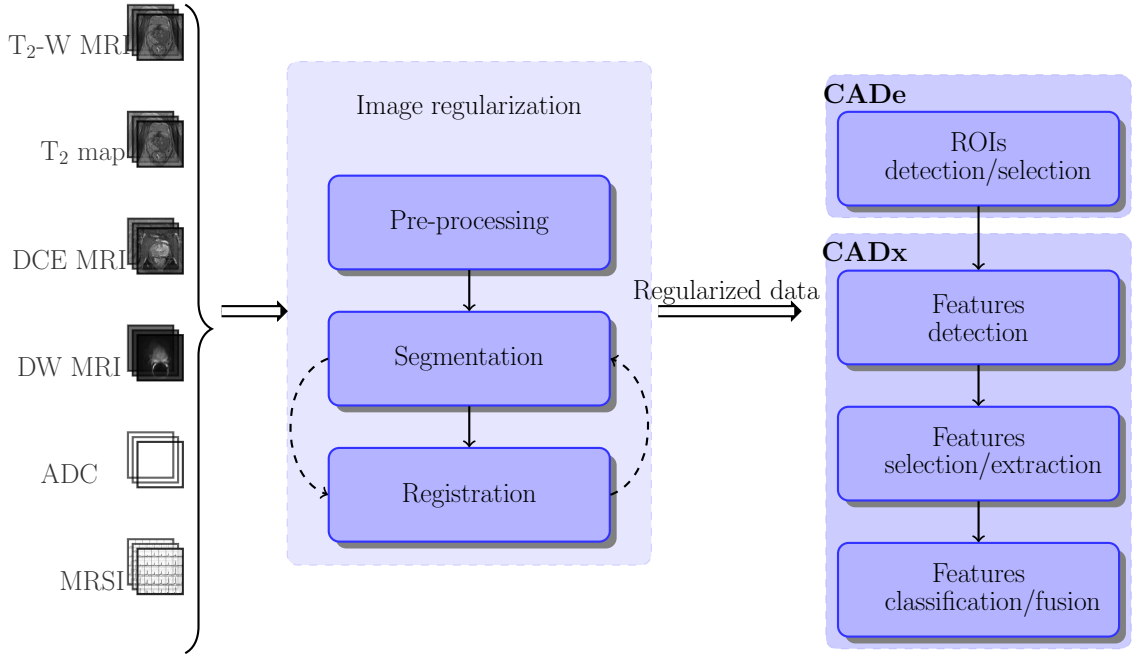


Figure 3.1: Common CAD framework based on MRI images used to detect CaP.

same reference frame. Registration and segmentation can be swapped depending on the strategy chosen.

Some studies do not fully apply the methodology depicted in Fig. 3.1. Details about those can be found in Table 3.1. Some studies bypass the pre-processing stages to prove the robustness of their approaches to noise or other artifacts, by using directly the raw data as inputs of their CAD systems. In some cases, prostate segmentation is performed manually as well as registration. Sometimes, it is also assumed that no patient motions occur during the acquisition procedure, removing the need of registering the mp-MRI images.

Once the data are regularized, it becomes possible to extract features and classify the data to obtain either the location of possible lesions (i.e., CADe) or/and the malignancy nature of these lesions (i.e., CADx).

In a CADe framework, *possible lesions are segmented automatically* and further used as input of a CADx. Nevertheless, some works also used a fusion of CADe-CADx framework in which a voxel-based features are directly used, in which the location of the malignant lesions are obtained as results. On the other hand,

manual lesions segmentation are not considered to be part of CADe. The output of the CADe is used as input of the CADx.

CADx is composed of the processes allowing to *distinguish malignant from non-malignant tumours*. Here, CaP malignancy is defined using the grade of the GS determined after post biopsy or prostatectomy. As presented in Fig. 3.1, CADx is usually composed of the three common steps used in a classification framework: (i) features detection, (ii) feature extraction/selection, and (iii) feature classification.

This chapter is organized using the methodology presented in Fig. 3.1. Methods embedded in the image regularization framework are presented initially to subsequently focus on the image classification framework, being divided into CADe and CADx. Finally, we present a summary of the results reported in the state-of-the-art as well as a discussion that follows. Table 3.1 summarizes the 56 different CAD studies reviewed in this section. The first set of information reported is linked to the data acquisition such as the number of patients included in the study, the modalities acquired as well as the strength of the field of the scanner used. Subsequently, information about the prostate zones considered in the CAD analysis — i.e. PZ or CG — are reported since that detecting CaP in the CG is a more challenging problem and has received particular attention only in the recent publications.

Table 3.1: Overview of the different studies reviewed with their main characteristics. Acronyms: number (#) - image regularization (Reg.). Notes: **X**: not used or not implemented; **✓[!]**: partially implemented; **✓**: used or implemented.

Index	Study	#	MRI-modality				Strength of field		Studied zones		CAD stages			
			Cases	T ₂ -W	DCE	DW	MRSI	1.5 T	3 T	PZ	CG	Reg.	CADe	CADx
[9, 10]	Ampeliotis et al.	25	✓	✓	✗	✗	✗	✓	✗	✓	✗	✓ [!]	✗	✓
[13]	Antic et al.	53	✓	✗	✓	✓	✗	✓	✗	✓	✓	✗	✗	✓
[14]	Artan et al.	10	✓	✓	✓	✓	✗	✓	✗	✓	✗	✗	✓	✓
[15]	Artan et al.	21	✓	✓	✓	✓	✗	✓	✗	✓	✗	✓ [!]	✓	✓
[33, 34]	Cameron et al.	5/13	✓	✗	✓	✓	✗	✗	✓	✓	✓	✗	✓	✓
[39]	Chan et al.	15	✓	✗	✓	✓	✗	✓	✗	✓	✗	✗	✗	✓
[45]	Chung et al.	20	✓	✗	✓	✓	✗	✗	✓	✓	✓	✗	✓	✓
[80, 81]	Giannini et al.	10/56	✓	✓	✓	✓	✗	✓	✗	✓	✗	✓	✓	✓
[119]	Kelm et al.	24	✗	✗	✗	✗	✓	✓	✗	✓	✓	✓ [!]	✓	✓
[121]	Khavati et al.	20	✓	✗	✓	✓	✗	✗	✓	✓	✓	✗	✓	✓
[127]	Langer et al.	25	✓	✓	✓	✓	✗	✓	✗	✓	✗	✓ [!]	✗	✓
[133]	Lehaire et al.	35	✓	✓	✓	✓	✗	✓	✗	✓	✗	✓ [!]	✗	✓
[153]	Litjens et al.	188	✓	✓	✓	✓	✗	✗	✓	✓	✗	✓ [!]	✓	✓
[154]	Litjens et al.	288	✓	✓	✓	✓	✗	✗	✓	✓	✓	✓ [!]	✓	✓
[151]	Litjens et al.	347	✓	✓	✓	✓	✗	✗	✓	✓	✓	✓ [!]	✓	✓
[157]	Liu et al.	11	✓	✓	✓	✓	✗	✓	✗	✓	✗	✓ [!]	✓	✓
[155]	Liu et al.	54	✓	✓	✓	✓	✗	✗	✓	✓	✓	✓ [!]	✗	✓
[158]	Lopes et al.	27	✓	✗	✗	✗	✗	✓	✗	✓	✗	✓ [!]	✓	✓
[160]	Lv et al.	55	✓	✗	✗	✗	✗	✓	✗	✓	✗	✓ [!]	✗	✓
[168]	Matulewicz et al.	18	✗	✗	✗	✗	✓	✗	✓	✓	✓	✗	✓	✓
[169]	Mazzetti et al.	10	✗	✓	✗	✗	✗	✓	✗	✓	✗	✓ [!]	✓	✓
[181, 182]	Niaf et al.	23/30	✓	✓	✓	✓	✗	✓	✗	✓	✗	✓ [!]	✗	✓

[191, 192]	Ozer et al.	20	✓	✓	✓	✗	✓	✗	✓	✗	✓ [!]	✓	✓
[196]	Parfait et al.	22	✗	✗	✗	✓	✗	✓	✓	✓	✓ [!]	✓	✓
[201]	Peng et al.	48	✓	✓	✓	✗	✗	✓	✓	✓	✓	✗	✓
[209]	Puech et al.	100	✗	✓	✗	✗	✓	✗	✓	✓	✓	✗	✓
[215, 217]	Rampun et al.	45	✓	✗	✗	✗	✓	✗	✓	✗	✗	✓	✓
[215, 218, 219]	Rampun et al.	45	✓	✗	✗	✗	✓	✗	✓	✗	✗	✓	✓
[230]	Samarasinghe et al.	40	✗	✓	✗	✗	✗	✓	✓	✓	✓ [!]	✗	✓
[256]	Sung et al.	42	✗	✓	✗	✗	✗	✓	✓	✓	✓	✗	✓
[261]	Tiwari et al.	14	✗	✗	✗	✓	✓	✗	✓	✓	✓ [!]	✓	✓
[262]	Tiwari et al.	18	✗	✗	✗	✓	✓	✗	✓	✓	✓ [!]	✓	✓
[263]	Tiwari et al.	18	✗	✗	✗	✓	✓	✗	✓	✓	✓ [!]	✓	✓
[264]	Tiwari et al.	15	✓	✗	✗	✓	✓	✗	✓	✓	✓ [!]	✓	✓
[265]	Tiwari et al.	19	✓	✗	✗	✓	✓	✗	✓	✓	✓ [!]	✓	✓
[266]	Tiwari et al.	36	✓	✗	✗	✓	✓	✗	✓	✓	✓	✗	✓
[267]	Tiwari et al.	29	✓	✗	✗	✓	✓	✗	✓	✓	✓ [!]	✓	✓
[273, 274]	Trigui et al.	34	✓	✓	✓	✓	✓	✗	✓	✓	✓ [!]	✓	✓
[289]	Viswanath et al.	16	✓	✗	✗	✓	✓	✗	✓	✓	✓	✗	✓
[288]	Viswanath et al.	6	✓	✓	✗	✗	✗	✗	✓	✓	✓ [!]	✓	✓
[290]	Viswanath et al.	6	✓	✓	✓	✗	✗	✗	✓	✓	✓	✓	✓
[291]	Viswanath et al.	12	✓	✓	✓	✓	✗	✗	✓	✓	✓ [!]	✓	✓
[292]	Viswanath et al.	22	✓	✗	✗	✗	✗	✗	✓	✓	✓	✓	✓
[293]	Vos et al.	29	✓	✓	✓	✗	✗	✓	✓	✓	✓ [!]	✗	✓
[294]	Vos et al.	29	✗	✓	✗	✗	✓	✓	✓	✓	✓ [!]	✗	✓
[295]	Vos et al.	29	✓	✓	✗	✗	✓	✗	✓	✓	✓ [!]	✗	✓
[296]	Vos et al.	NA	✓	✓	✓	✗	✗	✓	✓	✓	✓ [!]	✓	✓

3.1 Image regularization framework

This section provides a review of the methods used in CADs for CaP in order to *regularize* the mp-MRI images. At first, we present the pre-processing methods in Sect. 3.1.1, focusing mainly on the denoising and artefacts removal methods as well as standardization of SI. Section 3.1.2 and Sect. 3.1.3 summarize the segmentation and registration methods, which are processes allowing the CAD to only operate on the prostate organ and ensuring that the mp-MRI images are aligned in the same reference frame.

3.1.1 Pre-processing

Three different groups of pre-processing methods are commonly applied to images as initial stage in CADs for CaP. These methods are explained for both MRI and MRSI modalities.

3.1.1.1 MRI modalities

Noise filtering The NMR signal, measured and acquired in the k-space, is affected by noise. This noise obeys a complex Gaussian white noise mainly due to thermal noises in the patient [184]. Furthermore, MRI images visualized by radiologists are in fact the magnitude images resulting from the complex Fourier transform of the k-space data. The complex Fourier transform does not affect the Gaussian noise characteristics since this is a linear and orthogonal transform [184]. However, the calculation of the magnitude is a non-linear transform — i.e., the square root of the sum of squares of real and the imaginary parts — implying that the noise distribution is no longer Gaussian; it indeed follows a Rician distribution making the denoising task more challenging. Briefly, a Rician distribution is characterized as follows: in low-SI region (low-SNR), it can be approximated with a Rayleigh distribution while in high-SI region (high-SNR), it is similar to a Gaussian distribution [167]. Refer to Fig. 3.2 to observe the difference between a Gaussian and Rayleigh distribution. Comprehensive reviews regarding denoising methods can be found in [30, 177].

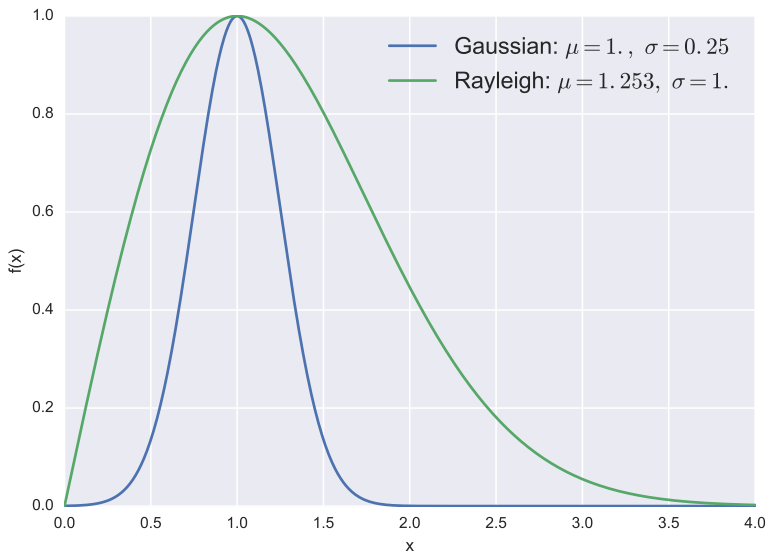


Figure 3.2: Illustration of a Gaussian and Rayleigh distribution. Although the mode of these distributions are identical, it can be noted that the Rayleigh distribution ($\mu = 1.253$) is suffering of a bias term when compared with the Gaussian distribution ($\mu = 1$).

Median filtering is the simplest approach used to address the denoising issue in MRI images [191, 192]. In both studies, Ozer et al. used a square-shaped kernel of size $5 \text{ px} \times 5 \text{ px}$.

More recently, Rampun et al. used a combination of median and anisotropic diffusion filter [215, 217, 218, 219], proposed in [149]. In low-SNR images, the gradient generated by an edge and noise can be similar, making the denoising by diffusion more challenging. In this condition, the threshold allowing to locally differentiate a noise gradient from an edge gradient needs to be increased, at the cost of blurring edges after filtering. Therefore, Ling and Bovik proposed to apply a standard anisotropic diffusion filter with a low threshold followed by a median filtering to remove large noise spikes.

Samarasinghe et al. filtered DCE-MRI images with a sliding 3D Gaussian filter [230]. However, from a theoretical point of view, this simple filtering method is not well formalized to address the noise distribution in MRI images. That is why more complex approaches have been proposed to overcome this problem. Another common method used to denoise MRI images is based on wavelet decom-

3. REVIEW OF CAD SYSTEMS FOR CAP

position and shrinkage. This filtering exploits the sparsity property of the wavelet decomposition. The projection of a noisy signal from the spatial-domain to the wavelet-domain implies that only few wavelet coefficients contribute to the “signal-free noise” while all wavelet coefficients contribute to the noise [61]. Therefore, insignificant wavelet coefficients are thresholded/attenuated to enforce the sparsity in the wavelet-domain, which result to a denoising process in the spatial domain. Investigations focus on the strategies to perform the most adequate coefficient shrinkage (e.g., thresholding, singularity property, or Bayesian framework) [204]. Ampeliotis et al. denoised the magnitude MRI images [9, 10] — i.e., T₂-W-MRI and DCE-MRI — by wavelet shrinkage, using thresholding techniques [165]. However, since the wavelet transform is an orthogonal transform, the Rician distribution of the noise is preserved in the wavelet-domain. Hence, for low-SNR, the wavelet and scaling coefficients still suffer from a bias due to this specific noise distribution [184]. That is why, Lopes et al. filtered T₂-W-MRI images [158], using the method proposed in [205] based on joint detection and estimation theory. In this approach, the wavelet coefficients “free-of-noise” are estimated from the noisy wavelet coefficients using a maximum *a posteriori* (MAP) estimate. Furthermore, the designed estimator takes spatial context into account by including both local and global information in the prior probabilities. The different probabilities needed by the MAP are empirically estimated by using mask images, representing the locations of the significant wavelet coefficients. These mask images are computed by thresholding the detail images obtained from the wavelet decomposition. To remove the bias from the wavelet and scaling coefficients, the squared magnitude MRI image is computed instead of the magnitude MRI image as proposed in [184]. This involves changing the Rician distribution to a scaled non-central Chi-squared distribution. It implies that the wavelet coefficients are also unbiased estimators and the scaling coefficients are unbiased estimators but up to a constant C as defined in Eq. (3.1) which needs to be subtracted from each scaling coefficient such as:

$$C = 2^{(J+1)}\hat{\sigma}^2, \quad (3.1)$$

where J is the number of levels of the wavelet decomposition and $\hat{\sigma}$ is an estimate of the noise standard deviation.

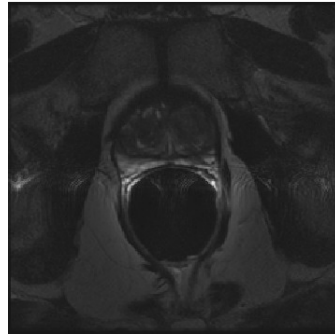


Figure 3.3: Example of artifacts with high SI due to perturbation from the endorectal coil which create non-homogeneity.

Bias correction Besides being corrupted by noise, MRI images are also affected by the inhomogeneity of the MRI field commonly referred to as bias field [255]. This bias field results in a smooth variation of the SI through the image. When an endorectal coil is used, a resulting artifact of an hyper-intense signal is observed around the coil as depicted in Fig. 3.3. As a consequence, the SI of identical tissues varies depending on their spatial location in the image making further processes such as segmentation, registration, or classification more challenging [115, 297]. A comprehensive review of bias correction methods is proposed in [297].

The model of image formation is usually formalized as:

$$s(\mathbf{x}) = o(\mathbf{x})b(\mathbf{x}) + \eta(\mathbf{x}) , \quad (3.2)$$

where $s(\mathbf{x})$ is the corrupted SI at the pixel for the image coordinates $\mathbf{x} = \{x, y\}$, $o(\mathbf{x})$ is the “noise-free signal” , $b(\mathbf{x})$ is the bias field function and $\eta(\mathbf{x})$ is an additive white Gaussian noise.

Hence, the task of bias correction involves estimating the bias function $b(\mathbf{x})$ in order to infer the “signal-free bias” $o(\mathbf{x})$.

Viswanath et al. corrected this artifact on T₂-W-MRI images [290], using the model proposed in [255], in which Styner et al. model the bias field function by using a linear combination of Legendre polynomials f_i as:

$$\begin{aligned}\hat{b}(\mathbf{x}, \mathbf{p}) &= \sum_{i=0}^{m-1} p_i f_i(\mathbf{x}) \\ &= \sum_{i=0}^l \sum_{j=0}^{l-i} p_{ij} P_i(x) P_j(y) ,\end{aligned}\tag{3.3}$$

where $\hat{b}(\cdot)$ is the bias estimation with the image coordinates $\mathbf{x} = \{x, y\}$ and the m coefficients of the linear combination $\mathbf{p} = p_{11}, \dots, p_{ij}$; m can be defined as $m = (l + 1) \frac{(l+2)}{2}$ where l is the degree of Legendre polynomials chosen and $P_i(\cdot)$ denotes a Legendre polynomial of degree i .

This family of functions offers to model the bias function as a smooth inhomogeneous function across the image. To estimate the set of parameters \mathbf{p} , a cost function is defined which relies on the following assumptions: (i) an image is composed of k regions with a mean μ_k and a variance σ_k^2 for each particular class, and (ii) each noisy pixel belongs to one of the k regions with its SI value close to the class mean μ_k . Hence, the cost function is defined as:

$$C(\mathbf{p}) = \sum_{\mathbf{x}} \prod_k \rho_k(s(\mathbf{x}) - \hat{b}(\mathbf{x}, \mathbf{p}) - \mu_k) ,\tag{3.4}$$

$$\rho_k(x) = \frac{x^2}{x^2 + 3\sigma_k^2} ,\tag{3.5}$$

where $\rho_k(\cdot)$ is a M-estimator allowing estimations to be less sensitive to outliers than the usual squared distance [144].

Finally, the parameters \mathbf{p} are estimated by finding the minimum of the cost function $C(\mathbf{p})$, which was optimized using the non-linear (1+1) Evolution Strategy (ES) optimizer [254].

In a later publication, Viswanath et al. as well as Giannini et al. corrected T_2 -W-MRI [81, 292] using the well known N3 algorithm [243] in which Sled et al. infer the bias function using the probability density functions (PDFs) of the signal and bias. Taking advantage of the logarithm property, the model in Eq. (3.2) becomes additive as expressed in Eq. (3.6).

$$\begin{aligned}\log s(\mathbf{x}) &= \log b(\mathbf{x}) + \log \left(o(\mathbf{x}) + \frac{\eta(\mathbf{x})}{b(\mathbf{x})} \right) , \\ &\approx \log b(\mathbf{x}) + \log \hat{o}(\mathbf{x}) ,\end{aligned}\tag{3.6}$$

where $\hat{o}(\mathbf{x})$ is the signal only degraded by noise. Sled et al. show that Eq. (3.6) is related to PDFs such that:

$$S(s) = B(s) * O(s) ,\tag{3.7}$$

where $S(\cdot)$, $B(\cdot)$, and $O(\cdot)$ are the PDFs of $s(\cdot)$, $b(\cdot)$, and $o(\cdot)$, respectively.

The corrupted signal s is restored by finding the multiplicative field b which maximizes the frequency content of the distribution O . Sled et al. argued that a brute-force search through all possible fields b and selecting the one which maximizes the high frequency content of O is possible but far to complex. By assimilating the bias field distribution to be a near Gaussian distribution as *a priori*, it is then possible to infer the distribution O using the Wiener deconvolution given B and S and later estimate the corresponding smooth field b .

Lv et al. corrected the non-homogeneity in T₂-W-MRI images [160] by using the method proposed in [163]. Madabhushi et al. proposed to correct the MRI images by detecting the image foreground via generalized scale (*g*-scale) in an iterative manner and estimating a bias field function based on a 2nd order polynomial model. First, the background of the MRI image is eliminated by thresholding, in which the threshold value is commonly equal to the mean SI of the considered image. Then, a seeded region growing algorithm is applied in the image foreground, considering every thresholded pixel as a potential seed. However, pixels already assigned to a region are not considered any more as potential seed. As in seeded region growing algorithm [238], two criteria are taken into account to expand a region. First, the region grows using a connected-neighbourhood, initially defined by the user. Then, the homogeneity of SI is based on a fuzzy membership function taking into account the absolute difference of two pixel SI. Depending on the membership value — corresponding to a threshold which needs to be defined — the pixel considered is merged or not to the region. Once this segmentation is performed, the largest

3. REVIEW OF CAD SYSTEMS FOR CAP

region R is used as a mask to select pixels of the original image and the mean SI, μ_R , is computed. The background variation $b(\mathbf{x})$ is estimated as:

$$b(\mathbf{x}) = \frac{s(\mathbf{x})}{\mu_R}, \quad \forall \mathbf{x} \in R, \quad (3.8)$$

where $s(\mathbf{x})$ is the original MRI image.

Finally, a 2nd order polynomial $\hat{b}_\Theta(\mathbf{x})$ is fitted in a least-squares sense as in Eq. (3.9),

$$\hat{\Theta} = \arg \min_{\Theta} |b(\mathbf{x}) - \hat{b}_\Theta(\mathbf{x})|^2, \quad \forall \mathbf{x} \in R. \quad (3.9)$$

Finally, the whole original MRI image is corrected by dividing it by the estimated bias field function $\hat{b}_\Theta(\mathbf{x})$. The convergence is reached when the number of pixels in the largest region R does not change significantly between two iterations.

SI normalization/standardization As discussed in the later section, segmentation or classification tasks are usually composed of a learning stage using a set of training patients. Hence, one can emphasize the desire to perform automatic diagnosis with a high repeatability or in other words, one would ensure to obtain consistent SI of tissues across patients of the same group — i.e., healthy patients *vs.* patients with CaP — for each MRI modality. However, it is a known fact that variability between patients occurs during the MRI examinations even using the same scanner, protocol or sequence parameters [185]. Hence, the aim of normalization or standardization of the MRI data is to remove the variability between patients and enforce the repeatability of the MRI examinations. These standardization methods are categorized either as statistical-based standardization or organ SI-based standardization

Artan et al., Ozer et al., and Rampun et al. standardized T₂-W-MRI, DCE-MRI, and DW-MRI images [14, 15, 191, 192, 215, 216, 217, 218, 219] by computing the *standard score* (also called *z-score*) of the pixels of the PZ as:

$$I_s(\mathbf{x}) = \frac{I_r(\mathbf{x}) - \mu_{pz}}{\sigma_{pz}}, \quad \forall \mathbf{x} \in \text{PZ}, \quad (3.10)$$

where $I_s(\mathbf{x})$ is the standardized SI with the image coordinates $\mathbf{x} = \{x, y\}$, $I_r(\mathbf{x})$ is the raw SI, μ_{pz} is the mean SI of the PZ and σ_{pz} is the SI standard deviation

3.1 Image regularization framework

in the PZ. This transformation enforces the image PDF to have a zero mean and a unit standard deviation. In a similar way, Liu et al. normalized T₂-W-MRI by making use of the median and inter-quartile range for all the pixels [155].

Lv et al. scaled the SI of T₂-W-MRI images using the method proposed in [186] based on PDF matching [160]. This approach is based on the assumption that MRI images from the same sequence should share the same PDF appearance. Hence, one can approach this issue by transforming and matching the PDFs using some statistical landmarks such as quantiles. Using a training set, these statistical landmarks — such as minimum, 25th percentile, median, 75th percentile, and maximum — are extracted for N training images:

$$\begin{aligned}\Phi_0 &= \{\phi_0^1, \phi_0^2, \dots, \phi_0^N\}, \\ \Phi_{25} &= \{\phi_{25}^1, \phi_{25}^2, \dots, \phi_{25}^N\}, \\ \Phi_{50} &= \{\phi_{50}^1, \phi_{50}^2, \dots, \phi_{50}^N\}, \\ \Phi_{75} &= \{\phi_{75}^1, \phi_{75}^2, \dots, \phi_{75}^N\}, \\ \Phi_{100} &= \{\phi_{100}^1, \phi_{100}^2, \dots, \phi_{100}^N\},\end{aligned}\tag{3.11}$$

where $\phi_{n^{\text{th}}}^{i^{\text{th}}}$ is the n^{th} percentile of the i^{th} training image.

Then, the mean of each statistical landmarks $\{\bar{\Phi}_0, \bar{\Phi}_{25}, \bar{\Phi}_{50}, \bar{\Phi}_{75}, \bar{\Phi}_{100}\}$ is also calculated. Once this training stage is performed, a piecewise linear transformation $\mathcal{T}(\cdot)$ is computed as in Eq. (3.12). For each test image t , this transformation maps each statistical landmark $\varphi_{(\cdot)}^t$ of the image t to the pre-learned statistical landmarks $\bar{\Phi}_{(\cdot)}$. An example of such piecewise linear function is depicted in Fig. 3.4.

$$\mathcal{T}(s(\mathbf{x})) = \begin{cases} \lceil \bar{\Phi}_0 + (s(\mathbf{x}) - \varphi_0^t) \left(\frac{\bar{\Phi}_{25} - \bar{\Phi}_0}{\varphi_{25}^t - \varphi_0^t} \right) \rceil, & \text{if } \varphi_0^t \leq s(\mathbf{x}) < \varphi_{25}^t, \\ \lceil \bar{\Phi}_{25} + (s(\mathbf{x}) - \varphi_{25}^t) \left(\frac{\bar{\Phi}_{50} - \bar{\Phi}_{25}}{\varphi_{50}^t - \varphi_{25}^t} \right) \rceil, & \text{if } \varphi_{25}^t \leq s(\mathbf{x}) < \varphi_{50}^t, \\ \lceil \bar{\Phi}_{50} + (s(\mathbf{x}) - \varphi_{50}^t) \left(\frac{\bar{\Phi}_{75} - \bar{\Phi}_{50}}{\varphi_{75}^t - \varphi_{50}^t} \right) \rceil, & \text{if } \varphi_{50}^t \leq s(\mathbf{x}) < \varphi_{75}^t, \\ \lceil \bar{\Phi}_{75} + (s(\mathbf{x}) - \varphi_{75}^t) \left(\frac{\bar{\Phi}_{100} - \bar{\Phi}_{75}}{\varphi_{100}^t - \varphi_{75}^t} \right) \rceil, & \text{if } \varphi_{75}^t \leq s(\mathbf{x}) \leq \varphi_{100}^t, \end{cases}\tag{3.12}$$

Viswanath et al. used a variant of the piecewise linear normalization presented in [162], to standardize T₂-W-MRI images [290, 291, 292]. Instead of computing the PDF of an entire image, a pre-segmentation of the foreground is carried out

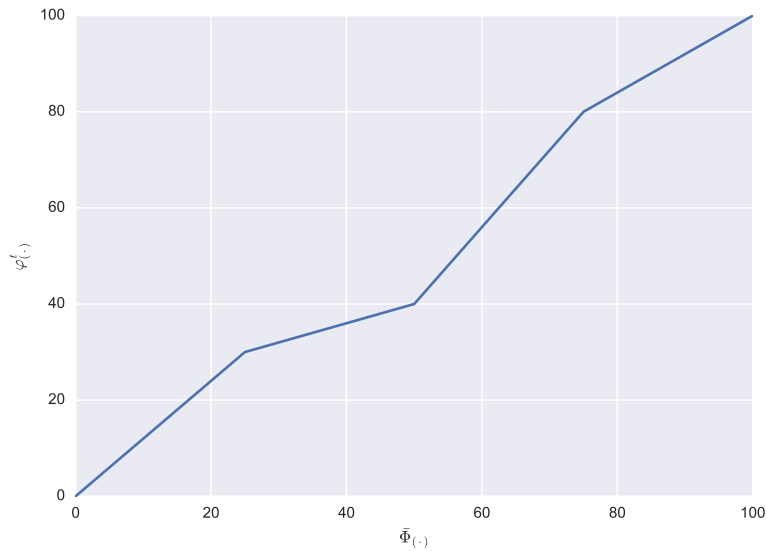


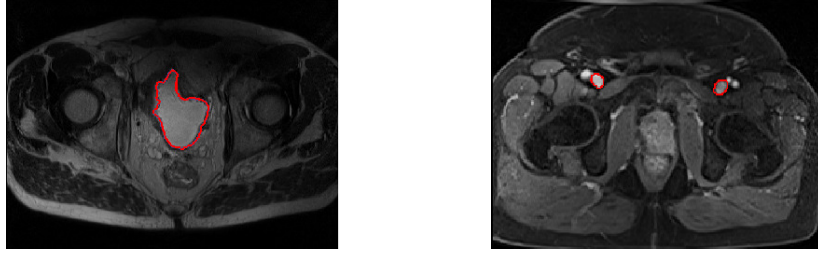
Figure 3.4: Example of piecewise linear normalization as proposed in [186].

via g -scale which has been discussed in the bias correction section. Once the foreground is detected, the largest region is extracted, and the regular piecewise linear normalization is applied.

The standardization problem can be tackled by normalizing the MRI images using the SI of some known organs present in these images. Niaf et al. and Lehaire et al. normalized T₂-W-MRI images by dividing the original SI of the images by the mean SI of the bladder [133, 181, 182], which is depicted in Fig. 3.5(a). Giannini et al. also normalized the same modality but using the signal intensity of obturator muscle [81]. Likewise, Niaf et al. standardized the T₁-W-MRI images using the arterial input function (AIF) [181]. They computed the AIF by taking the mean of the SI in the most enhanced part of the common femoral arteries — refer to Fig. 3.5(b) — as proposed in [301]. Along the same line, Samarasinghe et al. normalized the SI of lesion regions in T₁-W-MRI using the mean intensity of the prostate gland in the same modality [230].

3.1.1.2 MRSI modality

As presented in Sect. 2.6, MRSI is a modality related to a one dimensional signal. Hence, specific pre-processing steps for this type of signals have been applied



(a) Illustration and location of the bladder on a T₂-W-MRI image acquired with a 3 T MRI scanner

(b) Illustration and location of the femoral arteries on a T₁-W-MRI image acquired with a 3 T MRI scanner

Figure 3.5: Illustration of the two organs used in [181, 182] to normalize T₂-W-MRI and T₁-W-MRI images.

instead of standard signal processing methods.

Phase correction Acquired MRSI spectra suffer from zero-order and first-order phase misalignment [42, 188] as depicted in Fig. 3.6. Parfait et al. and Trigui et al. used a method proposed by Chen et al. where the phase of MRSI signal is corrected based on entropy minimization in the frequency domain [196, 273, 274]. The corrected MRSI signal $o(\xi)$ can be expressed as:

$$\begin{aligned}\Re(o(\xi)) &= \Re(s(\xi)) \cos(\Phi(\xi)) - \Im(\xi) \sin(\Phi(\xi)) , \\ \Im(o(\xi)) &= \Im(s(\xi)) \cos(\Phi(\xi)) + \Re(\xi) \sin(\Phi(\xi)) , \\ \Phi(\xi) &= \phi_0 + \phi_1 \frac{\xi}{N} ,\end{aligned}\quad (3.13)$$

where $\Re(\cdot)$ and $\Im(\cdot)$ are the real and imaginary part of the complex signal, respectively, $s(\xi)$ is the corrupted MRSI signal, ϕ_0 and ϕ_1 are the zero-order and first-order phase correction terms respectively and N is the total number of samples of the MRSI signal.

Chen et al. tackled this problem as an optimization in which ϕ_0 and ϕ_1 have to be inferred. Hence, the simplex Nelder-Mead optimizer [180] is used to minimize

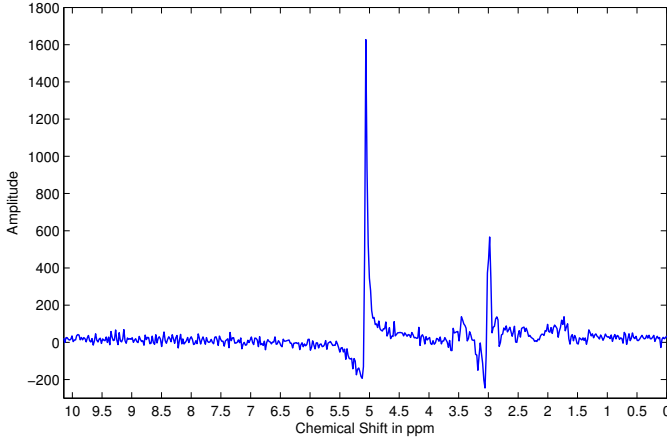


Figure 3.6: Illustration of phase misalignment in an MRSI spectra acquire with a 3 T MRSI scanner. Note the distortion of the signal specially visible for the water and citrate peaks.

the following cost function based on the *Shannon entropy* formulation:

$$\hat{\Phi} = \arg \min_{\Phi} \left[- \sum \Re(s'(\xi)) \ln \Re(s'(\xi)) + \lambda \|\Re(s(\xi))\|_2 \right], \quad (3.14)$$

where $s'(\xi)$ is the first derivative of the corrupted signal $s(\xi)$ and λ is a regularization parameter. Once the best parameter Φ vector is obtained, the MRSI signal is corrected using Eq. (3.13).

Water and lipid residuals filtering The water and lipid metabolites occur in much higher concentrations than the metabolites of interests, namely choline, creatine, and citrate [188, 305]. Fortunately, specific MRSI sequences have been developed in order to suppress water and lipid metabolites using pre-saturation techniques [305]. However, these techniques do not perfectly remove water and lipids peaks and some residuals are still present in the MRSI spectra as illustrated in Fig. 3.7. Therefore, different post-processing methods have been proposed to enhance the quality of the MRSI spectra by removing these residuals. For instance, Kelm et al. used the HSVD algorithm proposed by Pijnappel et al. which models the MRSI signal by a sum of exponentially damped sine waves in the time domain

3.1 Image regularization framework

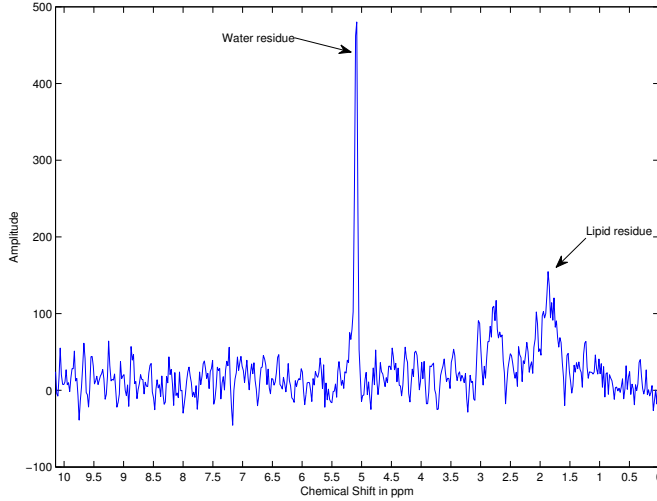


Figure 3.7: Illustration of the residues of water and fat even after their suppression during the acquisition protocol. The acquisition has been carried out with a 3 T MRI.

as Eq. (3.15).

$$s(t) = \sum_{k=1}^K a_k \exp(i\phi_k) \exp(-d_k + i2\pi f_k)t + \eta(t) , \quad (3.15)$$

where a_k is the amplitude proportional to the metabolite concentration with a resonance frequency f_k , d_k represents the damping factor of the exponential, ϕ_k is the first-order phase, and $\eta(t)$ is a complex white noise.

The “noise-free signal” can be found using the singular value decomposition (SVD) decomposition [203]. Therefore, the noisy signal is reorganized inside an Hankel matrix H . It can be shown that the signal is considered as a “noise-free signal” if the rank of H is equal to rank K . However, due to the presence of noise, H is in fact a full rank matrix. Thus, to recover the “noise-free signal”, the rank of H is truncated to K using its SVD decomposition. Hence, knowing the cut off frequencies of water — i.e., 4.65 ppm — and lipid — i.e., 2.2 ppm — metabolites, their corresponding peaks are reconstructed and subtracted from the original signal [130].

3. REVIEW OF CAD SYSTEMS FOR CAP

Baseline correction Sometimes, the problem discussed in the above section regarding the lipid molecules is not addressed simultaneously with water residuals suppression. Lipids and macro-molecules are known to affect the baseline of the MRSI spectra, causing errors while quantifying metabolites, especially the citrate metabolite.

Parfait et al. made the comparison of two different methods to detect the baseline and correct the MRSI spectra [196] which are based on [60, 145]. Lieber and Mahadevan-Jansen corrected the baseline in the frequency domain by fitting a low degree polynomial $p(x)$ — e.g., 2nd or 3rd degree — to the MRSI signal $s(x)$ in a least-squares sense [145]. Then, the values of the fitted polynomial are re-assigned as:

$$p_f(x) = \begin{cases} p(x) , & \text{if } p(x) \leq s(x) , \\ s(x) , & \text{if } p(x) > s(x) . \end{cases} \quad (3.16)$$

Finally, this procedure of fitting and re-assignment is repeated on $p_f(x)$ until a stopping criterion is reached. The final polynomial function is subtracted from the original signal $s(x)$ to correct it. [196] modified this algorithm by convolving a Gaussian kernel to smooth the MRSI signal instead of fitting a polynomial function, keeping the rest of the algorithm identical. Unlike Lieber and Mahadevan-Jansen, Devos et al. corrected the baseline in the time domain by multiplying the MRSI signal by a decreasing exponential function [60] as:

$$c(t) = \exp(-\beta t) , \quad (3.17)$$

with a typical β value of 0.15. However, Parfait et al. concluded that the method proposed in [145] outperformed the one in [60]. The later study of Trigui et al. used these conclusion and adopted the same method [273, 274].

In the contemporary work of Tiwari et al., the authors detected the baseline using a local non-linear fitting method avoiding regions with significant peaks which have been detected using an experimentally parametric signal-to-noise ratio, which has been set to a value larger than 5 dB.

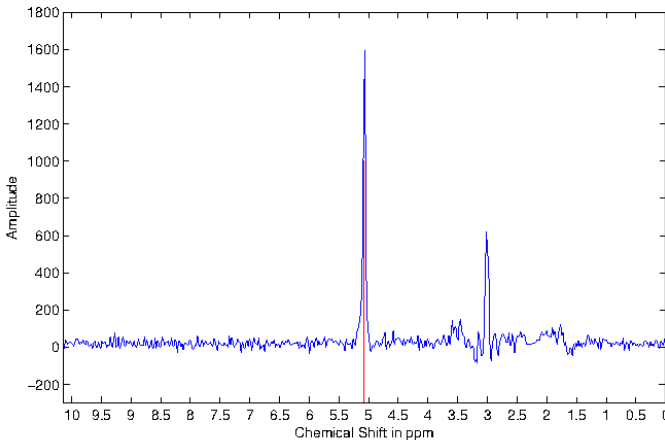


Figure 3.8: Illustration of frequency misalignment in a MRSI spectra acquired with a 3 T MRSI scanner. The water peak is known to be aligned at 4.65 ppm. However, it can be seen that the peak on this spectra is aligned at around 5.1 ppm.

Frequency alignment Due to variations of the experimental conditions, a frequency shift is commonly observed in the MRSI spectra [42, 188] as depicted in Fig. 3.8. Tiwari et al. corrected this frequency shift by first detecting known metabolite peaks such as choline, creatine, or citrate and minimizing the frequency error between the experimental and theoretical values for each of these peaks [266].

Normalization The NMR spectra is subject to variations due to intra-patient variations and non homogeneity of the magnetic field. Parfait et al. as in [60] compared two methods to normalize MRSI signal [196]. In each method, the original MRSI spectra is divided by a normalization factor, similar to the intensity normalization described earlier. The first approach consists in estimating the water concentration from an additional MRSI sequence where the water has not been suppressed. The estimation is performed using the previously HSVD algorithm. The second approach does not require any additional acquisition and is based on the L_2 norm of the MRSI spectra $\|s(\xi)\|_2$. It should be noted that both Parfait et al. and Devos et al. concluded that the L_2 normalization is the most efficient method [196]. Lately, Trigui et al. used the L_2 normalization in their framework [273, 274].

3. REVIEW OF CAD SYSTEMS FOR CAP

Table 3.2: Overview of the pre-processing methods used in CAD systems.

Pre-processing operations	References
MRI pre-processing:	
Noise filtering:	
• Anisotropic median-diffusion filtering	[215, 216, 217, 218, 219]
• Gaussian filtering	[230]
• Median filtering	[191, 192]
• Wavelet-based filtering	[9, 10, 158]
Bias correction:	
• Parametric methods	[81, 160, 290]
• Non-parametric methods	[291]
Standardization:	
• Statistical-based normalization:	[14, 15, 160, 191, 192, 215, 216, 217, 218, 219, 290, 291, 292]
• Organ SI-based normalization	[133, 181, 182, 230]
MRSI pre-processing:	
Phase correction	[196, 273, 274]
Water and lipid residuals filtering	[119]
Baseline correction	[196, 266, 273, 274]
Frequency alignment	[266, 273, 274]
Normalization	[196, 273, 274]

3.1.1.3 Summary

The different pre-processing methods are summarized in Table 3.2.

3.1.2 Segmentation

The segmentation task consists in delineating the prostate boundaries in the MRI and is of particular importance for focusing the posterior processing on the organ of interest [79]. In this section, only the segmentation methods used in CAD for CaP are presented. An exhaustive review of prostate segmentation methods in MRI is available in [79].

Manual segmentation To highlight the importance of prostate segmentation task in CAD systems, it is interesting to note the large number of studies which manually segment the prostate organs [14, 15, 133, 168, 181, 182, 191, 192, 209, 273, 274, 293, 294]. In all the cases, the boundaries of the prostate gland are manually defined in order to limit further processing to only this area. This approach

3.1 Image regularization framework

ensures the right delineation of the organ; nevertheless this procedure is highly time consuming and should be performed by a radiologist.

Region-based segmentation Litjens et al. used a multi-atlas-based segmentation using multi-modal images — i.e., T₂-W-MRI and ADC map — to segment the prostate with an additional pattern recognition method to differentiate CG and PZ [154], as proposed in [150]. This method consists in three different steps: (i) the registration between each atlas and the multi-modal images, (ii) the atlas selection, and finally (iii) the classification of the prostate voxels into either CG or PZ classes. Each atlas and the MRI images are registered through two successive registrations: a rigid registration to roughly align the atlases and the MRI images followed by an elastic registration using a B-spline transformation. The cost function driving the registration is defined as the weighted sum of the mutual information (MI) of both T₂-W-MRI and ADC map. The final atlas is selected using either a majority voting or the simultaneous truth and performance level estimation (STAPLE) approach [300]. Subsequently, each voxel within the prostate are classified either as CG or PZ using a linear discriminant analysis (LDA) classifier. Three types of feature are considered to characterize the voxels: (i) anatomy, (ii) intensity, and (iii) texture. The relative position and the relative distance from the voxel to the border of the prostate encode the anatomical information. The intensity features consist in the intensity of the voxel in the ADC coefficient and the T₂ map. The texture features are composed of 5 different features: homogeneity, correlation [6], entropy, texture strength [142], and local binary pattern (LBP) [187]. Finally, the final segmentation is obtained by removing artifacts and smoothing the contour between the zones using the thin plate spline (TPS) [23].

Litjens et al. used an almost identical algorithm in [151], initially proposed for the PROMISE12 challenge [152]. Their segmentation method is also based on multi-atlas multi-modal images, but the SIMPLE method [128] is used instead, to combine labels after the registration of the different atlas to obtain the final segmentation.

Finally, Rampun et al. recurrently used a method to segment the PZ [215, 216, 217, 218, 219], which is proposed in [214]. The PZ is modelled using a quadratic

3. REVIEW OF CAD SYSTEMS FOR CAP

function driven by the centre of the prostate, the left-most, and the right-most coordinates of the prostate boundaries.

Model-based segmentation Viswanath et al. in [288, 290] used the multi-attribute non-initializing texture reconstruction based active shape model (MANTRA) method as proposed by Toth et al. [271]. MANTRA [271] is closely related to the active shape model (ASM) from [50]. This algorithm consists of two stages: (i) a training stage where a shape and an appearance model are generated and (ii) the actual segmentation based on the learned model. For the training stage, a set of landmarks is defined and the shape model is generated as in the original ASM method [50]. Then, to model the appearance, a set of K texture images $\{I_1, I_2, \dots, I_k\}$ based on first and second order statistical texture features is computed. For a given landmark l with its given neighbourhood $\mathcal{N}(l)$, its feature matrix extracted is expressed as:

$$f_l = \{I_1(\mathcal{N}(l)), I_2(\mathcal{N}(l)), \dots, I_k(\mathcal{N}(l))\} , \quad (3.18)$$

where $I_k(\mathcal{N}(l))$ represents a feature vector obtained by sampling the k^{th} texture map using the neighbourhood $\mathcal{N}(l)$. Therefore, multiple landmarks are generated followed by a decomposition using principal components analysis (PCA) [199] to learn the appearance variations as in ASM.

For the segmentation stage, the mean shape learned previously is initialized in the test image. The same associated texture images as in the training stage are computed. For each landmark l , a neighbourhood of patches are used to sample the texture images and a reconstruction is obtained using the appearance model previously trained. The new landmark location will be defined as the position where the MI is maximal between the reconstructed and original values. This scheme is performed in a multi-resolution manner as in [50].

Subsequently, Viswanath et al. in [292], used the weighted ensemble of regional image textures for active shape model segmentation (WERITAS) method also proposed in Toth et al.. Similarly to MANTRA, WERITAS is also based on the ASM formulation [272]. It differs in the last stage of the algorithm in which the Mahalanobis distance is used instead of the MI metric, to adapt the positions

3.1 Image regularization framework

of new landmarks. In the training stage, the Mahalanobis distance is computed between landmarks and neighbour patches for each of the features. Subsequently, a new metric is proposed as a linear weighted combination of those Mahalanobis distances which maximizes the correlation with the Euclidean distance between the patches and the true landmarks. In the segmentation step, this metric is then computed between the initialized landmarks and neighbouring patches in order to update landmark positions, in a similar fashion to other active contour model (ACM) models.

Litjens et al. as well as Vos et al. used an approach proposed in [108] in which the bladder, the prostate, and the rectum are segmented [153, 296]. The segmentation task is performed as an optimization problem taking 3 parameters into account linked to organ characteristics such as: (i) the shape (i.e., an ellipse), (ii) the location, and (iii) the respective angles between them. Furthermore, Litjens et al. used only the ADC map to encode the appearance [153] whereas Vos et al. used both ADC and T₂ maps [296]. The cost function, defined as the sum of the deviations, is minimized using a quasi-Newton optimizer. This rough segmentation is then used inside a Bayesian framework to refine the segmentation.

Giannini et al. segmented the prostate with a multi-Otsu thresholding [190] in ADC images [81]. Further morphological operations are applied to improve the segmentation.

Only the work of Tiwari et al. used the MRSI modality to segment the prostate organ [263]. The prostate is segmented based on an unsupervised hierarchical spectral clustering. First, each MRSI spectrum is projected into a lower-dimensional space using graph embedding [239]. To proceed, a similarity matrix W is computed using a Gaussian similarity measure from Euclidean distance [18] such that:

$$W(\mathbf{x}, \mathbf{y}) = \begin{cases} \exp\left(\frac{\|s(\mathbf{x}) - s(\mathbf{y})\|_2^2}{\sigma^2}\right) & \text{if } \|\mathbf{x} - \mathbf{y}\|_2 < \epsilon, \\ 0 & \text{if } \|\mathbf{x} - \mathbf{y}\|_2 > \epsilon. \end{cases} \quad (3.19)$$

where $s(\mathbf{x})$ and $s(\mathbf{y})$ are the MRSI spectra for the voxels \mathbf{x} and \mathbf{y} , respectively, σ is the standard deviation of the Gaussian similarity measure, and ϵ is the parameter to define an ϵ -neighbourhood.

3. REVIEW OF CAD SYSTEMS FOR CAP

Table 3.3: Overview of the segmentation methods used in CAD systems.

Segmentation methods	References
MRI-based segmentation:	
Manual segmentation	[14, 15, 133, 168, 181, 182, 191, 192, 209, 273, 274, 293, 294, 295, 296]
Region-based segmentation	[151, 154, 215, 216, 217, 218, 219]
Model-based segmentation	[81, 153, 288, 290, 291, 296]
MRSI-based segmentation:	
Clustering	[263]

The projection can be performed as a generalized eigenvector problem such that:

$$\begin{aligned}
 Lu &= \lambda Du, \\
 D(\mathbf{x}, \mathbf{x}) &= \sum_{\mathbf{y}} W(\mathbf{x}, \mathbf{y}), \\
 L &= D - W,
 \end{aligned} \tag{3.20}$$

where D is the diagonal weight matrix, L is the Laplacian matrix, λ and u represent the eigenvalues and eigenvectors. Once the MRSI spectra are projected into the lower-dimensional space, a replicate k-means clustering method is used to define 2 clusters. Subsequently, the data corresponding to the largest cluster is assumed to belong to the non-prostate voxels and thus these voxels are eliminated from the processing. The full procedure is repeated until the total number of voxels left is inferior to a given threshold experimentally set.

3.1.2.1 Summary

The segmentation used in CAD system for the detection of CaP are summarized in Table 3.3.

3.1.3 Registration

Image registration plays a vital role in CAD systems using mp-MRI images. As it will be discussed in Sect. 3.2, the features detected in each modality are grouped depending of their spatial location, requiring a perfect alignment of the mp-MRI ahead of the classification.

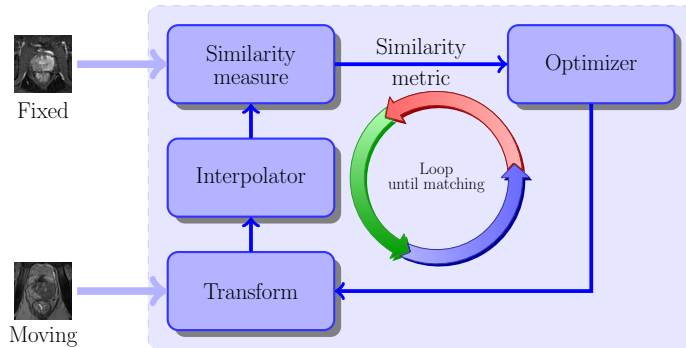


Figure 3.9: Typical framework involved to solve the registration problem.

Image registration is the procedure consisting of aligning an unregistered image — also called moving image — into a template image — also called fixed image — via a geometric transformation. This problem is usually addressed as depicted in Fig. 3.9. An iterative procedure takes place to infer the geometric transformation, parametric or non-parametric, via an optimizer which maximizes the similarity between the two images. In the following, a review of the different components of a typical registration framework: transformation model, similarity metric, optimizer, and interpolation are presented. To conclude a summary is given focusing on the registration approaches applied in CAD for CaP systems. Exhaustive reviews covering all registration methods in computer science and medical fields can be found in [164, 307].

Geometric transformation models As previously mentioned, the registration process is equivalent to find a geometric transformation which minimizes the difference between two images. From all CAD systems reviewed, only parametric methods have been implemented. Three different groups of parametric transformation models have been used — i.e., rigid, affine, and elastic — each of them characterized by a specific degree of freedom.

The simplest transformation used in terms of degree of freedom is usually referred to as rigid transformation. This type of transformation is only composed of a rotation and a translation. Therefore, for the 2D case where $\mathbf{x} = (x, y) \in \mathbb{R}^2$, a rigid transformation \mathcal{T}_R is formalized as:

3. REVIEW OF CAD SYSTEMS FOR CAP

$$\begin{aligned}\mathcal{T}_R(\mathbf{x}) &= \begin{bmatrix} R & \mathbf{t} \\ \mathbf{0}^T & 1 \end{bmatrix} \mathbf{x}, \\ &= \begin{bmatrix} \cos \theta & -\sin \theta & t_x \\ \sin \theta & \cos \theta & t_y \\ 0 & 0 & 1 \end{bmatrix} \begin{bmatrix} x \\ y \\ 1 \end{bmatrix},\end{aligned}\quad (3.21)$$

where θ is the rotation angle and $\{t_x, t_y\}$ represents the translation along $\{x, y\}$ respectively. In the case of 3D registration using volume, an additional component z is introduced such that $\mathbf{x} = (x, y, z)$. Thus, the rotation matrix \mathbf{R} becomes of size 3×3 whereas the translation vector \mathbf{t} consists of a vector of 3 variables. The geometric transformation $\mathcal{T}_R(\cdot)$ is embedded into a matrix of size 4×4 .

The affine transformation provide additional degrees of freedom, providing rotation, translation, — as with the rigid transformations — and also shearing and scaling. Hence, for a 2D space where $\mathbf{x} = (x, y) \in \mathbb{R}^2$, an affine transformation \mathcal{T}_A is formalized as:

$$\begin{aligned}\mathcal{T}_A(\mathbf{x}) &= \begin{bmatrix} A & \mathbf{t} \\ \mathbf{0}^T & 1 \end{bmatrix} \mathbf{x}, \\ &= \begin{bmatrix} a_{11} & a_{12} & t_x \\ a_{21} & a_{22} & t_y \\ 0 & 0 & 1 \end{bmatrix} \begin{bmatrix} x \\ y \\ 1 \end{bmatrix}.\end{aligned}\quad (3.22)$$

where the 4 parameters $\{a_{11}, a_{12}, a_{21}, a_{22}\}$ of the affine matrix and $\{t_x, t_y\}$ of the translation encode the deformation. As in the rigid registration case, in 3D the affine transformation $\mathcal{T}_A(\cdot)$ is of size 4×4 with 12 parameters involved.

Finally, the last group of transformation is known as elastic transformation and offers the advantage to handle local distortions. In the reviewed CAD systems, the radial basis functions are used to formalize the local distortions such as:

$$\mathcal{T}_E(\mathbf{x}) = \frac{a_{11}x - a_{12}y + t_x + \sum_i c_i g(\|\mathbf{x} - p_i\|)}{a_{21}x + a_{22}y + t_y + \sum_i c_i g(\|\mathbf{x} - p_i\|)}, \quad (3.23)$$

where \mathbf{x} are the control points in both images and $g(\dots)$ is the actual radial basis function.

Two radial basis functions are used: (i) the TPS and (ii) the B-splines. Apart from the formalism, these two approaches have a main difference: with B-splines,



(a) Illustration of a joint histogram between two aligned images.

(b) Illustration of a joint histogram between two misaligned images.

Figure 3.10: Difference observed in joint histogram between aligned and misaligned images. The joint measure will be more concentrated of the histogram in the case that the images are aligned and more randomly distributed in the case that both images are more misaligned.

the control points are usually uniformly and densely placed on a grid whereas with TPS, the control points correspond to some detected or selected key points. By using TPS, Mitra et al. obtained more accurate and time efficient results than with the B-splines strategy [176].

It is reasonable to point out that usually only rigid or affine registrations are used to register mp-MRI from a same protocol. Elastic registration methods are more commonly used to register multi-protocol images such as histopathology with MRI images [271, 272].

Similarity measure The most naive similarity measure used in reviewed registration framework is the mean squared error (MSE) of the SI of MRI images. For a pair of images I and J , the MSE is formalized as:

$$\text{MSE} = \frac{1}{N} \sum_x \sum_y [I(x, y) - J(x, y)]^2 , \quad (3.24)$$

where N is the total number of pixels. This metric is not well suited when mp-MRI images are involved due to the tissue appearance variations between the different modalities.

3. REVIEW OF CAD SYSTEMS FOR CAP

In this regard, MI has been introduced as a similarity measure in registration framework in the late 1990's by Pluim et al.. The MI measure finds its foundation in the assumption that a homogeneous region in the first modality image should also appear as a homogeneous region in the second modality, even if their SIs are not identical. Thus, those regions share information and the registration task is achieved by maximizing this common information. Hence, MI of two images A and B is defined as:

$$MI(A; B) = S(A) + S(B) - S(A, B) , \quad (3.25)$$

where $S(A)$, $S(B)$, and $S(A, B)$ are the marginal entropies of A and B and the joint entropy, respectively. Therefore, maximizing the MI is the equivalent of minimizing the joint entropy. The joint entropy measure is related to the degree of uncertainty or dispersion of the data in the joint histogram of the images A and B . As shown in Fig. 3.10, the data in the joint histogram are concentrated in the case of aligned images (see Fig. 3.10(a)) while it is more randomly distributed in the case of misaligned images (see Fig. 3.10(b)). The entropy is computed based on an estimation of the PDF of the images and thus histogram or Parzen window methods are a common way to estimate these PDFs.

A generalized form of MI, combined mutual information (CMI), has been proposed by Chappelow et al.. CMI encompasses interdependent information such as texture and gradient information into the metric. Hence, for both of images A and B , the image ensembles ϵ_n^A and ϵ_m^B are generated and composed of n and m images based on the texture and gradient. Then, the CMI is formulated such as:

$$CMI(\epsilon_n^A; \epsilon_m^B) = S(\epsilon_n^A) + S(\epsilon_m^B) - S(\epsilon_n^A, \epsilon_m^B) . \quad (3.26)$$

From Eq. (3.26), note that CMI is estimated from high-dimensional data and as a consequence the histogram-based methods to estimate the PDFs are not suitable anymore [40]. However, other alternative approaches are used such as the one employed in [251] to compute the α -MI [100].

3.1 Image regularization framework

Table 3.4: Classification of the different registration methods used in the CAD systems reviewed. Acronyms: mean squared error (MSE), mutual information (MI), combined mutual information (CMI), gradient descent (GD), limited-memory Broyden-Fletcher-Goldfarb-Shannon box constraints (L-BFGS-B).

Study index	Modality registered	Type	Geometric model		Similarity measure			Optimizer	
			Affine	Elastic	MSE	MI	CMI	GD	L-BFGS-B
[9, 10]	T ₂ -W - DCE	2D	✓	—	✓	—	—	—	—
[80, 81]	T ₂ -W - DW	2D	✓	✓	—	—	—	—	—
[80, 81]	T ₂ -W - DCE	2D	✓	✓	—	✓	—	✓	—
[288, 290]	T ₂ -W - DCE	2D	✓	—	—	✓	—	—	—
[291]	T ₂ -W - DCE - DW	3D	✓	—	—	—	✓	✓	—
[293]	T ₂ -W - DCE	3D	✓	—	—	✓	—	—	—
[295]	T ₂ -W - DCE	3D	✓	✓	—	✓	—	—	✓

Notes:

—: not used or not mentioned.

✓: used or implemented.

Optimization methods Registration is usually regarded as an optimization problem where the parameters of the geometric transformation model have to be inferred by minimizing/maximizing the similarity measure. Iterative optimization methods are commonly used, where the most common methods used are the L-BFGS-B quasi-Newton method [32] and the gradient descent [287]. During our review, we noticed that authors do not usually linger over optimizer choice.

Interpolation The registration procedure involves transforming an image and pixels mapped to non-integer points must be approximated using interpolation methods. As for the optimization methods, we notice that little attention has been paid on the choice of those interpolations methods. However, commonly used methods are bi-linear, nearest-neighbour, bi-cubic, spline, and inverse-distance weighting method [174].

Registration methods used in CAD systems Table 3.4 summarized the framework used to register mp-MRI images in CAD for CaP.

Ampeliotis et al. in [9, 10] did not use the framework as presented in Fig. 3.9 to register 2D T₂-W-MRI and DCE-MRI images. By using image symmetries

3. REVIEW OF CAD SYSTEMS FOR CAP

and the MSE metric, they found the parameters of an affine transformation but without using a common objective function. The scale factor, the rotation, and the translation are independently and sequentially estimated.

[80] used also a in-house registration method for 2D T₂-W-MRI and DW-MRI images using an affine model [80, 81]. The bladder is first segmented in both modalities in order to obtain its contours and to focus on the registration and minimize the distance between the contours.

Giannini et al. and also Vos et al. used a framework based on finding an affine transformation to register the T₂-W-MRI and DCE-MRI images using MI [80, 227, 295]. Then, an elastic registration using B-spline takes place using the affine parameters to initialize the geometric model with the same similarity measure. However, the two approaches differ regarding the choice of the optimizer since a gradient descent is used in [80] and a quasi-Newton method in [295]. Moreover, Giannini et al. applied a 2D registration whereas Vos et al. registered 3D volumes.

Viswanath et al. as well as Vos et al. registered T₂-W-MRI and DCE-MRI images using an affine registration and a MI metric [288, 290, 293]. However, the choice of the optimizer has not been specified. Furthermore, Viswanath et al. focused on 2D registration [288, 290] while Vos et al. performed 3D registration [293].

Finally, Viswanath et al. performed a 3D registration with the three modalities, T₂-W-MRI, DCE-MRI, and DW-MRI, using an affine transformation model combined with the CMI similarity measure [291]. Moreover, in this latter work, the authors employed a gradient descent approach [40] to solve this problem but suggested that the Nelder-Mead simplex and the quasi-Newton methods are other possible solutions.

3.2 Image classification framework

3.2.1 CADe: ROIs detection/selection

As discussed in the introduction and shown in Fig. 3.1, the image classification framework is often composed of a CADe and a CADx. In this section, we focus on studies which embed a CADe in their framework. Two approaches are considered to define a CADe: (i) voxel-based delineation and (ii) lesion segmentation. These

3.2 Image classification framework

Table 3.5: Overview of the CADe strategies employed in CAD systems.

CADe: ROIs selection strategy	References
All voxels-based approach	[14, 15, 80, 119, 121, 133, 157, 158, 168, 169, 191, 192, 196, 215, 216, 217, 218, 219, 256, 261, 262, 263, 264, 265, 266, 267, 273, 274, 288, 289, 290, 291, 292]
Lesions candidate detection	[33, 34, 151, 153, 154, 296]

methods are summarized in Table 3.5. The first strategy is in fact linked to the nature of the classification framework and concerns the majority of the studies reviewed [14, 15, 80, 119, 121, 133, 157, 158, 168, 169, 191, 192, 196, 215, 216, 217, 218, 219, 256, 261, 262, 263, 264, 265, 266, 267, 273, 274, 288, 289, 290, 291, 292]. Each voxel is a possible candidate and will be classified as cancer or healthy. The second group of methods is composed of method implementing a lesion segmentation algorithm to delineate potential candidates to further obtain a diagnosis through the CADx. This approach is borrowed from other application areas such as breast cancer. These methods are in fact very similar to the classification framework used in CADx later.

Vos et al. highlighted lesion candidates by detecting blobs in the ADC map [296]. These candidates are filtered using some *a priori* criteria such as SI or diameter. As mentioned in Sect. 2.6 and Table 2.1, low SI in ADC map can be linked to potential CaP. Hence, blob detectors are suitable to highlight these regions. Blobs are detected in a multi-resolution scheme, by computing the three main eigenvalues $\{\lambda_{\sigma,1}, \lambda_{\sigma,2}, \lambda_{\sigma,3}\}$ of the Hessian matrix, for each voxel location of the ADC map at a specific scale σ [143]. The probability p of a voxel \mathbf{x} being a part of a blob at the scale σ is given by:

$$P(\mathbf{x}, \sigma) = \begin{cases} \frac{\|\lambda_{\sigma,3}(\mathbf{x})\|^2}{\|\lambda_{\sigma,1}(\mathbf{x})\|} , & \text{if } \lambda_{\sigma,k}(\mathbf{x}) > 0 \text{ with } k = \{1, 2, 3\} , \\ 0 , & \text{otherwise .} \end{cases} \quad (3.27)$$

The fusion of the different scales is computed as:

$$L(\mathbf{x}) = \max P(\mathbf{x}, \sigma), \forall \sigma . \quad (3.28)$$

The candidate blobs detected are then filtered depending on their appearances — i.e., maximum of the likelihood of the region, diameter of the lesion — and their

3. REVIEW OF CAD SYSTEMS FOR CAP

SI in ADC and T₂-W-MRI images. The detected regions are then used as inputs for the CADx. Cameron et al. used a similar approach by automatically selecting low SI connected regions in the ADC map with a size larger than 1 mm² [33, 34].

Litjens et al. used a pattern recognition approach in order to delineate the ROIs [153]. A blobness map is computed in the same manner as in [295] using the multi-resolution Hessian blob detector on the ADC map, T₂-W, and pharmacokinetic parameters maps (see Sect. 3.2.2 for details about those parameters). Additionally, the position of the voxel $\mathbf{x} = \{x, y, z\}$ is used as a feature as well as the Euclidean distance of the voxel to the prostate center. Hence, each feature vector is composed of 8 features and a support vector machines (SVM) classifier is trained using a radial basis function (RBF) kernel (see Sect. 3.2.4 for more details).

Subsequently, Litjens et al. modified this approach by including only features related to the blob detection on the different maps as well as the original SIs of the parametric images [154]. Two new maps are introduced based on texture and a k -nearest neighbour (k -NN) classifier is used instead of a SVM classifier. The candidate regions are then extracted by performing a local maxima detection followed by post-processing region-growing and morphological operations.

3.2.2 CADx: Feature detection

Discriminative features which help to recognize CaP from healthy tissue need to be first detected. This processing is known in computer vision as feature extraction. However, feature extraction also refer to the name given in pattern recognition to some types of dimension reduction methods which are later presented. In order to avoid confusion between these two aspects, in this survey, the procedure “detecting” or “extracting” features from images and signals is defined as feature detection. This section summarizes the different features used in CAD for CaP and are summarized in Table 3.6.

Table 3.6: Overview of the feature detection methods used in CAD systems. Notes: (✓- ✓- ✓-): triplet stating the implementation or not of the feature for respectively T₂-W-MRI images, DCE-MRI images, DW-MRI images; ✓: used or implemented; ✓[!]: partially implemented.

Feature detection methods	Indexes
MRI image:	
<i>Voxel-wise detection</i>	
Intensity-based	✓- ✓- ✓- [9, 10, 215, 217, 293] ✓- ✓- ✓- [80] ✓- ✓- ✓- [14, 15, 33, 34, 39, 45, 81, 121, 127, 151, 153, 154, 157, 191, 192, 273, 274] ✓✓✓ [133, 181, 182]
Edge-based	✓- ✓- [264, 265, 267, 289] • Prewitt operator • Sobel operator • Kirsch operator • Gabor filtering ✓- ✓- [216, 218, 219, 264, 265, 267, 289, 290, 291, 292] ✓✓✓ [133, 181, 182] ✓- ✓- [264, 265, 267, 289, 290, 291, 292] ✓- ✓- [45, 121] ✓✓✓ [133, 181, 182] ✓- ✓- [266, 289, 292] ✓- ✓- [45, 121]
Texture-based	✓- ✓- [13, 216, 218, 219, 264, 265, 267, 273, 289, 290, 292] ✓- ✓- [291] ✓- ✓- [33, 34, 45, 121] ✓✓✓ [133, 154, 181, 182] • Haralick features • Tamura features • Fractal analysis • DCT • Wavelet-based features • Gaussian filter bank • Laplacian of Gaussian filter bank ✓- ✓- [216, 218, 219] ✓- ✓- [158, 160] ✓✓✓ [39] ✓- ✓- [292] ✓- ✓- [151, 216, 218, 219] ✓- ✓- [216, 218, 219]
Position-based	[39, 151, 153, 154]
<i>Region-wise detection</i>	
Statistical-based	✓- ✓- [294] ✓- ✓- [13, 201] ✓✓- [295] ✓✓✓ [133, 151, 153, 154, 181, 182, 296] • Percentiles • Statistical-moments ✓- ✓- [9, 10, 216, 218, 219, 264, 265, 267, 289, 290, 292] ✓- ✓- [13] ✓- ✓- [291] ✓- ✓- [33, 34, 45, 121, 201] ✓✓✓ [133, 151, 153, 154, 181, 182]
Histogram-based	✓✓✓ [155] • PDF

3. REVIEW OF CAD SYSTEMS FOR CAP

• HOG	✓✓✓ [155]
• Shape context	✓✓✓ [155]
• LBP	✓✓✓ [155]
Anatomical-based	[33, 34, 151, 154, 168]
Fractal-based	[158, 160]
DCE signal:	
Whole spectra approach	[9, 10]
Semi-quantitative approach	✓! [209] [81, 133, 169, 181, 182, 230, 256, 273, 274]
Quantitative approach	
• Toft model	✓! [155, 201] [80, 81, 127, 133, 151, 153, 154, 169, 181, 182]
• Brix model	✓! [14, 15, 191, 192] [157, 256]
• Weibull function	[80, 81, 169]
• PUN	[80, 81, 169]
MRSI signal:	
Whole spectra approach	[119, 168, 196, 261, 262, 263, 264, 265, 267, 289]
Quantification approach	[119, 196, 273, 274]
Wavelet-based approach	[266]

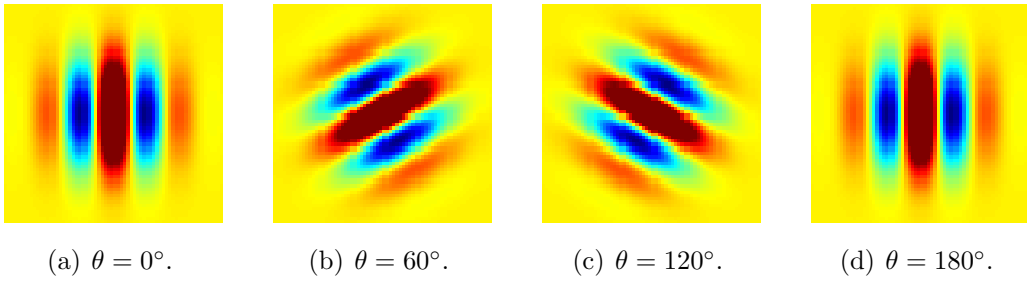


Figure 3.11: Illustration of 4 different Gabor filters varying their orientations θ .

3.2.2.1 Image-based features

This section focuses on image-based features which can be categorized into two categories: (i) voxel-wise detection and (ii) region-wise detection.

Voxel-wise detection This strategy refers to the fact that a feature is extracted at each voxel location. As discussed in Chap. 2, CaP has an influence on the SI in mp-MRI images. Therefore, intensity-based feature is the most commonly used feature [9, 10, 14, 15, 33, 34, 39, 45, 80, 81, 121, 127, 133, 151, 153, 154, 157, 181, 182, 191, 192, 215, 217, 273, 274, 293]. This feature consists in the extraction of the intensity of the MRI modality of interest.

Edge-based features have also been used to detect SI changes but bring additional information regarding the SI transition. Each feature is computed by convolving the original image with an edge operator. Three operators are commonly used: (i) Prewitt operator [207], (ii) Sobel operator [244], and (iii) Kirsch operator [124]. These operators differ due to the kernel used which attenuates more or less the noise. Multiple studies used the resulting magnitude and orientation of the edges computed in their classification frameworks [45, 121, 133, 181, 182, 216, 218, 219, 264, 265, 267, 289, 291].

Gabor filters [55, 76] offer an alternative to the usual edge detector, with the possibility to tune the direction and the frequency of the filter to encode a specific pattern. A Gabor filter is defined by the modulation of a Gaussian function with a sine wave which can be further rotated and is formalized as in Eq. 3.29.

$$g(x, y; \theta, \psi, \sigma, \gamma) = \exp\left(-\frac{x'^2 + \gamma^2 y'^2}{2\sigma^2}\right) \cos\left(2\pi \frac{x'}{\lambda} + \phi\right), \quad (3.29)$$

3. REVIEW OF CAD SYSTEMS FOR CAP

with

$$\begin{aligned}x' &= s(x \cos \theta + y \sin \theta) , \\y' &= s(-x \sin \theta + y \cos \theta) ,\end{aligned}$$

where λ is the wavelength of the sinusoidal factor, θ represents the orientation of the Gabor filter, ψ is the phase offset, σ is the standard deviation of the Gaussian envelope, γ is the spatial aspect ratio, and s is the scale factor. In an effort to characterize pattern and texture, a bank of Gabor filters is usually created with different angles, scale, and frequency — refer to Fig. 3.11 — and then convolved with the image. Viswanath et al., Tiwari et al. and more recently Khalvati et al. and Chung et al. have designed a bank of Gabor filters to characterized texture and edge information in T₂-W-MRI and DW-MRI modalities [45, 121, 266, 292].

Texture-based features provide other characteristics discerning CaP from healthy tissue. The most common texture analysis for image classification is based on the gray-level co-occurrence matrix (GLCM) with their related statistics which have been proposed by Haralick et al. in [95]. In a neighborhood around a central voxel, a GLCM is build considering each voxel pair defined by a specific distance and angle. Then, using the GLCM, a set of statistical features is computed as defined in Table 3.7 and assigned to the location of the central voxel. Therefore, N — up to 14 — statistical maps are derived from the GLCM analysis, one per statistics presented in Table 3.7. GLCM is commonly used in CAD systems, on the different MRI modalities, namely T₂-W-MRI, DCE-MRI, or DW-MRI [13, 33, 34, 45, 121, 133, 181, 182, 216, 218, 219, 264, 265, 267, 273, 289, 290, 291, 292]. However, the statistics extracted from the GLCM across studies vary. Along the same line, Rampun et al. extracted from T₂-W-MRI [216, 219] Tamura features [259] composed of three features to characterize texture: (i) coarseness, (ii) contrast, and (iii) directionality.

Lopes et al. used fractal analysis and more precisely a local estimation of the fractal dimension [20], to describe the texture roughness at a specific location. The fractal dimension is estimated through a wavelet-based method in multi-resolution analysis. They showed that cancerous tissues have a higher fractal dimension than healthy tissue.

3.2 Image classification framework

Table 3.7: The 14 statistical features for texture analysis commonly computed from the GLCM p as presented by [95].

Statistical features	Formula
Angular second moment	$\sum_i \sum_j p(i,j)^2$
Contrast	$\sum_{n=0}^{N_g-1} n^2 \left[\sum_{i=1}^{N_g-1} \sum_{j=1}^{N_g-1} p(i,j) \right], i-j = n$
Correlation	$\frac{\sum_i \sum_j (ij)p(i,j) - \mu_x \mu_y}{\sigma_x \sigma_y}$
Variance	$\sum_i \sum_j (i - \mu)^2 p(i,j)$
Inverse difference moment	$\sum_i \sum_j \frac{1}{1+(i-\mu)^2} p(i,j)$
Sum average	$\sum_{i=2}^{2N_g} i p_{x+y}(i)$
Sum variance	$\sum_{i=2}^{2N_g} (i - f_s)^2 p_{x+y}(i)$
Sum entropy	$-\sum_{i=2}^{2N_g} p_{x+y}(i) \log p_{x+y}(i)$
Entropy	$-\sum_i \sum_j p(i,j) \log p(i,j)$
Difference variance	$\sum_{i=0}^{N_g-1} i^2 p_{x-y}(i)$
Difference entropy	$-\sum_{i=0}^{N_g-1} p_{x-y}(i) \log p_{x-y}(i)$
Info. measure of corr. 1	$\frac{S(X;Y) - S_1(X;Y)}{\max(S(X), S(Y))}$
Info. measure of corr. 2	$\sqrt{(1 - \exp[-2(H_2(X;Y) - H(X;Y))])}$
Max. corr. coeff.	$\sqrt{\lambda_2} \text{ , of } Q(i,j) = \sum_k \frac{p(i,k)p(j,k)}{p_x(i)p_y(k)}$

3. REVIEW OF CAD SYSTEMS FOR CAP

Chan et al. described texture using the frequency signature via the discrete cosine transform (DCT)[2] defining a neighbourhood of $7\text{px} \times 7\text{px}$ for modalities used, namely T₂-W-MRI and DW-MRI. The DCT allows to decompose a portion of image into a coefficient space, where few of these coefficients encode the significant information. The DCT coefficients are computed such as:

$$C_{k_1, k_2} = \sum_{m=0}^{M-1} \sum_{n=0}^{N-1} p_{m,n} \cos \left[\frac{\pi}{M} \left(m + \frac{1}{2} \right) k_1 \right] \cos \left[\frac{\pi}{N} \left(n + \frac{1}{2} \right) k_2 \right], \quad (3.30)$$

where C_{k_1, k_2} is the DCT coefficient at the position k_1, k_2 , M and N are the dimension of the neighbourhood and $p_{m,n}$ is the pixel SI at the position $\{m, n\}$.

Viswanath et al. projected T₂-W-MRI images into the wavelet space, using the Haar wavelet, and used the resulting coefficients as features [292]. Litjens et al. computed the texture map based on T₂-W-MRI images using a Gaussian filter bank [153]. Likewise, Rampun et al. employed a rotation invariant filter bank proposed in [140]. The bank is composed of 48 filters including Gaussian filters, first and second derivatives of Gaussian filters as well as Laplacian of Gaussian.

Region-wise detection Unlike the previous section, another strategy is to study a region instead of each pixel independently. Usually, the feature maps are computed using the method presented in voxel-based approach followed by a step in which features are computed in some specific delineated regions to characterize them.

The most common feature type is based on statistics and more specifically the statistic-moments such as mean, standard deviation, kurtosis, and skewness [9, 10, 13, 33, 34, 45, 121, 133, 151, 153, 154, 181, 182, 201, 216, 218, 219, 264, 265, 267, 289, 290, 291, 292]. Additionally, some studies extract additional statistical landmarks based on percentiles [13, 133, 151, 153, 154, 181, 182, 201, 294, 295, 296]. The percentiles to use are manually determined by observing the PDF of the features and checking which values allow the best to differentiate malignant from healthy tissue.

Further statistics are computed through the use of histogram-based features. Liu et al. introduced 4 different types of histogram-based features to characterized

hand-delineated lesions [155]. The first type corresponds to the histogram of the SI of the image. The second type is the HOG [54] which encodes the local shape of the object of interest by using the distribution of the gradient directions. This descriptor is extracted mainly in three steps. First, the gradient image and its corresponding magnitude and direction are computed. Then, the ROI is divided into cells and an oriented-based histogram is generated for each cell. At each pixel location, the orientation of the gradient votes for a bin of the histogram and this vote is weighted by the magnitude of the same gradient. Finally, the cells are grouped into blocks and each block is normalized. The third histogram-based type used in [155] is the shape context introduced in [19]. The shape context is also a way to describe the shape of an object of interest. First, a set of points defining edges have to be detected and for each point of each edge, a log-polar-based histogram is computed using the relative points distribution. The last set of histogram-based feature extracted is based on the framework described in [304] which is using the Fourier transform of the histogram created via local binary pattern (LBP) [187]. LBP is generated by comparing the value of the central pixel with its neighbours, defined through a radius and the number of connected neighbours. Then, in the ROI, the histogram of the LBP distribution is computed. The discrete fourier transform (DFT) of the LBP histogram is used to make the feature invariant to rotation.

Another subset of features are anatomical-based features and have been used in [33, 34, 151, 154, 168]. Litjens et al. computed the volume, compactness, and sphericity related to the given region [151, 154]. Additionally, Litjens et al. also introduced a feature based on symmetry in which they compute the mean of a candidate lesion as well as its mirrored counter-part and compute the quotient as feature [151]. Matulewicz et al. introduced 4 features corresponding to the percentage of tissue belonging to the regions PZ, CG, periurethral region, or outside the prostate region for the considered ROI [168]. Finally, Cameron et al. defined 4 features based on morphology and asymmetry: (i) the difference of morphological closing and opening of the ROI, (ii) the difference of the initial perimeter and the one after removing the high-frequency components, (iii) the difference between the initial ROI and the one after removing the high-frequency components, and (iv)

3. REVIEW OF CAD SYSTEMS FOR CAP

the asymmetry by computing the difference of the two areas splitting the ROI by its major axes [33, 34].

The last group of region-based feature is based on fractal analysis. This group of features is based on estimating the fractal dimension which is a statistical index representing the complexity of the analyzed texture. Lv et al. proposed two features based on fractal dimension: (i) texture fractal dimension and (ii) histogram fractal dimension [160]. The first feature is based on estimating the fractal dimension on the SI of each image and thus this feature is a statistical characteristic of the image roughness. The second fractal dimension is estimated using the PDF of each image and characterizes the complexity of the PDF. Lopes et al. proposed a 3D version to estimate the fractal dimension of a volume using a wavelet decomposition [158].

3.2.2.2 DCE-based features

DCE-MRI is more commonly based on a SI analysis over time as presented in Sect. 2.3. In this section, the features extracted for DCE-MRI analysis are presented.

Whole-spectra approach Some studies are using the whole DCE time series as feature vector [9, 10, 266, 288, 289]. In some cases, the high-dimensional feature space is reduced using dimension reduction methods as it will be presented in the Sect. 3.2.3.

Semi-quantitative approach Semi-quantitative approaches are based on mathematically modelling the DCE time series. The parameters modelling the signal are commonly used, mainly due to the simplicity of their computation [81, 133, 169, 181, 182, 209, 230, 256, 273, 274]. Parameters included in semi-quantitative analysis are summarized in Table 3.8 and also graphically depicted in Fig. 3.12. A set of time features corresponding to specific amplitude level (start, maximum, and end) are extracted. Then, derivative and integral features are also considered as discriminative and are commonly computed.

3.2 Image classification framework

Table 3.8: Parameters used as features for a DCE semi-quantitative analysis in CAD systems.

Semi-quantitative features	Explanations
Amplitude features:	
S_0	Amplitude at the onset of the enhancement
S_{\max}	Amplitude corresponding to 95% of the maximum amplitude
S_p	Amplitude corresponding to the maximum amplitude
S_f	Amplitude at the final time point
Time features:	
t_0	Time at the onset of the enhancement
t_{\max}	Time corresponding to 95% of the maximum amplitude
t_p	Time corresponding to the maximum amplitude
t_f	Final time
t_{tp}	Time to peak which is the time from t_0 to t_p
Derivatives and integral features:	
WI	Wash-in rate corresponding to the signal slope from t_0 to t_m or t_p
WO	Wash-out rate corresponding to the signal slope from t_m or t_p to t_f
$IAUC$	Initial area under the curve which is the area between t_0 to t_f

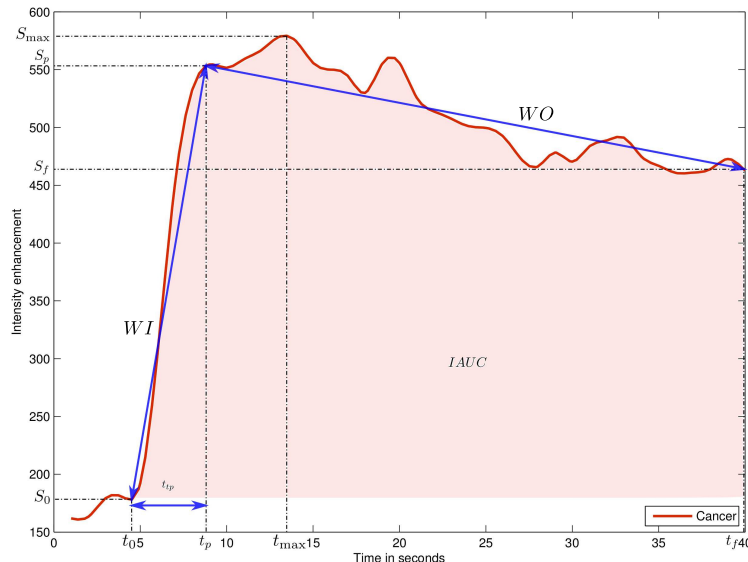


Figure 3.12: Graphical representation of the different semi-quantitative features used for DCE-MRI analysis.

3. REVIEW OF CAD SYSTEMS FOR CAP

Quantitative approach As presented in Chap. 2, quantitative approaches correspond to mathematical-pharmacokinetic models based on physiological exchanges. Four different models have been used in CAD for CaP systems. The most common model reviewed is the *Brix model* [14, 15, 157, 191, 192, 256]. This model is formalized such as:

$$\frac{S(t)}{S(0)} = 1 + Ak_{ep} \left(\frac{\exp(-k_{ep}t) - \exp(-k_{el}t)}{k_{el} - k_{ep}} \right) , \quad (3.31)$$

where $S(\cdot)$ is the DCE signal, A is the parameter simulating the tissue properties, k_{el} is the parameter related to the first-order elimination from the plasma compartment, and k_{ep} is the parameter of the transvascular permeability. The parameters k_{ep} , k_{el} , and A are computed from the MRI data and used as features.

Another model is Tofts model [269] which have been used in [80, 81, 127, 133, 169, 181, 182]. In this model, the DCE signal relative to the concentration is presented as:

$$C_t(t) = v_p C_p(t) + K_{trans} \int_0^t C_p(\tau) \exp(-k_{ep}(t - \tau)) d\tau , \quad (3.32)$$

where $C_t(\cdot)$ is the concentration of the medium, $C_p(\cdot)$ is the AIF which have to be estimated independently, K_{trans} is the parameter related to the diffuse transport of media across the capillary endothelium, k_{ep} is the parameter related to the exchanges back into the vascular space, and v_e is the extravascular-extracellular space fraction defined such that $v_e = 1 - v_p$. In this model, parameters K_{trans} , k_{ep} , and v_e are computed and used as features.

Mazzetti et al. and Giannini et al. used the Weibull function [80, 81, 169] which is formalized as:

$$S(t) = At \exp(-t^B) , \quad (3.33)$$

where A and B are the two parameters which have to be inferred.

They also used another empirical model which is based on the West-like function and named the phenomenological universalities (PUN) [37], formalized as:

$$S(t) = \exp \left[rt + \frac{1}{\beta} a_0 - r (\exp(\beta t) - 1) \right] , \quad (3.34)$$

where the parameters β , a_0 and r are inferred. For all these models, the parameters are inferred using an optimization curve fitting approach.

3.2.2.3 MRSI-based features

Whole spectra approach As in the case of DCE analysis, one common approach is to incorporate the whole MRSI spectra in the feature vector for classification [119, 168, 196, 261, 263, 264, 265, 267, 273, 274, 288]. Sometimes post-processing involving dimension reduction methods is performed to reduce the complexity during the classification as it will be presented in Sect. 3.2.3.

Quantification approach We can reiterate that in MRSI only few biological markers — i.e., choline, creatine, and citrate metabolites — are known to be useful to discriminate CaP and healthy tissue. Therefore, only the concentrations of these metabolites are considered as a feature prior to classification. In order to perform this quantification, 4 different approaches have been used. Kelm et al. used the following models [119]: QUEST [221], AMARES [281], and VARPRO [49]. They are all time-domain quantification methods varying by the type of pre-knowledge embedded and the optimization approaches used to solve the quantification problem. Unlike the time-domain quantification approaches, Parfait et al. used the LcModel approach proposed in [208] which solves the optimization problem in the frequency domain. Although Parfait et al. used each metabolite relative concentration individually [196], other authors such as Kelm et al. proposed to compute relative concentrations as the ratios of metabolites as shown in Eq. 3.35 and Eq. 3.36.

$$R_1 = \frac{[\text{Cho}] + [\text{Cr}]}{[\text{Cit}]} . \quad (3.35)$$

$$R_2 = \frac{[\text{Cit}]}{[\text{Cho}] + [\text{Cr}] + [\text{Cit}]} , \quad (3.36)$$

where Cit, Cho and Cr are the relative concentration of citrate, choline, and creatine, respectively.

Recently Trigui et al. used an absolute quantification approach from which water sequences are acquired to compute the absolute concentration of the metabolites [273, 274]. Absolute quantification using water as reference is based on the

3. REVIEW OF CAD SYSTEMS FOR CAP

Table 3.9: Overview of the feature selection and extraction methods used in CAD systems.

Dimension reduction methods	References
Feature selection:	
Statistical test	[181, 182, 296]
MI-based methods	[45, 121, 133, 181, 182, 293]
Correlation-based methods	[216, 219]
Feature extraction:	
Linear mapping	
PCA	[262, 263]
Non-linear mapping	
Laplacian eigenmaps	[261, 263, 264, 265, 289, 291]
LLE and LLE-based	[262, 263, 288, 289]
Dictionary-based learning	
Sparse coding	[133]
BoW	[215, 217]

fact that the fully relaxed signal from water or metabolites is proportional to the number of moles of the molecules in the voxel [77].

Wavelet decomposition approach Tiwari et al. performed a wavelet packet decomposition [48] of the spectra using the Haar wavelet basis function and use its coefficients as features.

3.2.3 CADx: Feature selection and feature extraction

As presented in the previous section, it is a common practise to extract a wide variety of features. While dealing with mp-MRI, the feature space created is a high-dimensional space which might mislead or corrupt the classifier during the training phase. Therefore, it is of interest to reduce the number of dimensions before proceeding to the classification task. The strategies used can be grouped as: (i) feature selection and (ii) feature extraction. In this section only the methods used in CAD system are presented and summarized in Table 3.9.

3.2.3.1 Feature selection

The feature selection strategy is based on selecting the most discriminative feature dimensions of the high-dimensional space. Thus, the low-dimensional space is then composed of a subset of the original features detected. In this section, methods employed in CAD for CaP detection are presented. A more extensive review specific to feature selection is available in [229].

Niaf et al. make use of the *p*-value by using the independent two-sample *t*-test with equal mean for each feature dimension [181, 182]. In this statistical test, there are 2 classes: CaP and healthy tissue. Hence, for each particular feature, the distribution of each class is characterized by their means \bar{X}_1 and \bar{X}_2 and standard deviation s_{X_1} and s_{X_2} . Therefore, the null hypothesis test is based on the fact that these both distribution means are equal. The *t*-statistic used to verify the null hypothesis is formalized such that:

$$t = \frac{\bar{X}_1 - \bar{X}_2}{s_{X_1 X_2} \cdot \sqrt{\frac{1}{n_1} + \frac{1}{n_2}}}, \quad (3.37)$$

$$s_{X_1 X_2} = \sqrt{\frac{(n_1 - 1)s_{X_1}^2 + (n_2 - 1)s_{X_2}^2}{n_1 + n_2 - 2}},$$

where n_1 and n_2 are the number of samples in each class. From Eq. (3.37), more the means of the class distribution diverge, the larger the *t*-statistic t will be, implying that this particular feature is more relevant and able to make the distinction between the two classes.

The *p*-value statistic is deduced from the *t*-test and corresponds to the probability of obtaining such an extreme test assuming that the null hypothesis is true [88]. Hence, smaller the *p*-value, the more likely the null hypothesis to be rejected the null hypothesis and more relevant the feature is likely to be. Finally, the features are ranked and the most significant features are selected. However, this technique suffers from a main drawback since it assumes that each feature is independent, which is unlikely to happen and introduces a high degree of redundancy in the features selected.

Vos et al. in [296] employed a similar feature ranking approach but make use of the Fisher discriminant ratio to compute the relevance of each feature dimension.

3. REVIEW OF CAD SYSTEMS FOR CAP

Taking the aforementioned formulation, the Fisher discriminant ratio is formalized as the ratio of the interclass variance to the intraclass variance as:

$$F_r = \frac{\bar{X}_1 - \bar{X}_2}{s_{X_1}^2 + s_{X_2}^2} . \quad (3.38)$$

Therefore, a relevant feature dimension is selected when the interclass variance is maximum and the intraclass variance is minimum. Once the features are ordered, the authors select the feature dimensions with the largest Fisher discriminant ratio.

MI is a possible metric to use for selecting a subset of feature dimensions. This method has previously been presented in Sect. 3.1.3 and expressed in Eq. (3.25). Peng et al. introduced two main criteria to select the feature dimensions based on MI: (i) maximal relevance and (ii) minimum redundancy. Maximal relevance criterion is based on the paradigm that the classes and the feature dimension which has to be selected have to share a maximal MI and is formalized as:

$$\arg \max Rel(\mathbf{x}, c) = \frac{1}{|\mathbf{x}|} \sum_{x_i \in \mathbf{x}} MI(x_i, c) , \quad (3.39)$$

where $\mathbf{x} = \{x_i; i = 1, \dots, d\}$ is a feature vector of d dimensions and c is the class considered. As in the previous method, using maximal relevance criterion alone imply an independence between each feature dimension. The minimal redundancy criterion enforce the selection of a new feature dimension which shares as little as possible MI with the previously selected feature dimensions such that:

$$\arg \min Red(\mathbf{x}) = \frac{1}{|\mathbf{x}|^2} \sum_{x_i, x_j \in \mathbf{x}} MI(x_i, x_j) . \quad (3.40)$$

Combination of these two criteria is known as the minimum redundancy maximum relevance (mRMR) algorithm [200]. Two combinations are usually used: (i) the difference or (ii) the quotient. This method has been used at several occasions for the selecting a subset of features prior to classification [45, 121, 133, 181, 182, 292].

add a couple of sentence about correlation-based feature selection used by Ram-pun.

3.2.3.2 Feature extraction

The feature extraction strategy is related to dimension reduction methods but not selecting discriminative features. Instead, these methods aim at mapping the data from the high-dimensional space into a low-dimensional space to maximize the separability between the classes. As in the previous sections, only methods employed in CAD system are reviewed in this section. We refer the reader to [70] for a full review of feature extraction techniques.

PCA is the most commonly used linear mapping method in CAD systems. PCA is based on finding the orthogonal linear transform mapping the original data into a low-dimensional space. The space is defined such that the linear combinations of the original data with the k^{th} greatest variances lie on the k^{th} principal components [114]. The principal components are computed by using the eigenvectors-eigenvalues decomposition of the covariance matrix. Let \mathbf{x} denote the data matrix. Then, the covariance matrix and eigenvectors-eigenvalues decomposition are defined as in Eq. (3.41), and Eq. (3.42), respectively. The eigenvectors-eigenvalues decomposition can be formalized as:

$$\Sigma = \mathbf{x}^T \mathbf{x} . \quad (3.41)$$

$$\mathbf{v}^{-1} \Sigma \mathbf{v} = \Lambda , \quad (3.42)$$

where \mathbf{v} are the eigenvectors matrix and Λ is a diagonal matrix containing the eigenvalues.

It is then possible to find the new low-dimensional space by sorting the eigenvectors using the eigenvalues and finally select the eigenvectors corresponding to the largest eigenvalues. The total variation that is the sum of the principal eigenvalues of the covariance matrix [70], usually corresponds to the 95 % to 98 % of the cumulative sum of the eigenvalues. Tiwari et al. used PCA in order to reduce the complexity of feature space [262, 263, 266].

Non-linear mapping has been also used for dimension reduction and is mainly based on Laplacian eigenmaps and locally linear embedding (LLE) methods. Laplacian eigenmaps also referred as spectral clustering in computer vision, aim to find a low-dimensional space in which the proximity of the data should be preserved

3. REVIEW OF CAD SYSTEMS FOR CAP

from the high-dimensional space [18, 239]. Therefore, two adjacent data points in the high-dimensional space should also be close in the low-dimensional space. Similarly, two distant data points in the high-dimensional space should also be distant in the low-dimensional space. To compute this projection, an adjacency matrix is defined as:

$$W(i, j) = \exp \|\mathbf{x}_i - \mathbf{x}_j\|_2 , \quad (3.43)$$

where \mathbf{x}_i and \mathbf{x}_j are the two samples considered. Then, the low-dimensional space is found by solving the generalized eigenvectors-eigenvalues problem:

$$(D - W)\mathbf{y} = \lambda D\mathbf{y} , \quad (3.44)$$

where D is a diagonal matrix such that $D(i, i) = \sum_j W(j, i)$. Finally the low-dimensional space is defined by the k eigenvectors of the k smallest eigenvalues [18]. Tiwari et al. and Viswanath et al. used this spectral clustering to project their feature vector into a low-dimensional space [261, 263, 264, 289]. The feature space in these studies is usually composed of features extracted from a single or multiple modalities and then concatenated before applying the Laplacian eigenmaps dimension reduction technique.

Tiwari et al. used a slightly different approach by combining the Laplacian eigenmaps techniques with a prior multi-kernel learning strategy [263, 267]. First, multiple features are extracted from multiple modalities. The features of a single modality are then mapped to a higher-dimensional space via the Kernel trick [3], namely a Gaussian kernel. Then, each kernel is linearly combined to obtain a combined kernel K and the adjacency matrix W is computed. Finally, the same scheme as in the Laplacian eigenmaps is applied. However, in order to use the combined kernel, Eq. (3.44) is rewritten as:

$$K(D - W)K^T\mathbf{y} = \lambda KDK^T\mathbf{y} , \quad (3.45)$$

which is solved as a generalized eigenvectors-eigenvalues problem as previously. Viswanath et al. used Laplacian eigenmaps inside a bagging framework in which multiple embeddings are generated by successively selecting feature dimensions [291].

LLE is another common non-linear dimension reduction technique widely used, first proposed in [225]. LLE is based on the fact that a data point in the feature

space is characterized by its neighbourhood. Thus, each data point in the high-dimensional space is transform to represent a linear combination of its k -nearest neighbours. This can be expressed as:

$$\hat{\mathbf{x}}_i = \sum_j W(i, j) \mathbf{x}_j , \quad (3.46)$$

where $\hat{\mathbf{x}}_i$ are the data point estimated using its neighbouring data points \mathbf{x}_j , and W is the weight matrix. The weight matrix W is estimated using a least square optimization as in Eq. (3.47).

$$\begin{aligned} \hat{W} &= \arg \min_W \sum_i |\mathbf{x}_i - \sum_j W(i, j) \mathbf{x}_j|^2 , \\ &\text{subject to } \sum_j W(i, j) = 1 , \end{aligned} \quad (3.47)$$

Then, the essence of LLE is to project the data into a low-dimensional space, while retaining the data saptial organization. Therefore, the projection into the low-dimensional space is tackled as an optimization problem as:

$$\hat{\mathbf{y}} = \arg \min_{\mathbf{y}} \sum_i |\mathbf{y}_i - \sum_j W(i, j) \mathbf{y}_j|^2 . \quad (3.48)$$

This optimization is solved as an eigenvectors-eigenvalues problem by finding the k^{th} eigenvectors corresponding to the k^{th} smallest eigenvalues of the sparse matrix $(I - W)^T(I - W)$.

Tiwari et al. used a modified version of the LLE algorithm in which they applied LLE in a bagging approach with multiple neighbourhood sizes [262]. The different embeddings obtained are then fused using the maximum likelihood (ML) estimation.

Another way of reducing the complexity of high-dimensional feature space is to use the family of so-called dictionary-based methods. Sparse coded features (SCF) representation has become very popular in other computer vision application and has been used by Lehaire et al. in [133]. The main goal of sparse modeling is to efficiently represent the images as a linear combination of a few typical patterns, called atoms, selected from a dictionary. Sparse coding consists of three main steps: (i) dictionary learning and low-level features projection [226].

3. REVIEW OF CAD SYSTEMS FOR CAP

Sparse approximation - Given a dictionary $\mathbf{D} \in \mathbb{R}^{n \times K}$ composed of K atoms and an original signal $\mathbf{y} \in \mathbb{R}^n$ — i.e., one feature vector —, the sparse approximation corresponds to find the sparsest vector $\mathbf{x} \in \mathbb{R}^K$ such that:

$$\arg \min_{\mathbf{x}} \|\mathbf{y} - \mathbf{D}\mathbf{x}\|_2 \quad \text{s.t. } \|\mathbf{x}\|_0 \leq \lambda , \quad (3.49)$$

where λ is a specified sparsity level.

Solving the above optimization problem is an NP-hard problem [65]. However, approximate solutions are obtained using greedy algorithms such as Matching Pursuit (MP) [166] or Orthogonal Matching Pursuit (OMP) [56, 198].

Dictionary learning - As stated previously, the sparse approximation is computed given a specific dictionary \mathbf{D} , which involves a learning stage from a set of training data. This dictionary is learned using K -SVD which is a generalized version of K -means clustering and uses SVD. The dictionary is built, in an iterative manner by solving the optimization problem of Eq. (3.50), by alternatively computing the sparse approximation of \mathbf{X} and the dictionary \mathbf{D} .

$$\arg \min_{\mathbf{D}, \mathbf{X}} \|\mathbf{Y} - \mathbf{D}\mathbf{X}\|_2 \quad \text{s.t. } \|\mathbf{x}_i\|_1 \leq \lambda , \quad (3.50)$$

where \mathbf{Y} is a training set of low-level descriptors, \mathbf{X} is the associated sparse coded matrix — i.e., set of high-level descriptors — with a sparsity level λ , and \mathbf{D} is the dictionary with K atoms. Given \mathbf{D} , \mathbf{X} is computed using the batch-OMP algorithm, while given \mathbf{X} , \mathbf{D} is sequentially updated, one atom at a time using SVD.

Low-level features projection - Once the dictionary is learned, each set of low-level features \mathbf{F}_I previously extracted is encoded using the dictionary \mathbf{D} , solving the optimization problem presented in Eq. (3.49) such that $\mathbf{F}_I \simeq \mathbf{D}\mathbf{X}_I$.

Bag of Words (BoW) approach offer an alternative methods [242] which has been used by Rampun et al. in [215]. This model represents the features by creating a codebook or visual dictionary, from the set of low-level features. The set of low-level features are clustered using k -means to create the dictionary with k clusters known as visual words. Once the codebook created from the training set, the low-level descriptors are replaced by their closest word within the codebook. The final descriptor is a histogram of size k which represents the codebook occurrences for a given mapping.

3.2.4 CADx: Classification

Once the feature vector has been extracted and eventually the complexity reduced, it is possible to make a decision and classify this feature vector to belong to CaP or healthy tissue. Classification methods used in CAD system to distinguish these two classes are summarized in Table 3.10. A full review of classification methods used in pattern recognition is available found in [22].

Rule-based method Lv et al. make use of a decision stump classifier to distinguish CaP and healthy classes [160]. Puech et al. detect CaP by implementing a given set of rules and scores based on a medical support approach [209]. During the testing, the feature vector go through these different rules, and a final score is computed resulting to a final decision.

Clustering methods k -nearest neighbour (k -NN) is one of the simplest supervised machine learning classification methods. In this method, a new unlabelled vector is assigned to the most represented class from its k nearest-neighbours in the feature space. The parameter k is usually an odd number in order to avoid any tie case. k -NN has been one of the method used in [181, 182, 217] mainly to make a comparison with different machine learning techniques. Litjens et al. used this method to roughly detect potential CaP voxels before performing a region-based classification [154].

The k -means algorithm is an unsupervised clustering method in which the data is partitioned into k clusters in an iterative manner. First, k random centroids are defined in the feature space and each data point is assigned to the nearest centroid. Then, the centroid position for each cluster is updated by computing the mean of all the samples belonging to this particular cluster. Both assignment and updating are repeated until the centroids are stable. The number of clusters k is usually defined as the number of classes. This algorithm can also be used for “on-line” learning. In case that new data has to be incorporated, the initial centroid positions correspond to the results of a previous k -means training and is followed by the assignment-updating stage previously explained. Tiwari et al. used k -means in an iterative procedure [261, 263]. Three clusters have been defined

3. REVIEW OF CAD SYSTEMS FOR CAP

Table 3.10: Overview of the classifiers used in CAD systems.

Classifier	References
Rule-based method:	[160, 209]
Clustering methods:	
<i>k</i> -means clustering	[261, 262, 263]
<i>k</i> -NN	[154, 181, 182, 217]
Linear model classifiers:	
LDA	[13, 39, 151, 181, 182, 296]
Logistic regression	[119, 127, 133, 216]
Non-linear classifier:	
QDA	[292]
Probabilistic classifier:	
Naive Bayes	[33, 34, 80, 169, 181, 182, 215, 216, 217, 219]
Ensemble learning classifiers:	
AdaBoost	[151, 158]
RF	[119, 151, 215, 216, 217, 219, 230, 266, 267, 273, 274, 290]
Probabilistic boosting tree	[263, 265, 266]
Kernel method:	
Gaussian processes	[119]
Sparse kernel methods:	
SVM	[14, 15, 39, 45, 81, 121, 133, 153, 154, 155, 158, 181, 182, 191, 192, 196, 201, 256, 266, 274, 293, 294, 295, 296]
RVM	[191, 192]
Neural network:	
Multiple layer perceptron	[168, 196, 219, 273, 274]
Probabilistic neural network	[9, 10, 291]
Graphical model classifiers:	
Markov random field	[157, 192]
Conditional random field	[14, 15, 45]

corresponding to CaP, healthy, and non-prostate. k -means is repeatedly applied and at each iteration, the voxels corresponding to the largest cluster are excluded under the assumption that it is assigned to “non-prostate” cluster. The algorithm stopped when the number of voxels in all remaining clusters are smaller than a given threshold. Tiwari et al. and Viswanath et al. used k -means in a repetitive manner in order to be less sensitive to the centroids initialization [262, 288, 289]. Thus, k clusters are generated T times and the final assignment is performed by majority voting using a co-association matrix as proposed in [71].

Linear model classifiers Linear discriminant analysis (LDA) is used as a classification method in which the optimal linear separation between 2 classes is found by maximizing the inter-class variance and minimizing the intra-class variance [74]. The linear discriminant function is defined as:

$$\delta_k(\mathbf{x}_i) = \mathbf{x}_i^T \Sigma^{-1} \mu_k - \frac{1}{2} \mu_k^T \Sigma^{-1} \mu_k + \log(\pi_k) , \quad (3.51)$$

where \mathbf{x}_i is an unlabelled feature vector, Σ is the covariance matrix of the training data, μ_k is the mean vector of the class k , and π_k is the prior probability of class k . To perform the classification, a sample \mathbf{x}_i is assigned to the class which maximizes the discriminant function as in Eq. (3.52).

$$C(\mathbf{x}_i) = \arg \max_k \delta_k(\mathbf{x}_i) . \quad (3.52)$$

LDA has been used in [13, 39, 181, 182, 296].

Logistic regression is also used to perform binary classification and provides the probability of an observation to belong to a class. The posterior probability of one of the classes, c_1 is written as:

$$p(c_1|\mathbf{x}_i) = \frac{1}{1 + \exp(-\mathbf{w}^T \mathbf{x}_i)} , \quad (3.53)$$

with $p(c_2|\mathbf{x}_i) = 1 - p(c_1|\mathbf{x}_i)$ and where \mathbf{w} is the vector of the regression parameters allowing to obtain a linear combination of the input feature vector \mathbf{x}_i . Thus, an unlabelled observation \mathbf{x}_i is assigned to the class which maximizes the posterior probability as shown in Eq. (3.54).

$$C(\mathbf{x}_i) = \arg \max_k p(C = k|\mathbf{x}_i) . \quad (3.54)$$

3. REVIEW OF CAD SYSTEMS FOR CAP

From Eq. (3.53), one can see that the key to classification using logistic regression model is to infer the set of parameters \mathbf{w} through a learning stage using a training set. This vector of parameters \mathbf{w} is inferred by estimating the maximum likelihood. This step is performed through an optimization scheme, using a quasi-Newton method [32], which seeks in an iterative manner for the local minimum in the derivative of Eq. (3.53). This method has been used to create a linear probabilistic model in [119, 133, 209, 216].

Non-linear model classifier Viswanath et al. used quadratic discriminant analysis (QDA) instead of LDA [292]. Unlike in LDA in which one assumes that the class covariance matrix Σ is identical for all classes, a covariance matrix Σ_k specific to each class is computed. Thus, Eq. (3.51) becomes:

$$\delta_k(\mathbf{x}_i) = \mathbf{x}_i^T \Sigma_k^{-1} \boldsymbol{\mu}_k - \frac{1}{2} \boldsymbol{\mu}_k^T \Sigma_k^{-1} \boldsymbol{\mu}_k + \log(\pi_k) . \quad (3.55)$$

The classification scheme in the case of the QDA is identical to Eq. (3.52).

Probabilistic classifiers The most commonly used classifier is the naive Bayes classifier which is a probabilistic classifier assuming independence between each feature dimension [222]. This classifier is based on Bayes' theorem:

$$p(C = k|\mathbf{x}) = \frac{p(C)p(\mathbf{x}|C)}{p(\mathbf{x})} , \quad (3.56)$$

where $p(C = k|\mathbf{x})$ is the posterior probability, $p(C)$ is the prior probability, $p(\mathbf{x}|C)$ is the likelihood, and $p(\mathbf{x})$ is the evidence. However, the evidence term is usually discarded since it is not class dependent and plays the role of a normalization term. Hence, in a classification scheme, an unlabelled observation is classified to the class which maximizes the posterior probability as:

$$C(\mathbf{x}_i) = \arg \max_k p(C = k|\mathbf{x}_i) , \quad (3.57)$$

$$p(C = k|\mathbf{x}_i) = p(C = k) \prod_{j=1}^n p(x_{ij}, |C = k) , \quad (3.58)$$

where d is the number of dimensions of the feature vector $\mathbf{x}_i = \{x_{i1}, \dots, x_{id}\}$. Usually, a model includes both the prior and likelihood probabilities and it is common to use an equal prior probability for each class or eventually a value based on the relative frequency derived from the training set. Regarding the likelihood probability, it is common to choose a Gaussian distribution to characterize each class. Thus, each class is characterized by two parameters: (i) the mean and (ii) the standard deviation. These parameters are inferred from the training set by using the maximum likelihood estimation (MLE) approach. The naive Bayes classifier has been used in [33, 34, 80, 169, 181, 182, 182, 215, 216, 217, 219].

Ensemble learning classifiers AdaBoost is an adaptive method based on an ensemble learning method and initially proposed in [73]. AdaBoost linearly combines several weak learners resulting into a final strong classifier. A weak learner is defined as a classification method performing slightly better than a random classifier. Popular choices regarding the weak learner classifiers are: decision stump or decision tree learners such as iterative dichotomiser 3 (ID3) [210], C4.5 [211], and classification and regression tree (CART) [27].

AdaBoost is considered as an adaptive method in the way that the weak learners are selected. The selection is performed in an iterative manner. At each iteration t , the weak learner selected h_t corresponds to the one minimizing the classification error on a distribution of weights D_t , that is associated with the training samples. Each weak learner is assigned a weight α_t as:

$$\alpha_t = \frac{1}{2} \ln \frac{1 - \epsilon_t}{\epsilon_t} , \quad (3.59)$$

where ϵ_t corresponds to the classification error rate of the weak learner on the distribution of weight D_t .

Before performing a new iteration, the distribution of weights D_t is updated such that the weights associated with the misclassified samples by h_t increase and the weights of well classified samples decrease as shown in Eq. (3.60).

$$D_{t+1}(i) = \frac{D_t(i) \exp(-\alpha_t y_i h_t(\mathbf{x}_i))}{Z_t} , \quad (3.60)$$

3. REVIEW OF CAD SYSTEMS FOR CAP

where \mathbf{x}_i is the i^{th} sample corresponding to class y_i and Z_t is a normalization factor forcing D_{t+1} to be a probability distribution. This procedure allows to select a weak learner at the next iteration $t + 1$ which will classify in priority the previous misclassified samples. Thus, after T iterations, the final strong classifier corresponds to the linear combination of the weak learners selected and the classification is performed such that:

$$C(\mathbf{x}_i) = \text{sign} \left(\sum_{t=1}^T \alpha_t h_t(\mathbf{x}_i) \right). \quad (3.61)$$

Lopes et al. make use of the AdaBoost classifier to perform their classification [158] while Litjens et al. used the GentleBoost variant [75] which provides a modification of the function affecting the weight at each weak classifier [151].

random forest (RF) is a classification method which is based on creating an ensemble of decision trees and was introduced in [26]. In the learning stage, multiple decision tree learners [27] are trained. However, each decision tree is trained using a different dataset. Each of these datasets corresponds to a bootstrap sample generated by randomly choosing n samples with replacement from the initially N samples available [63]. Then, randomization is also part of the decision tree growth. At each node of the decision tree, from the bootstrap sample of D dimensions, a number of $d \ll D$ dimensions will be randomly selected. Finally, the d^{th} dimension in which the classification error is minimum is used. This best “split” classifier is often evaluated using MI or Gini index. Finally, each tree is grown as much as possible without using any pruning procedure. In the prediction stage, the unlabelled sample is introduced in each tree and each of them assign a class. Finally, it is common to use a majority voting approach to choose the final class label. The RF classifier has been used in [119, 151, 215, 216, 217, 219, 230, 266, 267, 273, 274, 290].

Probabilistic boosting-tree is another ensemble learning classifier which shares principles with AdaBoost but using them inside a decision tree [275]. In the training stage, the probabilistic boosting-tree method grows a decision tree and at each node, a strong classifier is learned in an almost comparable scheme to AdaBoost. Once the strong learner is trained, the training set is split into two subsets which are used to train the next strong classifiers in the next descending

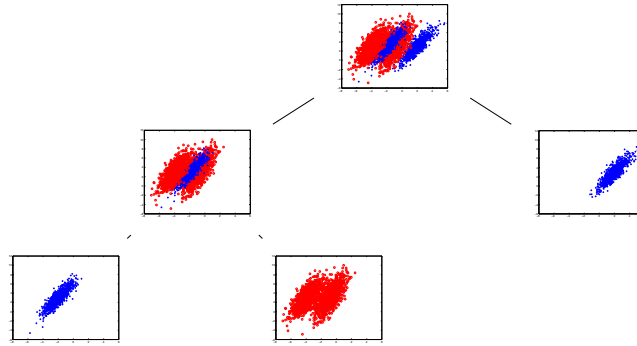


Figure 3.13: Representation of the capabilities of the probabilistic boosting-tree algorithm to split at each node of the tree the positive and negative samples.

nodes. Thus, three cases are conceivable to decide in which branch to propagate each sample training \mathbf{x}_i :

- if $q(+1, \mathbf{x}_i) - \frac{1}{2} > \epsilon$ then \mathbf{x}_i is propagated to the right branch set and a weight $w_i = 1$ is assigned.
- if $q(-1, \mathbf{x}_i) - \frac{1}{2} > \epsilon$ then \mathbf{x}_i is propagated to the left branch set and a weight $w_i = 1$ is assigned.
- else \mathbf{x}_i will be propagated in both branches with $w_i = q(+1, \mathbf{x}_i)$ in the right branch and $w_i = q(-1, \mathbf{x}_i)$ in the left branch.

with $\mathbf{w} = w_i, i = \{1, \dots, N\}$ corresponding to distribution of weights, N the number of samples as in AdaBoost and $q(\cdot)$ is defined as:

$$q(+1, \mathbf{x}_i) = \frac{\exp(2H(\mathbf{x}_i))}{1 + \exp(2H(\mathbf{x}_i))}, \quad (3.62)$$

$$q(-1, \mathbf{x}_i) = \frac{\exp(-2H(\mathbf{x}_i))}{1 + \exp(-2H(\mathbf{x}_i))}. \quad (3.63)$$

Employing such a scheme tends to divide the data in such a way that positive and negative samples are naturally split as shown in Eq. 3.13. In the classification stage, the unlabelled sample \mathbf{x} is propagated through the tree, where at each node, it is classified by each strong classifier previously learned and where an estimation

3. REVIEW OF CAD SYSTEMS FOR CAP

of the posterior distribution is computed. The posterior distribution corresponds to the sum of the posterior distribution at each node of the decision tree. The probabilistic boosting-tree classifier has been used in [264, 265, 266, 291].

Kernel method A Gaussian process for classification is a kernel method in which it is assumed that the data can be represented by a single sample from a multivariate Gaussian distribution [220]. In the case of linear logistic regression for classification, the posterior probability is expressed as:

$$\begin{aligned} p(y_i|\mathbf{x}_i, \mathbf{w}) &= \sigma(y_i f(\mathbf{x}_i)) , \\ f(\mathbf{x}_i) &= \mathbf{x}_i^T \mathbf{w} , \end{aligned} \quad (3.64)$$

where $\sigma(\cdot)$ is the logistic function and \mathbf{w} are the parameters vector of the model. Thus, the classification using Gaussian processes is based on assigning a Gaussian process prior over the function $f(\mathbf{x})$ which is characterized by a mean function \bar{f} and covariance function K . Therefore, in the training stage, the best mean and covariance functions have to be inferred in regard to our training data using a Newton optimization and a Laplacian approximation. The prediction stage is performed in two stages. First, for a new observation \mathbf{x}_* , the corresponding probability $p(f(\mathbf{x}_*)|f(\mathbf{x}))$ is computed such that:

$$\begin{aligned} p(f(\mathbf{x}_*)|f(\mathbf{x})) &= \mathcal{N}(K_* K^{-1} \bar{f}, K_{**} - K_*(K')^{-1} K_*^T) , \\ K' &= K + W^{-1} , \\ W &= \nabla \nabla \log p(\mathbf{y}|f(\mathbf{x})) , \end{aligned} \quad (3.65)$$

where K_{**} is the variance of the testing sample \mathbf{x}_* , K_* is the covariance of training-testing samples \mathbf{x} and \mathbf{x}_* . Then, the function $f(\mathbf{x}_*)$ is squashed using the sigmoid function and the probability of the class membership is defined such that:

$$C(\mathbf{x}_*) = \sigma \left(\frac{\bar{f}(\mathbf{x}_*)}{\sqrt{1 + \text{var}(f(\mathbf{x}_*))}} \right) . \quad (3.66)$$

Only Kelm et al. used Gaussian process for classification of MRSI data [119].

Sparse kernel methods In a classification scheme using Gaussian processes, when a prediction is performed, the whole training data are used to assign a label to the new observations. That is why this method is also called kernel method. Sparse kernel category is composed of methods which rely only on a few labelled observations of the training set to assign the label of new observations [22].

Support vector machines (SVM) is a sparse kernel method aiming at finding the best linear hyper-plane — non-linear separation is discussed further — which separates 2 classes such that the margin between the two classes is maximized [282]. The margin is in fact the region defined by 2 hyper-planes splitting the 2 classes, such that there is no points lying in between. The distance between these 2 hyper-planes is equal to $\frac{2}{\|\mathbf{w}\|}$ where \mathbf{w} is the normal vector of the hyper-plane splitting the classes. Thus, maximizing the margin is equivalent to minimizing the norm $\|\mathbf{w}\|$. Hence, this problem is solved by an optimization approach and formalized as:

$$\begin{aligned} \arg \min_{\mathbf{w}} \quad & \frac{1}{2} \|\mathbf{w}\|^2, \\ \text{subject to} \quad & y_i(\mathbf{w} \cdot \mathbf{x}_i - b) \geq 1, \quad i = \{1, \dots, N\}, \end{aligned} \quad (3.67)$$

where \mathbf{x}_i is a training sample with corresponding class label y_i . From Eq. (3.67), it is important to notice that only few points from the set of N points are selected which later define the hyper-plane. This constraint is imposed in the optimization problem using Lagrange multipliers α . All points which are not lying on the margin are assigned a corresponding $\alpha_i = 0$, which is formalized as Eq. (3.68).

$$\arg \min_{\mathbf{w}, b} \max_{\alpha \geq 0} \left\{ \frac{1}{2} \|\mathbf{w}\|^2 - \sum_{i=1}^n \alpha_i [y_i(\mathbf{w} \cdot \mathbf{x}_i - b) - 1] \right\}. \quad (3.68)$$

The different parameters are inferred using quadratic programming. This version of SVM is known as hard-margin since no points can lie in the margin area. However, it is highly probable not to find any hyper-plane splitting the classes such as specified previously. Thus, a soft-margin optimization approach has been proposed [51], where points have the possibility to lie on the margin but at the

3. REVIEW OF CAD SYSTEMS FOR CAP

cost of a penalty ξ_i which is minimized in the optimization process such that:

$$\arg \min_{\mathbf{w}, \xi, b} \max_{\boldsymbol{\alpha}, \boldsymbol{\beta}} \left\{ \frac{1}{2} \|\mathbf{w}\|^2 + C \sum_{i=1}^n \xi_i - \sum_{i=1}^n \alpha_i [y_i(\mathbf{w} \cdot \mathbf{x}_i - b) - 1 + \xi_i] - \sum_{i=1}^n \beta_i \xi_i \right\} . \quad (3.69)$$

The decision to assign the label to a new observation \mathbf{x}_i is taken such that:

$$C(\mathbf{x}_i) = \text{sign} \left(\sum_{n=1}^N \alpha_n (\mathbf{x}_n \cdot \mathbf{x}_i) + b_0 \right) , \quad (3.70)$$

where $\mathbf{x}_n | n = \{1, \dots, S\}$, S being the support vectors.

SVM can also be used as a non-linear classifier by performing a Kernel trick [24]. The original data \mathbf{x} is projected to a high-dimensional space in which it is assumed that a linear hyper-plane splits the 2 classes. Different kernels are popular such as the RBF kernel, polynomial kernels, or sigmoid kernel. In CAD for CaP systems, SVM is the most popular classification method and has been used in a multitude of research works [14, 15, 39, 45, 81, 121, 133, 153, 154, 155, 158, 181, 182, 191, 192, 196, 201, 256, 266, 274, 293, 294, 295, 296].

Relevant vector machine (RVM) is a sparse version of Gaussian process previously presented, proposed in [260]. RVM is identical to a Gaussian process with the following covariance function [212]:

$$K_{RVM}(\mathbf{x}_p, \mathbf{x}_q) = \sum_{j=1}^M \frac{1}{\alpha_j} \Phi_j(\mathbf{x}_p) \Phi_j(\mathbf{x}_q) , \quad (3.71)$$

where $\phi(\cdot)$ is a Gaussian basis function, $\mathbf{x}_i | i = \{1, \dots, N\}$ are the N training points, and $\boldsymbol{\alpha}$ are the weights vector. As mentioned in [212], the sparsity regarding the relevance vector arises if $j\alpha_j^{-1} = 0$. The set of weights $\boldsymbol{\alpha}$ is inferred using the expectation maximization algorithm. Ozer et al. use RVM and make a comparison with SVM for the task of CaP detection [191, 192].

Neural network Multilayer perceptron is a feed-forward neural networks considered as the most successful model of this kind in pattern recognition [22]. The

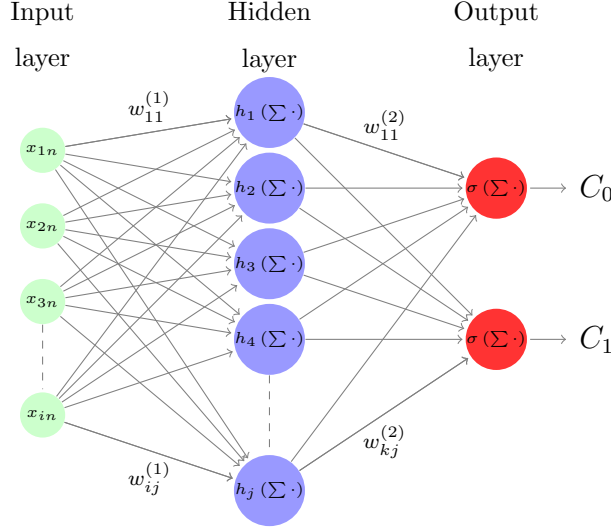


Figure 3.14: Representation of a neural network of the multilayer perceptron family.

most well known model used is based on 2 layers where a prediction of an observation is computed as:

$$C(\mathbf{x}_n, w_{ij}^{(1)}, w_{kj}^{(2)}) = \sigma \left[\sum_{j=0}^M w_{kj}^{(2)} h \left(\sum_{i=0}^D w_{ij}^{(1)} x_{in} \right) \right], \quad (3.72)$$

where $h(\cdot)$ and $\sigma(\cdot)$ are 2 activation functions usually non-linear, $w_{ij}^{(1)}$ and $w_{kj}^{(2)}$ are the weights associated with the linear combination with the input feature \mathbf{x}_n and the hidden unit.

A graphical representation of this network is presented in Eq. 3.14. Relating Fig. 3.14 with Eq. (3.72), it can be noted that this network is composed of some successive non-linear mapping of the input data. First, a linear combination of the input vector \mathbf{x}_n is mapped into some hidden units through a set of weights $w_{ij}^{(1)}$. This combination becomes non-linear by the use of the activation function $h(\cdot)$ which is usually chosen to be a sigmoid function. Then, the output of the networks consists of a linear combination of the hidden units and the set of weights $w_{kj}^{(2)}$. This combination is also mapped non-linearly using an activation function $\sigma(\cdot)$ which is usually a logistic function. Thus, the training of such a network

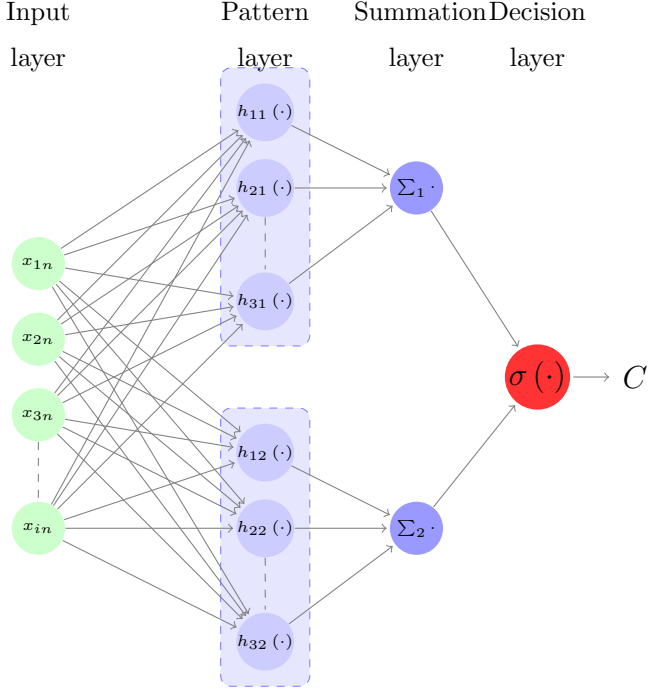


Figure 3.15: Representation of a neural network of the probabilistic neural network family.

resides in finding the best weights $w_{ij}^{(1)}$ and $w_{kj}^{(2)}$ which model the best the training data. The error of this model is computed as:

$$E(w_{ij}^{(1)}, w_{kj}^{(2)}) = \frac{1}{2} \sum_{n=1}^N \left(C(\mathbf{x}_n, w_{ij}^{(1)}, w_{kj}^{(2)}) - y(\mathbf{x}_n) \right)^2, \quad (3.73)$$

where $\mathbf{x}_n | n = \{1, \dots, N\}$ are the N training vectors with their corresponding class label $y(\mathbf{x}_n)$.

Therefore, the best set of weights is inferred in an optimization framework where the error $E(\cdot)$ needs to be minimized. This optimization is performed using a gradient descent method where the derivative of Eq. (3.73) is computed using the back-propagation algorithm proposed by [228]. This type of network has been used multiple times [168, 196, 219, 273, 274].

Probabilistic neural networks are another type of feed-forward networks which is derived from the multilayer perceptron case and has been proposed by [247].

This classifier is modelled by changing the activation function $h(\cdot)$ in Eq. (3.72) to an exponential function such that:

$$h(\mathbf{x}_n) = \exp \left(-\frac{(\mathbf{w}_j - \mathbf{x})^T (\mathbf{w}_j - \mathbf{x})}{2\sigma^2} \right) , \quad (3.74)$$

where σ is a free parameter set by the user.

The other difference of the probabilistic neural networks compared with the multilayer perceptron networks resides in the architecture as shown in Fig. 3.15. This network is formed by 2 hidden layers. The first hidden layer consists of the pattern layer, in which the mapping is done using Eq. (3.74). This pattern layer is sub-divided into a number of groups corresponding to the number of classes. The second hidden layer corresponds to the summation layer which simply sums the output of each sub-group of the pattern layer. This method is used in [9, 10, 291].

Graphical model classifiers Markov random field (MRF) is used as a lesion segmentation method to detect CaP. First, let define s as a pixel which belongs to a certain class denoted by ω_s . The labelling process is defined as $\omega = \{\omega_s, s \in I\}$ where I is the set of all the pixels inside the image. The observations corresponding to SI in the image are noted $\mathcal{F} = \{f_s | s \in I\}$. Thus, the image process \mathcal{F} represents the deviation from the labelling process ω [117]. Hence, lesion segmentation is equivalent to estimating the best $\hat{\omega}$ which maximizes the posterior probability $p(\omega|\mathcal{F})$. Thus, using a Bayesian approach, this problem is formulated such that:

$$p(\omega|\mathcal{F}) = \arg \max_{\omega} \prod_{s \in I} p(f_s|\omega_s) p(\omega) . \quad (3.75)$$

It is generally assumed that $p(f_s|\omega_s)$ follows a Gaussian distribution and that the pixels classes $\lambda = \{1, 2\}$ for a binary classification are characterized by their respective mean μ_λ and standard deviation σ_λ . Then, ω is a Markov random field, thus:

$$p(\omega) = \frac{1}{Z} \exp(-U(\omega)) , \quad (3.76)$$

where Z is a normalization factor to obtain a probability value, $U(\cdot)$ is the energy function.

3. REVIEW OF CAD SYSTEMS FOR CAP

Table 3.11: Overview of the model validation techniques used in CAD systems.

Model validation techniques	References
LOOCV	[9, 10, 13, 14, 15, 33, 34, 39, 45, 80, 119, 121, 133, 151, 154, 169, 181, 182, 191, 192, 201, 209, 267, 291, 293, 295]
k -CV	[153, 196, 215, 216, 217, 218, 219, 263, 264, 265, 266, 273, 274, 290, 292, 296]

Thus, the segmentation problem is solved as an optimization problem where the energy function $U(\cdot)$ has to be minimized. There are different possibilities to define the energy function $U(\cdot)$. However, it is common to define the energy function such that it combines two types of potential function: (i) a local term relative to the pixel itself and (ii) a smoothing prior which embeds neighbourhood information which penalizes the energy function affecting the region homogeneity. This optimization of such a function can be performed using an algorithm such as iterated conditional modes [117]. Liu et al. and Ozer et al. used MRF as an unsupervised method to segment lesions in mp-MRI images [157, 192]. Artan et al. and Chung et al. used conditional random fields instead of MRF for MRI segmentation [14, 15, 45]. The difference between these 2 methods resides in the fact that conditional probabilities are defined such as:

$$p(\omega|\mathcal{F}) = \frac{1}{Z} \exp \left[- \sum_{s \in I} V_{C1}(\omega_s|\mathcal{F}) - \sum_{\{s,r\} \in C} V_{C2}(\omega_s, \omega_r|\mathcal{F}) \right]. \quad (3.77)$$

$V_{C1}(\cdot)$ is the state (or partition) feature function and $V_{C2}(\cdot)$ is the transition (or edge) feature function [118].

3.2.5 Model validation

In pattern recognition, the use of model validation techniques to assessing the performance of a classifier plays an important role for reporting results. Two techniques are broadly used in the development of CAD system and are summarized in Table 3.11. The most popular technique used in CAD systems is the leave-one-out cross-validation (LOOCV) technique. From the whole data, one patient is kept for validation and the other cases are used for training. This manipulation is repeated

Table 3.12: Overview of the evaluation metrics used in CAD systems.

Evaluation metrics	References
Accuracy	[14, 15, 157, 256, 266]
Sensitivity - Specificity	[14, 15, 33, 34, 80, 121, 157, 158, 169, 191, 192, 196, 201, 230, 262, 263, 273, 274, 288, 289]
ROC - AUC	[10, 13, 39, 80, 81, 119, 127, 133, 155, 158, 160, 168, 169, 181, 182, 201, 215, 216, 217, 218, 219, 264, 265, 266, 267, 290, 291, 292, 293, 294, 295]
FROC	[153, 154, 296]
Dice's coefficient	[14, 15, 157, 191]

until each patient has been used for validation. This technique is popular when working with a limited number of patients, allowing to train on representative number of cases even with a small dataset. However, LOOCV cross-validation suffers from a large variance and is considered as an unreliable estimate [64].

The other technique is the k -fold cross-validation (k -CV) technique which is based on splitting the dataset into k subsets where the samples are randomly selected. Then, one fold is kept for testing and the remaining subsets are used for training. The classification is then repeated as in the LOOCV technique. In fact leave-one-out cross-validation (LOOCV) is a particular case of k -fold cross-validation (k -CV) when k equals the number of patients. In the reviewed papers, the typical values used for k has been set to three and five. k -fold cross-validation (k -CV) is regarded as more appropriate than leave-one-out cross-validation (LOOCV), but the number of patients in the dataset needs to be large enough for the results to be meaningful.

3.2.6 Evaluation measure

Several metrics are used in order to assess the performance of a classifier and are summarized in Table 3.12. Voxels in the MRI image are classified into healthy or malign tissue and compared with a ground-truth. This allows to compute a confusion matrix by counting true positive (TP), true negative (TN), false positive (FP), and false negative (FN) samples. From this analysis, different statistics are extracted.

The first statistic used is the accuracy which is computed as the ratio of true detection to the number of samples. However, depending on the strategy employed

3. REVIEW OF CAD SYSTEMS FOR CAP

in the CAD work-flow, this statistic is highly biased by a high number of true negative samples which boost the accuracy score overestimating the actual performance of the classifier. That is why, the most common statistic computed are sensitivity and specificity defined in Eq. (3.78) and Eq. (3.79), respectively. The metrics give a full overview of the performance of the classifier.

$$\text{SEN} = \frac{\text{TP}}{\text{TP} + \text{FN}} , \quad (3.78)$$

$$\text{SPE} = \frac{\text{TN}}{\text{TN} + \text{FP}} . \quad (3.79)$$

These statistics are also used to compute the receiver operating characteristic (ROC) curves [173], which give information about voxel-wise classification. This analysis represents graphically the sensitivity as a function of $(1 - \text{specificity})$, which is in fact the false positive rate, by varying the discriminative threshold of the classifier. By varying this threshold, more true negative samples are found but often at the cost of detecting more false negatives. However, this fact is interesting in CAD since it is possible to obtain a high sensitivity and to ensure that no cancers are missed even if more false alarms have to be investigated or the opposite. A statistic derived from ROC analysis is the area under the curve (AUC) which corresponds to the area under the ROC and is a measure used to make comparisons between models.

The free-response receiver operating characteristic (FROC) extends the ROC analysis but to a lesion-based level. The same confusion matrix is computed where the sample are not pixels but lesions. However, it is important to define what is a true positive sample in that case. Usually, a lesion is considered as a true positive sample if the region detected by the classifier overlaps “sufficiently” the one delineated in the ground-truth. However, “sufficiently” is a subjective measure defined by each researcher and can correspond to one pixel only. However, an overlap of 30 % to 50 % is usually adopted. Finally, in addition to the overlap measure, the Dice’s coefficient is often computed to evaluate the accuracy of the lesion localization. This coefficient consists of the ratio between twice the number

of pixels in common and the sum of the pixels of the lesions in the ground-truth GT and the output of the classifier S, defined as shown in Eq. (3.80).

$$Q_D = \frac{2|GT \cap S|}{|GT| + |S|} . \quad (3.80)$$

3.3 Discussion

3.3.1 Results reported

As discussed previously in Sect. 3.2.6, different metrics have been used to report results. A comparison of the different methods reviewed is given depending on the metric used in field of research and also the type of MRI scanner used, i.e. 1.5 T or 3 T. For each field, the *best classification performance* obtained in each study have been reported in these figures. The results in terms of AUC-ROC are depicted in Fig. 3.17. The results vary from 71 % to 97 % for some experiments with a 1.5 T MRI scanner and from 77 % to 95 % with a 3 T MRI scanner.

The results in regard of sensitivity and specificity are reported in Fig. 3.18. In the case that the data have been collected with a 1.5 T MRI scanner, the sensitivity ranges from 74 % to 100 % and the specificity from 43 % to 93 %. For the experiments carried out with a 3 T MRI scanner, the sensitivity varies from 60 % to 99 % and the specificity from 66 % to 100 %. Four studies also use FROC analysis to report their results and are reported in Fig. 3.16.

3.3.2 Comparison

We would like to stress the following findings drawn during the review of the different studies:

1. Quantitatively, it is difficult to make a fair comparison between the different studies reviewed. Different factors come into play to elucidate this fact. Mainly a lack of standardization has to be pointed out in regard to experimental evaluation: (i) different datasets are used during the evaluation of the frameworks developed hindering an inter-study comparison. The same conclusion has been recently drawn by [151] supporting this argument; (ii)

3. REVIEW OF CAD SYSTEMS FOR CAP

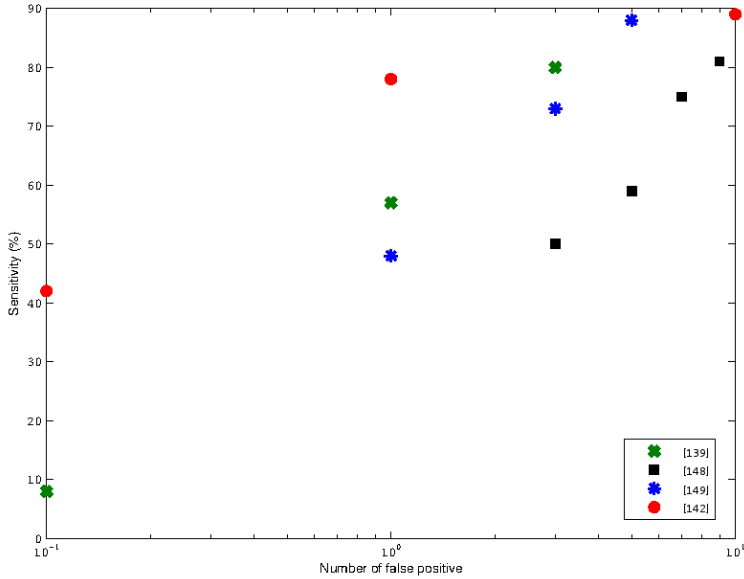


Figure 3.16: Comparison in terms of FROC of the methods using data from 3 T MRI scanner.

the experimental results are not reported with a common metric which leads to the inability to compare the different studies.

2. However, multiple studies reported some performance improvements using mp-MRI techniques instead of mono-parametric imaging techniques. Considering only the most recent studies proposing CADe-CADx frameworks, the following results can be highlighted. Viswanath et al. obtained an AUC of 77% using an ensemble learning approach combining the features from the three MRI modalities — i.e., T₂-W-MRI, DCE-MRI, and DW-MRI, while the results obtained as standalone modality range from 62% to 65% [291]. Tiwari et al. drawn similar conclusions by using T₂-W-MRI and MRSI modalities as both in standalone and multi-parametric frameworks with an improved AUC ranging from 57%-76% to 85% [267]. The most recent work of Litjens et al. obtained an improved AUC metric from 71%-76% considering each modality separately — i.e., T₂-W-MRI, DCE-MRI, and DW-MRI — to 89% in their mp-MRI framework.

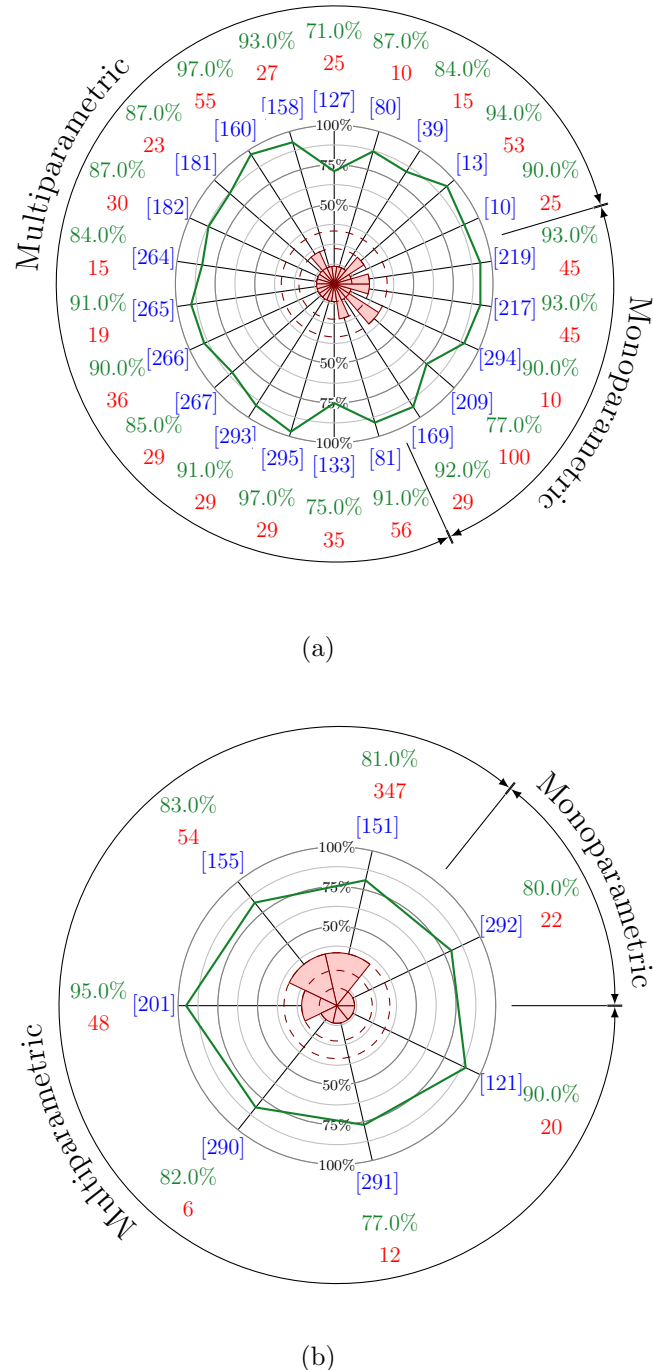


Figure 3.17: Numerical and graphical comparison of the results in terms of AUC for 1.5 T and 3 T MRI scanners. The green value represents the metric and are graphically reported in the green curve in the center of the figure. The red value and areas correspond to the number of patients in the dataset. The numbers between brackets in blue correspond to the reference as reported in Table 3.1.

3. REVIEW OF CAD SYSTEMS FOR CAP

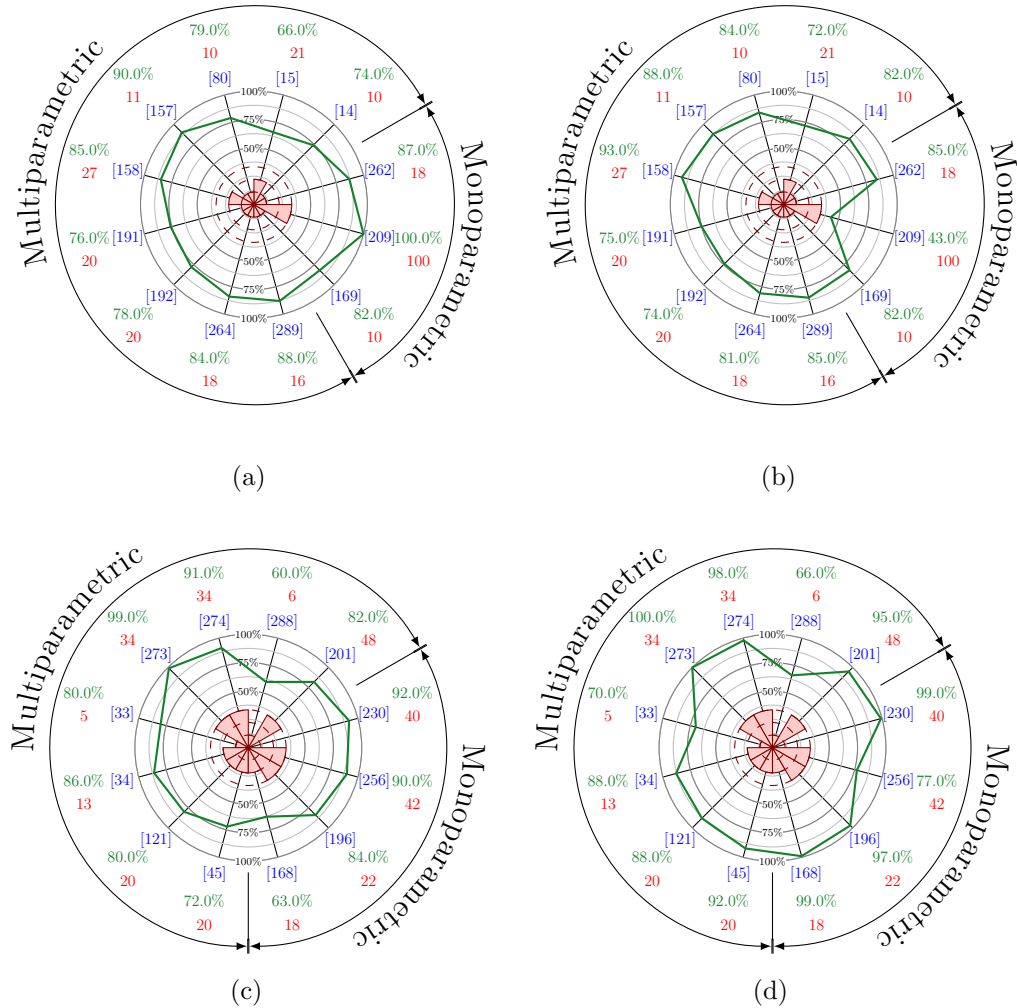


Figure 3.18: Numerical and graphical comparison of the results in terms of SE (a), (c) and SP (b), (d) for 1.5 T and 3 T MRI scanners. The value in green represents the metric and are graphically reported in the green curve in the center of the figure. The red value and areas correspond to the number of patients in the dataset. The numbers between brackets in blue correspond to the reference as reported in Table 3.1.

3. The studies comparing particular combination of more than a single modality give rise to the same fact [151, 153, 155, 192]: using 3 modalities lead to better performances than using any combination of 2 modalities.
4. Unlike the previous remark 2, no straightforward conclusions can be given regarding the classification performance using each modality in a standalone framework. The modality being processed by different methods, it does not allow us to conclude if a modality by itself is more suited than another. However, we are able to distinguish some interesting trends which deserves the attention of the community. Tiwari et al. in [264, 266, 267] observed that MRSI is a more suitable modality than T_2 -W to highlight CaP. Moreover, ADC maps have shown a better discriminative power than T_2 -W as well [127, 201, 291]. Lately, Litjens et al. observed that DW-MRI modality is more suitable than both DCE-MRI and T_2 -W-MRI to distinguish CaP in their CADx system [151]. Recently, Rampun et al. showed, however, some promising results using T_2 -W-MRI only in conjunction with textons and BoW; this study should be transposed to other MRI modalities [217].
5. Furthermore, mp-MRI has attracted the attention of both radiologists and computer vision researchers. Indeed, pioneer research groups included new modalities over years when at the same time, new research groups directly introduced mp-MRI CAD systems. These facts lead us to think that CaP researches will benefit from mp-MRI techniques.
6. When focusing on the different modalities used, it can be pointed out that only Trigui et al. reported the use of all modalities in a single framework by incorporating the MRSI modality [273, 274]. Although the results reported are promising, the detection has been performed at MRSI scale and further investigations need to be carried out. Nevertheless, MRSI has shown some overall good classification performance at the price of a lower resolution as well as an increased acquisition time. Moreover, MRSI analysis is more complex in comparison with the other modalities. To our mind, MRSI could contribute in a mp-MRI framework and should be fused with the other modalities.

3. REVIEW OF CAD SYSTEMS FOR CAP

7. Lately, 3 studies focused on developing a region-based classification in which PZ and CG will be analyzed separately [151, 154, 292]. The promising obtained results indicate that this strategy should be further investigated.
8. Recent studies are using quantitative features in addition to SI. It seems that these quantitative features provide uncorrelated information with respect to SI features and should lead to better classification performance when combined all together.
9. Regarding the methods used in the “image regularization” — i.e., pre-processing, segmentation, and registration — it is particularly difficult to distinguish the benefit of a method over another since none of the studies focus on making comparison of these processing stages. The focus is usually entirely based on the “image classification” framework where different methods are directly compared. Note that the performance of a classifier is highly linked with the features vector extracted from particular data. Hence, one can not conclude that a machine learning method is more appropriate than another, but we can identify a trend in which SVM as well as ensemble learning classifiers — i.e., AdaBoost, GentleBoost, and RF — seem to perform better than neural network, LDA, or Naive Bayes.
10. We would like to draw the attention of the reader on the feature extraction/selection stage. This processing could reduce the complexity and also allow to find a better feature space for classification. However, few studies are performing such approaches. Niaf et al., Khalvati et al., Chung et al., and Rampun et al. are successfully applying a scheme to reduce the number of dimensions by selecting the most discriminative features [45, 121, 181, 182, 216, 219]. It allows them to obtain improved performances compared with a classification performed with their initial feature vector. Another group of studies also applied different feature extraction methods [133, 215, 217, 261, 262, 263, 265, 266, 267, 288, 289, 292]. In these specific cases, no comparison is performed against the original data.

3.4 Conclusion

This review leads to some general discussions which could direct to future avenues for research. As previously mentioned, no open mp-MRI is currently available. This fact leads to an impossibility to fairly compare the different algorithms designed over years. Also, the availability of a full mp-MRI dataset, could lead to the development of algorithms which use all the different modalities currently available. Recalling Table 3.1, it can be noted that a single research work provides a solution using at the same time the 4 different modalities. Also, all the algorithms are focused on one type of scanner only, either 1.5 T and 3 T. A dataset including both these types of imaging could allow development of more generic algorithms.

Analyzing the different stages of the CAD work-flow, it is seen that the current CAD systems do not include all the pre-processing steps. It could be interesting to evaluate the improvement using these pre-processing steps on the final results. Regarding segmentation and registration of the prostate, CAD systems could greatly benefit from specific research in these areas which could lead to a better automation of those systems.

Additionally, no research focus on the problem of imbalanced dataset. While classifying at the voxel-level, the medical dataset are highly imbalanced regarding the frequencies of CaP against healthy samples. Imbalanced data substantially compromises the learning process since most of the standard machine learning algorithms expect balanced class distribution or an equal misclassification cost [96]. Therefore, it seems important to investigate this field of pattern recognition to improve the classification performance while developing CAD systems.

An important point allowing a fair comparison between methods resides in the fact that no common dataset, nor universal evaluation model, nor metric has been defined by the research community allowing such comparison.

3. REVIEW OF CAD SYSTEMS FOR CAP

Chapter 4

Materials

4. MATERIALS

Chapter 5

Normalization/Standardization of T2W-MRI and DCE-MRI Images

CAD systems are usually designed as a sequential process consisting of four stages: pre-processing, segmentation, registration and classification. As a pre-processing image and data normalization is a crucial and important step of the chain in order to design a robust classifier and overcome the inter-patients intensity variations. However little attention has been dedicated to the normalization. In this section, we first propose two methods for normalization of T₂-W-MRI prostate images based on: (i) Rician *a priori* and (ii) square-root slope function (SRSF) representation. Then we proposed a fully automated framework for normalization of DCE-MRI images. In both cases, a comparison with the state-of-the-art methods are provided.

5.1 Normalization of T₂-W-MRI images

This section presents the state-of-the-art method proposed for normalization of T₂-W-MRI prostate images. Our proposed methods (Sect. 5.1.1), the designed experiments and finally the conclusions drawn from the results obtained.

Artan *et al.* [14, 15] and Ozer *et al.* [191, 192] proposed to normalize the T2W-MRI images by computing the standard score (i.e., *z-score*) of the PZ pixels such

5. NORMALIZATION/STANDARDIZATION OF T2W-MRI AND DCE-MRI IMAGES

as:

$$I_s(x) = \frac{I_r(x) - \mu_{PZ}}{\sigma_{PZ}}, \forall x \in PZ, \quad (5.1)$$

where, $I_s(x)$ and $I_r(x)$ are the standardized and the raw signal intensity, respectively, and μ_{PZ} and σ_{PZ} are the mean and standard deviation of the PZ signal intensity. This transformation enforces the image PDF to have a zero mean and a unit standard deviation. However, this normalization is not appropriate if the PDF do not follow a Gaussian distribution as illustrated in Fig. 5.1

Lv *et al.* [160] used the method proposed by Nyul *et al.* [186]. For a given patient, a warping function is inferred by matching some specific landmarks (i.e., median and different percentiles) of the current PDF to the same landmarks learned during a training phase from several patients. The mapping between each landmark is performed using a linear mapping. Viswanath *et al.* [292] used a variant of the previous method by segmenting first the image using region growing with a pre-defined homogeneity criterion and keeping only the largest region to build the PDF. Nevertheless, the warping functions inferred by these methods can suffer from abrupt changes around the landmarks position, leading to a disrupt PDF in the normalized image.

In this section, we evaluate and compare different normalization approaches in the context of T2W-MRI prostate images normalization. Our contribution is threefold: (i) a normalization approach based on a Rician *a priori*; (ii) a normalization approach based on a method used in registration of functional data, without any assumption regarding the PDF of the data; (iii) a novel evaluation metric to asses quantitatively the alignment of the PDFs independently of the assumed distribution. These methods will be compared qualitatively and quantitatively, with both *z-score* normalization and piecewise-linear normalization.

5.1.1 Methodology

5.1.1.1 Normalization using Rician *a priori*

As previosuly stated, proper normalization of the MRI data during pre-processing is a key problem that has been addressed using parametric and non-parametric strategies. We believe that normalizing MRI data using a parametric model based

5.1 Normalization of T₂-W-MRI images

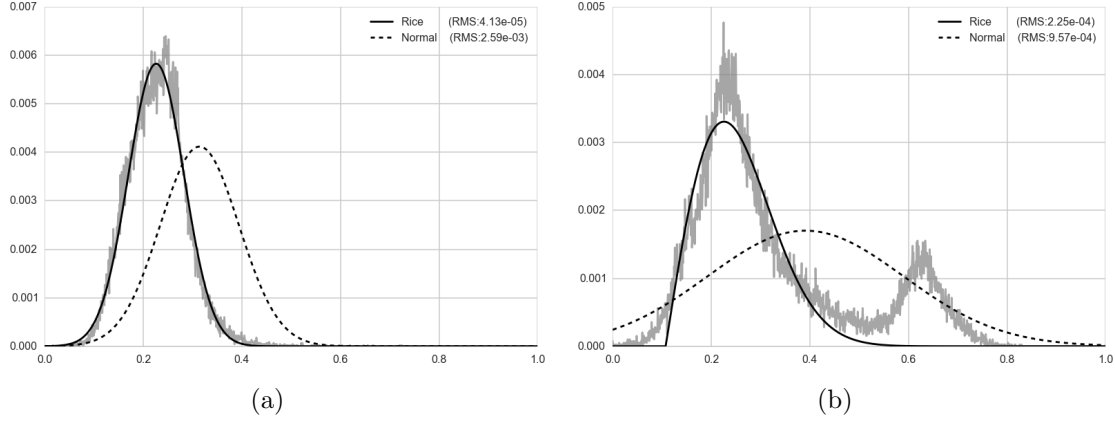


Figure 5.1: Visual evaluation of the goodness of fitting using Rician and Gaussian distribution.

on a Rician distribution would improve the results for the parametric case. Expecting this improvement by changing the data model from the widely used Gaussian distribution to Rician distribution is reasonable. Indeed, Bernstein *et al.* [21] state that MRI data theoretically follows a Rayleigh distribution for a low SNR scenarios while it appears closer to a Gaussian distribution when the SNR increases. Figure 5.1 shows the intensity spectrum for some MRI prostate data as well as the fitted Gaussian and Rician distributions. A qualitative assessment of the underlying distribution is performed by overlying the fitted distribution, while quantitative results of the fitting are given in terms of root mean square (RMS). It can be highlighted that the Rician model better fits the data than the Gaussian model.

The normalization is carried out as: (i) fit a Rician model to each prostate PDF using non-linear least squares minimization; (ii) compute the mean (see Eq. (5.2)) and variance (see Eq. (5.3)) of the Rician model; (iii) normalize the entire data using the *z-score* similarly as in Eq. (5.1).

$$\mu_r = \sigma \sqrt{\frac{\pi}{2}} L_{1/2} \left(-\frac{\nu^2}{2\sigma^2} \right), \quad (5.2)$$

$$\sigma_r = 2\sigma^2 + \nu^2 - \frac{\pi\sigma^2}{2} L_{1/2}^2 \left(\frac{-\nu^2}{2\sigma^2} \right), \quad (5.3)$$

5. NORMALIZATION/STANDARDIZATION OF T2W-MRI AND DCE-MRI IMAGES

where ν and σ are the distance between the reference point and the center of the bivariate distribution and the scale, respectively; $L_{1/2}$ denotes a Laguerre polynomial.

5.1.1.2 Normalization using generative models in functional data analysis

Srivastava *et al.* [248] have proposed a generic method to register functional data, without any assumption regarding the models of different functions. This framework (see Sect. ??) relies on the SRSF representation (see Sect. ??) which transforms the Fisher-Rao metric into the conventional \mathbb{L}^2 metric, and thus allows to define a cost function corresponding to an Euclidean distance between two functions in this new representation.

square-root slope function representation In the proposed registration framework of functional data, two function f_1 and f_2 are registered by composing f_2 with a warping function γ such that:

$$\arg \min_{\gamma \in \Gamma} D_{FR}(f_1, (f_2 \circ \gamma)) , \quad (5.4)$$

where D_{FR} is the Fisher-Rao distance and Γ is the set of all the functions γ .

The SRSF representation is used to transform the functions and register them into this space. The SRSF of a function f is defined as:

$$q(t) = \text{sign}(\dot{f}(t)) \sqrt{|\dot{f}(t)|} , \quad (5.5)$$

where $\dot{f}(t)$ corresponds to the derivative of f .

The major property of the SRSF representation used in the registration framework is the following: the composition of a function f with a warping function γ (i.e., $f \circ \gamma$) is equivalent to Eq. (5.6), using the SRSF representation.

$$\tilde{q}(t) = (q(t) \circ \gamma) \sqrt{\dot{\gamma}} , \quad (5.6)$$

where $\dot{\gamma}$ is the derivative of γ .

Using this property, a cost function (named amplitude or y -distance) is defined to measure the similarity between two functions f_1 and f_2 , expressed as in Eq. (5.7)

$$D_y(f_1, f_2) = \inf_{\gamma \in \Gamma} \|q_1 - (q_2 \circ \gamma)\sqrt{\dot{\gamma}}\| . \quad (5.7)$$

Registration framework The registration framework consists into two steps. First, an initialization in which the Karcher mean μ_f is computed as in Eq. (5.8)

$$\mu_f = \arg \min_{f \in \mathcal{F}} \sum_{i=1}^n D_y(f, f_i)^2 . \quad (5.8)$$

Then, for each function f_i : (i) compute γ_i^* as in Eq. (5.9); (ii) compute \tilde{q}_i as in Eq. (5.6); (iii) update μ_f as in Eq. (5.8) by replacing f_i by \tilde{f}_i , using \tilde{q}_i .

$$\gamma_i^* = \arg \min_{\gamma \in \Gamma} \sum_{i=1}^n D_y(\mu_f, f_i)^2 , \quad (5.9)$$

where n is the total number of functions to be aligned.

This step is iteratively performed based on the gradient of the cost function given in Eq. (5.8). We refer the reader to the work of Srivastava *et al.* [248] for more detailed discussion.

5.1.2 Experiments and results

5.1.2.1 Experiments

This section has repetitive information according to data, it should be checked.

The experiments are conducted on a subset of public multi-parametric MRI prostate publicly available dataset¹ [?]. This dataset was acquired from a cohort of patients with higher-than-normal level of PSA. The acquisition was performed using a 3T whole body MRI scanner (Siemens Magnetom Trio TIM, Erlangen, Germany) using sequences to obtain T₂-W-MRI. Aside of the MRI examinations, these patients also underwent a guided-biopsy. Finally, the dataset was composed of a total of 20 patients of which 18 patients had biopsy proven CaP and 2 patients

¹<http://visor.udg.edu/i2cvb/>

were “healthy” with negative biopsies. In this study, our subset consists of 17 patients with CaP. The prostate organ as well as the prostate zones (i.e., PZ, CG) and CaP were manually segmented by an experienced radiologist.

The different normalization methods are implemented in Python and publicly available in GitHub¹. The normalization based on SRSF uses the implementation² of Tucker *et al.* [276].

The model fitting for the Gaussian and Rician normalization is performed as a non-linear least squares problem, using Levenberg-Marquardt optimization. The piecewise-linear normalization is performed using the following set of percentiles $s \in \{0, 5, 25, 50, 75, 95, 100\}$ as landmarks. In the SRSF-based normalization, the PDFs are smoothed using spline-based denoising method.

5.1.2.2 Results

Qualitative Figure 5.2 depicts the alignment of the different PDFs using the different methods implemented. All the methods seem to address the problem of the PDF alignment of the full prostate data. However, the Rician normalization seems to outperform the other methods when focusing solely on the CaP data. The PDF computed in this specific area is more skewed from its original shape in the case of the piecewise-linear normalization than with the three other normalization strategies. The SRSF normalization gets unstable due to the warping function γ found which is in practise non-smooth.

Quantitative A spectral evaluation is performed by decomposing the set of normalized PDFs using PCA under the assumption that they are linearly dependent. Intuitively, the eigenvalues of the PCA decomposition are correlated with the alignment of the different PDFs. Thus, in the case of a perfect alignment of the PDFs, the first eigenvalue is much greater than the remaining since that the first eigenvector encodes all the information. In the contrary, in the case of a misalignment of the PDFs, more eigenvectors are needed to encode the information synonymous with larger eigenvalues. Thus, we propose to use the cumulative sum of the normalized eigenvalues as well as the AUC, as depicted in Fig. 5.3. Rician

¹<https://github.com/glemaitre/protoclass>

²<https://bitbucket.org/tetonedge/fdasrsf>

5.1 Normalization of T₂-W-MRI images

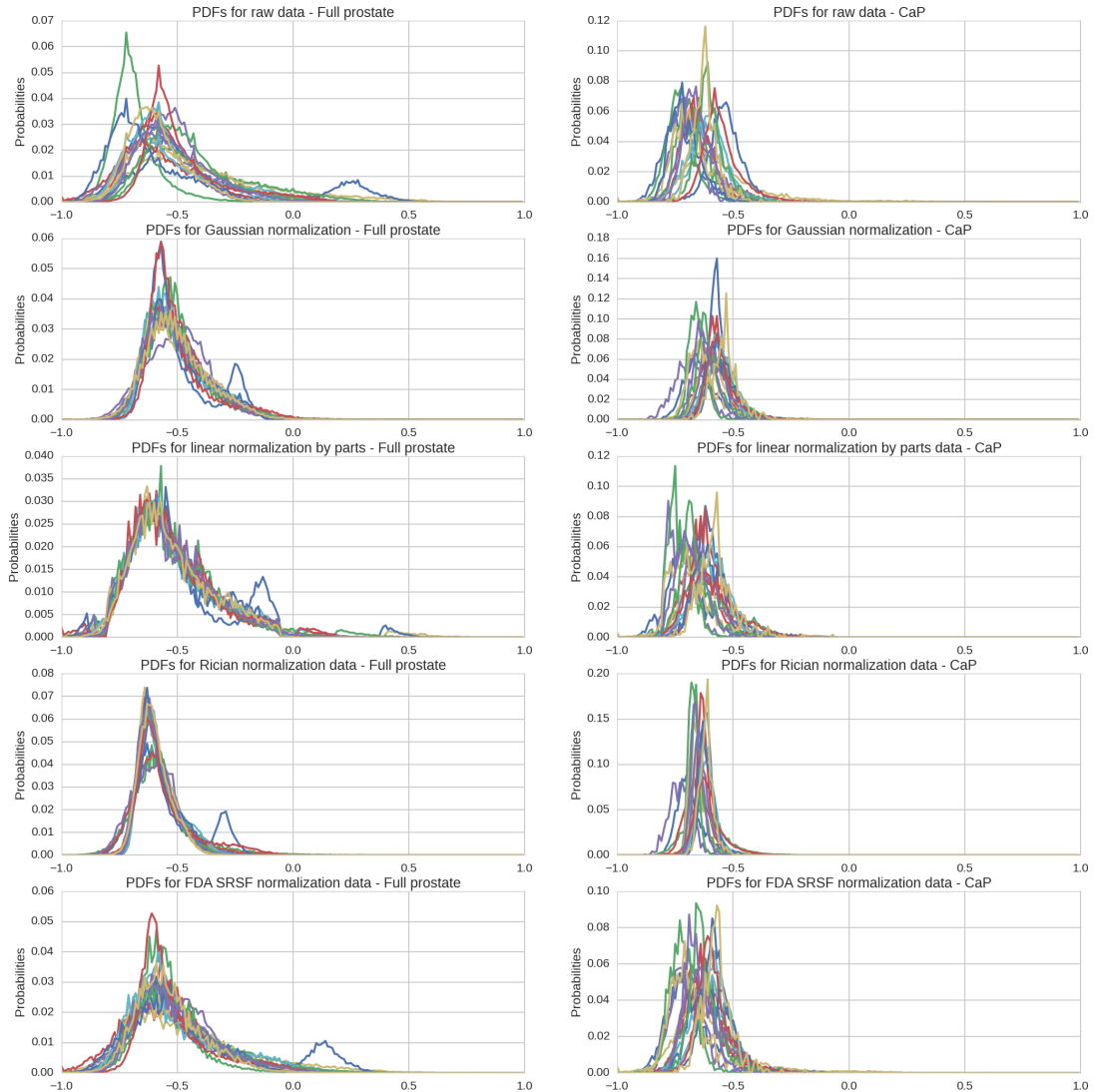
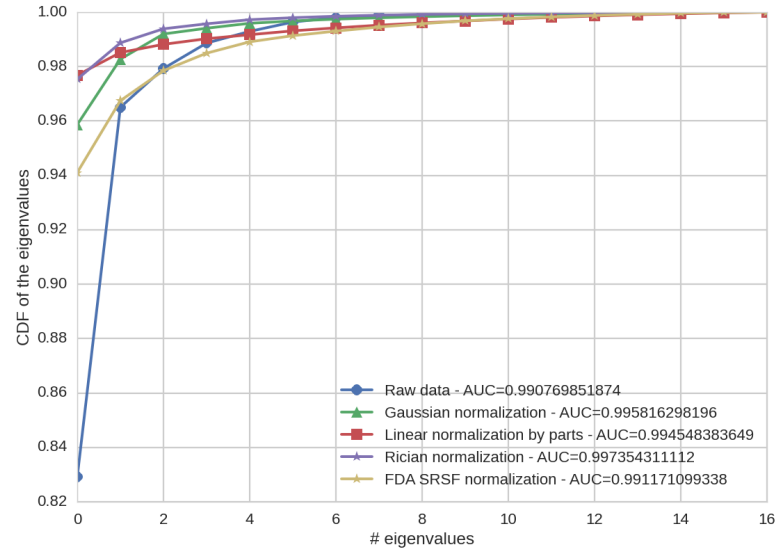
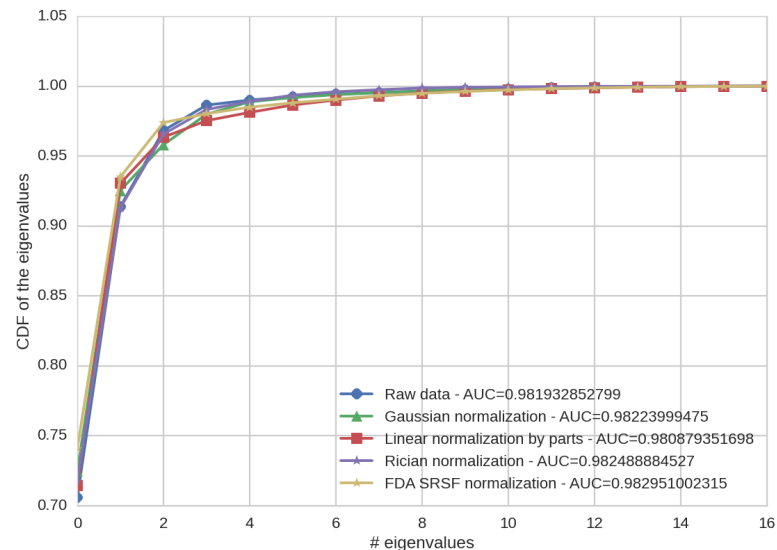


Figure 5.2: Qualitative evaluation by visual inspection of the alignment of the PDFs for the full prostate and the CaP.

5. NORMALIZATION/STANDARDIZATION OF T2W-MRI AND DCE-MRI IMAGES



(a)



(b)

Figure 5.3: Spectral evaluation using PCA decomposition: (a) evaluation considering the full prostate, (b) evaluation considering only the CaP.

normalization outperforms the other methods with an AUC of 0.9974 and 0.9824 considering the full prostate and CaP, respectively.

5.1.3 Discussion and conclusion

In this section, we propose to normalize the T₂-W-MRI prostate images using two new strategies: (i) based on a Rician *a priori* and (ii) based on a SRSF representation which do not make any assumption regarding the PDF of the data. An extensive comparison was conducted showing that the Rician normalization outperforms the Gaussian, SRSF-based, and piecewise-linear normalization for T₂-W-MRI prostate images normalization.

As avenues for future research, the contribution of the Rician normalization must be evaluated in a classification framework. Furthermore, normalized T₂-W-MRI can be included with other modalities in order to perform classification using multi-parametric MRI data.

5.2 Normalization of DCE-MRI images

In DCE-MRI, a contrast media is injected intravenously and a set of images is acquired over time. Consequently, each voxel in an image corresponds to a dynamic signal which is related to both contrast agent concentration and the vascular properties of the tissue. Therefore, changes of the enhanced signal allows to discriminate healthy from CaP tissues. In fact, these properties are automatically extracted using quantitative or semi-quantitative approaches [137].

Quantitative approaches uses pharmacokinetic modelling based on a bicompartiment model, namely Brix [29] and Tofts [270] models. The parameters of the Brix model are inferred assuming a linear relationship between the media concentration and the MRI signal intensity. This assumption has shown, however, to lead to inaccurately estimate the pharmacokinetic parameters [99]. In the contrary, Tofts model requires a conversion from MRI signal intensity to concentration, which becomes a non-linear relationship using specific equation of MRI sequences (e.g., FLASH sequence). Tofts modelling suffers, however, from a higher complexity [87]. Indeed, the conversion using the non-linear approach requires to acquire

5. NORMALIZATION/STANDARDIZATION OF T2W-MRI AND DCE-MRI IMAGES

a T_1 map which is not always possible during clinical examination. Additionally, the parameter calculation requires the AIF which is challenging to measure and can also lead to an inaccurate estimation.

Semi-quantitative approaches are rather mathematical than pharmacokinetic modelling since no pharmacokinetic assumption regarding the relation between the MRI signal and the contrast agent are made [87, 109]. These methods offer the advantages to not require any knowledge about the MRI sequence nor any conversion from signal intensity to concentration. However, they present some limitations: the heuristic approach proposed by Huisman *et al.* [109] requires an initial estimate of the noise standard deviation of the signal as well as some manual tuning.

Nevertheless, all presented methods suffer from two major drawbacks: (i) inter-patient variability and (ii) loss of information. The inter-patient variability is mainly due to the acquisition process and consequently leads to generalization issue while applying a machine learning algorithm. All previous methods extract few discriminative parameters to describe the DCE-MRI signal which might lead to a loss of information.

In this section, we propose a fully automatic normalization method for DCE-MRI that reduces the inter-patient variability of the data. The benefit and simplicity of our approach will be shown by classifying the whole normalized DCE-MRI signal and comparing with the state-of-the-art quantitative and semi-quantitative methods. Additionally, we will show that using this normalization approach in conjunction with the quantitative methods improves the classification performance of most of the models. We also propose a new clustering-based method to segment enhanced signals from the arteries, later used to estimate an AIF as well as an alternative approach to estimate the parameters of the semi-quantitative model proposed by [109].

This section is organized as follows: First Sect. 5.2.1.1 details our normalization strategy for DCE-MRI data. Quantitative and semi-quantitative methods are summarized in Sect. 5.2.1.2 with insights about their implementations. Finally experiments and results to answer the previous stated challenges are reported in Sect. 5.2.2 while discussed in Sect. 5.2.3, followed by a concluding section.

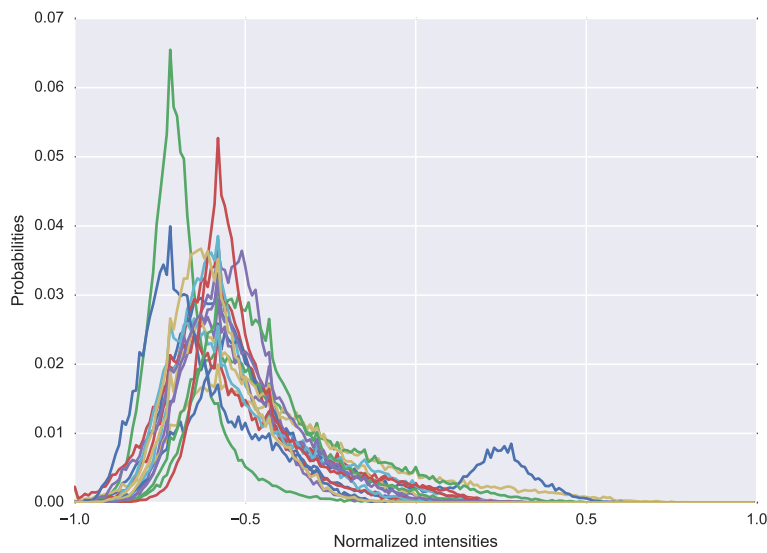


Figure 5.4: Illustration of the inter-patient variations in 17 different patients, using the PDF representation.

5.2.1 Methodology

5.2.1.1 Normalization of DCE-MRI images

In this section, we propose a method to normalize DCE-MRI prostate data to reduce inter-patient variations, although it can be applied to any DCE-MRI sequences. In T_2 -W-MRI, these variations are characterized by a shift and a scaling of the intensities as illustrated by the intensity PDF in Fig. 5.4. Therefore, these variations can be corrected using a z -score approach—i.e., normalizing the data by subtracting the mean and dividing by the standard deviation—assuming that the data follow a specific distribution [138].

In DCE-MRI, the intensity PDF of prostate gland does not follow a unique type of distribution such as Rician or Gaussian distribution, as shown in Fig. 5.5(a). Indeed, the inter-patient variations are more complex due to the temporal acquisition. A better representation to observe these variations is to represent the intensity PDF of the prostate gland over time—requiring to segment the prostate—using a heatmap representation as shown in Fig. 5.5(a). Analyzing this heatmap representation across patients (see Fig. 5.5(c)), the following variations are highlighted: (i) intensity offsets Δ_i of the PDF peak, (ii) a time offset Δ_t depending

5. NORMALIZATION/STANDARDIZATION OF T2W-MRI AND DCE-MRI IMAGES

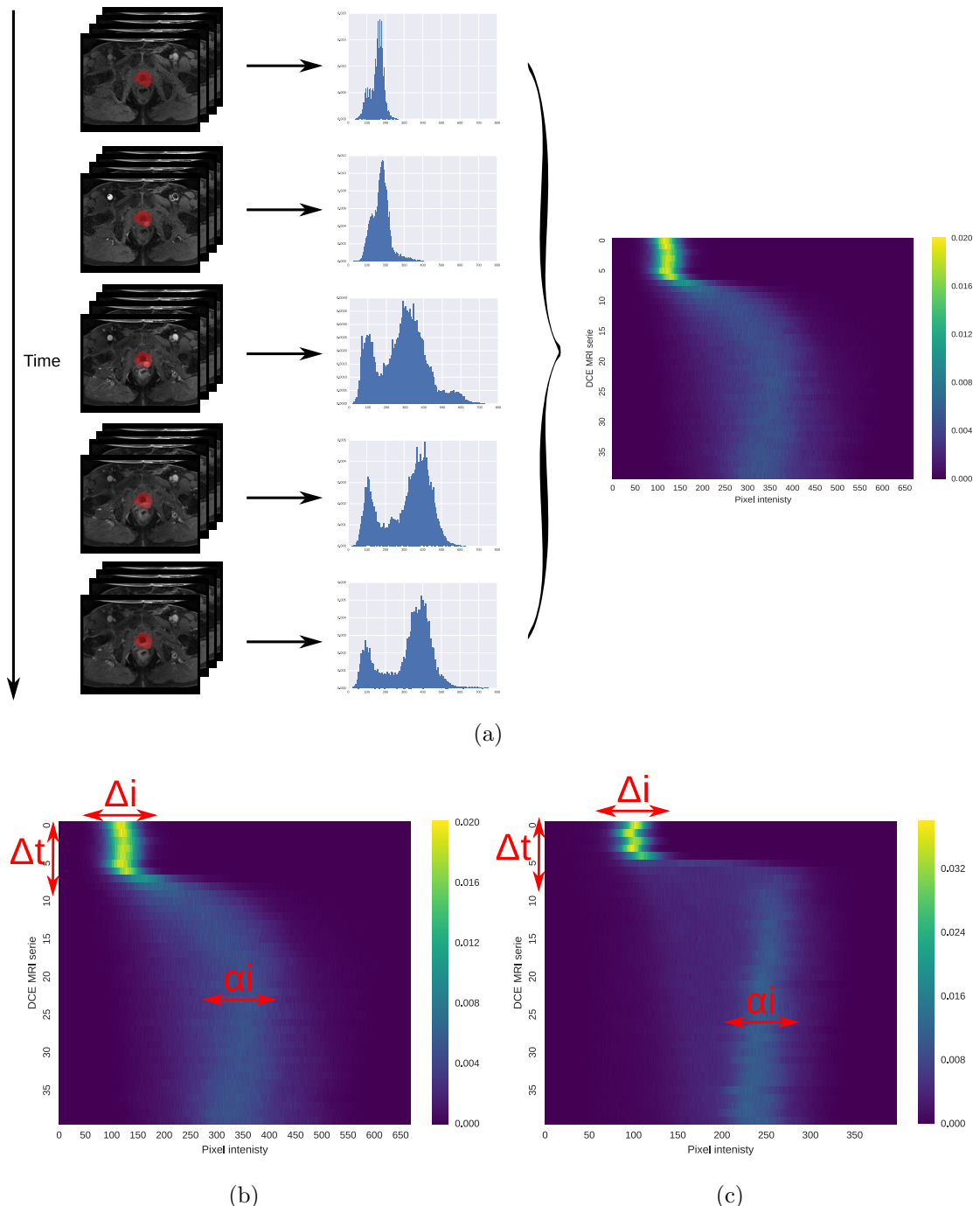


Figure 5.5: (a) Illustration of the heatmap representation: all PDFs of the prostate gland are concatenated together to build an heatmap; (b)-(c) Illustration of inter-patient variations (i.e., Δ_i , Δ_t , and α_i) PDF over time of two patients in a DCE-MRI.

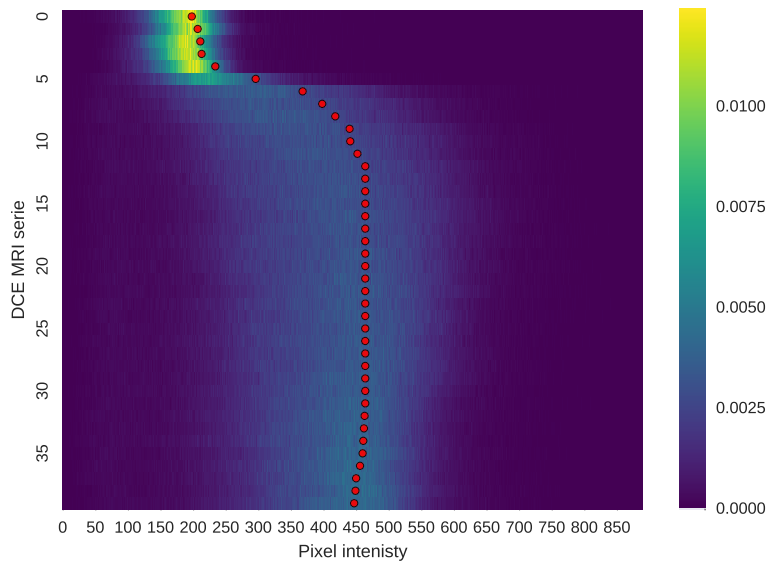


Figure 5.6: Illustration of the estimator found using the shortest-path through the graph.

of the contrast agent arrival, and (iii) a change of scale α_i related to the signal enhancement. Therefore, our normalization method should attenuate all these variations and be performed globally across the different time sequences rather than for each independent sequence.

Graph-based intensity offsets correction Before to standardize each sequence, the first step of the normalization is to cancel the intensity specific at each patient, occurring due to the media injection. As previously mentioned, the intensity PDF does not always follow either a Rician or a Gaussian distribution over time, in DCE-MRI. Therefore, the mean of these distributions cannot be used as a potential estimate for these offsets. Additionally, these offsets should be characterized by a smooth transition between series over time. Thus, this problem is solved using the graph-theory: considering the intensity PDF over time as shown in Fig. 5.5(a), the offsets correspond to the boundary splitting the heatmap in two partitions such that they are as close as possible to the peak of the intensity PDF (see Fig. 5.6 for an illustration). Given the heatmap, a directed weighted graph $\mathcal{G} = (\mathcal{V}, \mathcal{E})$ is built by taking each bar— i.e., the probability for a given time and

5. NORMALIZATION/STANDARDIZATION OF T2W-MRI AND DCE-MRI IMAGES

pixel intensity—of the heatmap as a node and connecting each pair of bars by an edge. The edge weight w_{ij} between two nodes i and j corresponding to two pixels at position (x_i, y_i) and (x_j, y_j) , respectively, is defined as in Eq. (5.10):

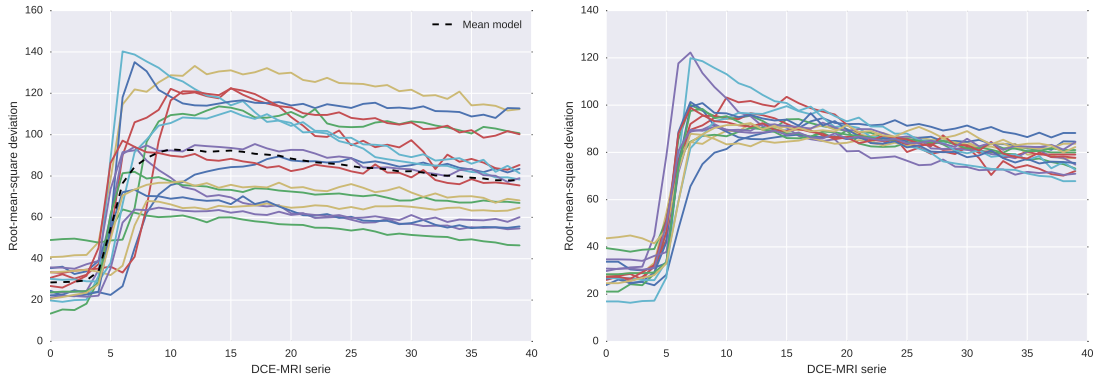
$$w_{ij} = \begin{cases} \alpha \exp\left(1 - \frac{H(i)}{\max(H)}\right) & \text{if } x_j = x_i + 1 \text{ and } y_j = y_i, \\ (1 - \alpha) \exp\left(1 - \frac{H(i)}{\max(H)}\right) & \text{if } x_j = x_i \text{ and } y_j = y_i + 1, \\ 0 & \text{otherwise,} \end{cases} \quad (5.10)$$

where H is the heatmap, α is a smoothing parameter controlling the partitioning.

Therefore, these offsets related to Δ_i are estimated by finding the shortest-path to cross the graph using Dijkstra's algorithm. The entry and exiting nodes are set to be the bin with the maximum probability for the first DCE-MRI serie and the bin corresponding to the median value for the last DCE-MRI serie, respectively. To ensure a robust estimation of these offsets, the process of finding the shortest-path is iteratively repeated by shifting the data and updating the heatmap as well as the graph \mathcal{G} . The procedure is stopped once the offset found does not change. In general, this process is not repeated more than 3 iterations. The parameter α is set to 0.9, empirically. Figure 5.6 illustrates the final estimation of the offsets Δ_i (i.e., red landmark) found for each DCE-MRI serie. Therefore, each intensity offset is subtracted for each DCE-MRI.

Time offset and data dispersion correction The next variations to correct are the time offset Δ_t and the data dispersion σ_i . By computing the root-mean-square deviation (RMSD) of the intensities for each DCE-MRI serie, one can observe these two variations as shown in Fig. 5.7(a). Therefore, to correct these variations, we propose to register each patient RMSD to a mean model which corresponds to the mean of all patients RMSD. The parametric model to perform the registration is formulated as in Eq. (5.11):

$$T(\alpha, \tau, f(t)) = \alpha f(t - \tau), \quad (5.11)$$



(a) RMSD computed for each patient of our dataset.
(b) RMSD after alignment using the curve parametric model.

Figure 5.7: Illustration of the correction of the time offset and the data dispersion.

where α and τ are the two parameters handling the time offset Δ_i and global scale σ_i , respectively, $f(\cdot)$ is the RMSD function define as:

$$f(t) = \sqrt{\left(\frac{\sum_{n=1}^N x(t)_n^2}{N} \right)}, \quad (5.12)$$

where $x(t)_n$ is the shifted intensity of a sample from a specific DCE-MRI serie at time t from a total number of N samples.

Therefore the registration problem is equivalent to:

$$\arg \min_{\alpha, \tau} = \sum_{t=1}^N [T(\alpha, \tau, f(t)) - \mu(t)]^2, \quad (5.13)$$

where $\mu(\cdot)$ is the mean model, N is the number of DCE-MRI serie.

Illustration of the correction applied to each RMSD patient is shown in Fig. 5.7(b). Once all these parameters have been inferred, the data are shifted as well as scaled.

The resulting normalized data can be used into two fashions: (i) each normalized signal can be used as a whole to determine whether the corresponding voxel is healthy or cancerous or (ii) the normalized data can be fitted using a quantitative method, as presented in the next section.

5. NORMALIZATION/STANDARDIZATION OF T2W-MRI AND DCE-MRI IMAGES

5.2.1.2 Quantification of DCE-MRI

The quantitative approaches for detection of DCE-based features was briefly discussed in Sect. 3.2.2.2. In this section, we present in details the different methods which have been used for the quantification of DCE-MRI for CaP detection [137] and which will be used for comparison in this work. Furthermore, we would like to emphasize the following additional contributions for this section: (i) a novel automatic AIF estimation algorithm based on clustering and (ii) a simplified semi-quantitative method using constrained optimization.

Brix and Hoffmann models In the Brix model [29], the MRI signal intensity is assumed to be proportional to the media concentration. Therefore, the model is expressed as in Eq. (5.14) (see also Eq. (3.31)):

$$s_n(t) = 1 + A \left[\frac{\exp(k_{el}t') - 1}{k_{ep}(k_{ep} - k_{el})} \exp(-k_{el}t) - \frac{\exp(k_{ep}t') - 1}{k_{el}(k_{ep} - k_{el})} \exp(-k_{ep}t) \right], \quad (5.14)$$

with

$$s_n(t) = \frac{s(t)}{S_0}, \quad (5.15)$$

where $s(t)$ and S_0 are the MRI signal intensity at time t and the average pre-contrast MRI signal intensity, respectively; A , k_{el} , and k_{ep} are the constant proportional to the transfer constant, the diffusion rate constant, and the rate constant, respectively. Additionally, t' is set such that $0 \leq t \leq \tau$, $t' = t$ and afterwards while $t > \tau$, $t' = \tau$.

Hoffmann *et al.* [103] proposed a similar model as expressed in Eq. (5.16), which derive from the Brix model:

$$s_n(t) = 1 + \frac{A}{\tau} \left[\frac{k_{ep}(\exp(k_{el}t') - 1)}{k_{el}(k_{ep} - k_{el})} \exp(-k_{el}t) - \frac{\exp(k_{ep}t') - 1}{(k_{ep} - k_{el})} \exp(-k_{ep}t) \right], \quad (5.16)$$

in which the constant A is redefined by isolating the parameter τ .

The parameters A , k_{el} , and k_{ep} are estimated by fitting the model using non-linear least-squares optimization solved with Levenberg-Marcquardt.

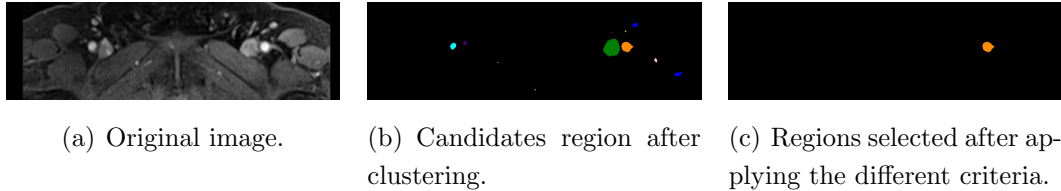


Figure 5.8: Illustration of the segmentation of the area used to determine the AIF.

Tofts model The extended Tofts model is formulated as in Eq. (5.17)(see also Eq. (3.32)):

$$C_t(t) = K_{trans}C_p(t) * \exp(-k_{ep}t) + v_pC_p(t), \quad (5.17)$$

where $*$ is the convolution operator; $C_t(t)$ and $C_p(t)$ are the concentrations of contrast agent in the tissue and in the plasma, respectively; K_{trans} , k_{ep} , and v_p are the volume transfer constant, the diffusion rate constant, and the plasma volume fraction, respectively.

Therefore, Tofts model requires to: (i) detect candidate voxels from the femoral or iliac arteries and estimate a patient-based AIF signal, (ii) convert the MRI signal intensity (i.e., AIF and dynamic signal) to a concentration, and (iii) in the case of a population-based AIF, estimate an AIF signal.

Segmentation of artery voxels and patient-based AIF estimation The AIF signal from DCE-MRI can be manually estimated by selecting the most-enhanced voxels from the femoral or iliac arteries [172]. Few methods have been proposed to address the automated extraction of AIF signal. [41] filtered successively the possible candidates to be considered as AIF such that [41]: (i) dynamic signals with small peak and voxels with a small wash-in are rejected by thresholding, (ii) a blob detector is used and large enough regions are kept, and (iii) circular and cylindricality criteria are used to reject the false positives. Zhu *et al.* [306] proposed an iterative method selecting voxels which best fit a gamma variate function [306]. However, it requires to compute first and second derivatives as well as maximum curvature points. Shanbhag *et al.* [237] proposed a 4-steps algorithm [68, 237]: (i) remove

5. NORMALIZATION/STANDARDIZATION OF T2W-MRI AND DCE-MRI IMAGES

slices with artefacts and find the best slices based on intrinsic anatomic landmarks and enhancement characteristics, (ii) find the voxel candidates using the maximum enhanced voxels and a multi-label maximum entropy based thresholding algorithm, (iii) exclude region next to the endorectal coil, and (iv) select the best 5 candidates which meet enhancement characteristics and that are correlated.

All the above methods are rather complex and thus we propose a simpler method which is based on the following reasonable assumptions: (i) all possible AIF signal candidates should have a similar shape, (ii) a high enhancement, and (iii) the arteries should be almost round and within a size range. Therefore, each slice is clustered into regions using K-means clustering with $k = 6$. The cluster made of the most enhanced signals is selected since it contains the artery signals. In this regards, the selection criteria corresponds to the 90th percentile of the maximum DCE-MRI signal. Finally, regions with an eccentricity smaller than 0.5 and an area in the range of [100, 400] voxels are kept. Additionally, to remove voxels contaminated by partial volume effect, only the 10% most enhanced voxels of the possible candidates are kept as proposed by [231] and the average signal is computed. A summary of the different segmentation steps is presented in Fig. 5.8.

Conversion of MRI signal intensity to concentration To estimate the free parameters of the Tofts model (see Eq. (5.17)), the concentration $C_t(t)$ and $C_p(t)$ need to be computed from the MRI signal intensity and the AIF signal, respectively. This conversion is based on the equation of the FLASH sequence—see ?? for details—and is formulated as in Eq. (5.18):

$$c(t) = \frac{1}{TR \cdot r_1} \ln \left(\frac{1 - \cos \alpha \cdot S^* \frac{s(t)}{S_0}}{1 - S^* \frac{s(t)}{S_0}} \right) - \frac{R_{10}}{r_1}, \quad (5.18)$$

with,

$$S^* = \frac{1 - \exp(-TR \cdot R_{10})}{1 - \cos \alpha \cdot \exp(-TR \cdot R_{10})}, \quad (5.19)$$

where $s(t)$ is the MRI signal, S_0 is the MRI signal prior to the injection of the contrast media, α is the flip angle, TR is the repetition time (TR),

R_{10} is the pre-contrast tissue relaxation time also equal to $\frac{1}{T_{10}}$, and r_1 is the relaxitativity coefficient of the contrast agent.

T_{10} can be estimated from the acquisition of a T_1 map. However, this modality is not part of the clinical trial in this research and the value of T_{10} is fixed to 1600 ms for both blood and prostate, in accordance with the values found in the literature [68? ?].

Estimation of population-based AIF While estimating the pharmacokinetic parameters from Tofts model, the AIF concentration $C_p(t)$ can be computed either from the patient or a population. We presented in the two previous sections the algorithms which allows to estimate the patient-based AIF concentration. To compare with the previous approach, we also computed a population-based AIF which will be also used later to compare the performance of both approaches. In that regard, the population-based AIF was estimated as in [172] by fitting the average patient-based AIFs to the model of [197] which is formulated as in Eq. (5.20):

$$C_p(t) = \sum_{n=1}^2 \frac{A_n}{\sigma_n \sqrt{2\pi}} \exp\left(\frac{-(t - T_n)^2}{2\sigma_n^2}\right) + \frac{\alpha \exp(-\beta t)}{1 + \exp -s(t - \tau)}, \quad (5.20)$$

where A_n , T_n , and σ_n are the scaling constants, centers, and widths of the n^{th} Gaussian, α and β are the amplitude and decay constant of the exponential; and s and τ are the width and center of the sigmoid function, respectively.

The parameters are estimated by fitting the model using a constrained non-linear least-squares optimization, solved with the Trust Region Reflective algorithm [246] and bounding the parameters to be positive.

PUN model Gliozzi *et al.* [87] showed that PUN approach can be used for DCE-MRI analysis [87]. The model has been successfully used in a CAD system proposed by [81]. This model can be expressed as in Eq. (5.21) (see also Eq. (3.34)):

$$s_n(t) = \exp \left[rt + \frac{1}{\beta} (a_0 - r) (\exp(\beta t) - 1) \right], \quad (5.21)$$

5. NORMALIZATION/STANDARDIZATION OF T2W-MRI AND DCE-MRI IMAGES

with

$$s_n(t) = \frac{s(t) - S_0}{S_0}, \quad (5.22)$$

where $s(t)$ and S_0 are the MRI signal intensity at time t and the average pre-contrast MRI signal intensity, respectively; r , a_0 , and β are the free parameters of the model.

The parameters are estimated by fitting the model using non-linear least-squares optimization solved with Levenberg-Marcquardt.

Semi-quantitative analysis The semi-quantitative analysis of the DCE-MRI is equivalent to extracting curve characteristics directly from the signal without a strict theoretical pharmacokinetic meaning (see Table. 3.8). In this work, we use the model presented by [109] which formulated the MRI signal as in Eq. (5.23):

$$s(t) = \begin{cases} S_0 & 0 \leq t \leq t_0 \\ S_M - (S_M - S_0) \exp\left(\frac{-(t-t_0)}{\tau}\right) & t_0 < t \leq t_0 + 2\tau \\ S_M - (S_M - S_0) \exp\left(\frac{-(t-t_0)}{\tau}\right) + w(t - t_0 + 2\tau) & t > t_0 + 2\tau \end{cases} \quad (5.23)$$

where $s(t)$ is the MRI signal intensity, S_0 is the pre-contrast signal intensity, t_0 is the time corresponding to the start of enhancement, S_M and τ is the maximum of the signal and the exponential time constant, and w is the slope of the linear part.

Huisman *et al.* [109] argue that curve fitting via least-squares minimization using Nelder-Mead algorithm leads to inaccurate estimation of the free parameters: mainly the issue come from an incorrect estimation of the start of enhancement t_0 leading to incorrect estimation of the other parameters. Therefore, they propose to: (i) estimate robustly t_0 , (ii) estimate S_0 by averaging the samples between 0 and t_0 (ii) estimate w depending if the slope is significant or not, (iii) estimate S_M which should be the point at the intersection of the most probable slope line and the plateau.

Instead of these successive estimations, we propose a unified optimization in which t_0 is fixed since that this is a key parameter. Therefore, t_0 is robustly estimated from the AIF signal since that this is the most enhanced signal in which

the start of enhancement is easily identifiable. The AIF signal is computed as in Section ???. t_0 is estimated by finding the maximum of the first derivative of the AIF signal, always occurring at the beginning of the signal. Then, the function in Eq. (5.23) is fitted using non-linear least squares with the Trust Region Reflective algorithm [246]. Furthermore, the parameters τ and S_M are bounded during the optimization to ensure robust estimations. τ is bounded between t_0 and t_f which is the time of the last sample while S_M is bounded between S_0 and $\max(s(t))$.

From Eq. (5.23), the following features are extracted: (i) the wash-in corresponding to the slope between t_0 and $t_0 + 2\tau$, (ii) the wash-out corresponding to the parameter w , (iii) the area under the curve between t_0 and the end of the signal, (iv) the exponential time constant τ , and (v) the relative enhancement $S_M - S_0$.

5.2.2 Experiment and results

>Data, check with the material chapter

The multi-parametric MRI data are acquired from a cohort of patients with higher-than-normal level of PSA. The acquisition is performed using a 3T whole body MRI scanner (Siemens Magnetom Trio TIM, Erlangen, Germany) using sequences to obtain T₂-W-MRI, DCE-MRI and DW-MRI. Aside of the MRI examination, these patients also have undergone a guided-biopsy. The dataset is composed of a total of 20 patients of which 18 patients have biopsy proven CaP and 2 patients are “healthy” with negative biopsies. Therefore, 13 patients have a CaP in the PZ, 3 patients have CaP in the CG, 2 patients have invasive CaP in both PZ and CG and finally 2 patients are considered as “healthy”. An experienced radiologist has segmented the prostate organ — on T₂-W-MRI and DCE-MRI — as well as the prostate zones (i.e., PZ and CG) and CaP on the T₂-W-MRI.

A 3 mm slice fat-suppressed T₂-W fast spin-echo sequence (TR/TE/echo train length (ETL): 3400 ms/85 ms/13) is used to acquire images in sagittal and oblique coronal planes, the latter planes being orientated perpendicular or parallel to the prostate PZ rectal wall axis. Three-dimensional T₂-W fast spin-echo (TR/TE/ETL: 3600 ms/143 ms/109, slice thickness: 1.25 mm) images are then acquired in an

5. NORMALIZATION/STANDARDIZATION OF T2W-MRI AND DCE-MRI IMAGES

Table 5.1: Coefficient of determination R^2 (i.e., μ ($\pm\sigma$)), while fitting data with the different quantification models.

Data type	Brix	Hoffmann	Tofts population AIF	Tofts patient AIF	PUN	Semi-quantitative
Un-normalized	0.85 (± 0.11)	0.81 (± 0.17)	0.84 (± 0.14)	0.88 (± 0.12)	0.27 (± 0.18)	0.64 (± 0.24)
Normalized	0.92 (± 0.05)	0.72 (± 0.32)	0.92 (± 0.06)	0.90 (± 0.10)	0.28 (± 0.20)	0.75 (± 0.20)

oblique axial plane. The nominal matrix and field of view (FOV) of the 3D T₂-W fast spin-echo images are 320 × 256 and 280 × 240 mm², respectively, thereby affording sub-millimetric pixel resolution within the imaging plane.

DCE-MRI is performed using a fat suppressed 3D T₁ VIBE sequence (TR/TE/Flip angle: 3.25 ms/1.12 ms/10°; Matrix: 256 × 192; FOV: 280 × 210 (with 75% rectangular FOV); slab of 16 partitions of 3.5 mm thickness; temporal resolution: 6 s/slab over approximately 5 min). A power injector (Medrad, Indianola, USA) is used to provide a bolus injection of Gd-DTPA (Dotarem, Guerbet, Roissy, France) at a dose of 0.2 ml Gd-DTPA/kg of body weight.

These DCE-MRI sequences are resampled using the spatial information of the T₂-W-MRI and missing data are interpolated using a linear interpolation. The volumes of the DCE-MRI dynamic are rigidly registered, to remove any patient motion during the acquisition. Furthermore, a non-rigid registration is performed between the T₂-W-MRI and DCE-MRI in order to propagate the prostate zones and CaP ground-truths. The resampling is implemented in C++ using the Insight Segmentation and Registration Toolkit [111].

The implementation of the registration (C++), normalization (Python), and classification pipeline (Python) are publicly available on GitHub¹ [136]. The data used for this work are also publicly available² [139].

5.2.2.1 Goodness of model fitting

Parameter estimation of the quantification methods are related to fit a specific model to the DCE-MRI data. Therefore, this section report the goodness of fitting

¹<https://github.com/I2Cvb/lemaître-2016-nov/tree/master>

²<https://zenodo.org/record/61163>

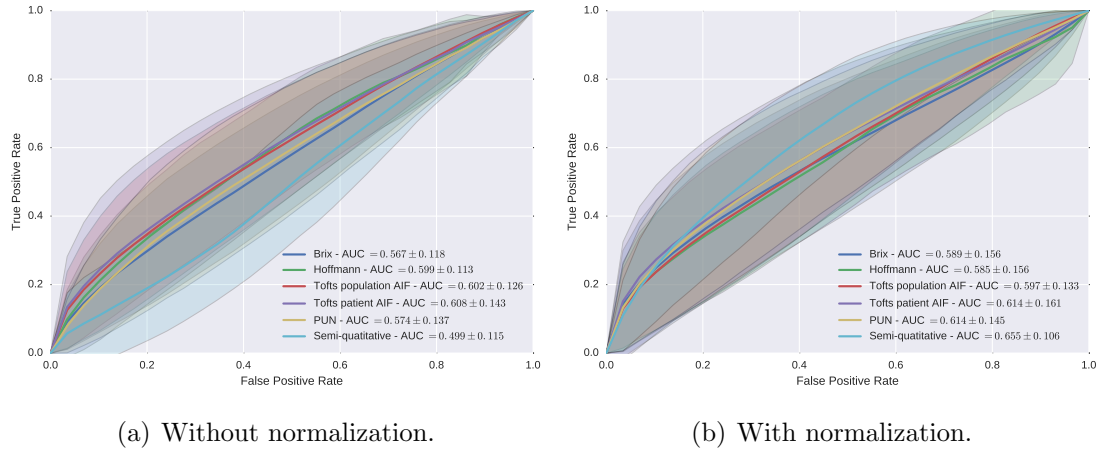


Figure 5.9: ROC analysis using a RF classifier with and without normalization DCE-MRI data for different pharmacokinetic models.

by computing the coefficient of determination R^2 such as in Eq. (5.24)

$$R^2 = 1 - \frac{\sum_{t=1}^T (s_t - \hat{s}_t)^2}{\sum_{t=1}^T (s_t - \bar{s})^2}, \quad (5.24)$$

where s_t and \hat{s}_t are the signal to be fitted and the estimated signal at time t , respectively; \bar{s} is the average signal to be fitted.

Mean and standard-deviation of the coefficient of determination R^2 is reported in Table 5.1 for each quantification model. Brix, Hoffmann, and Tofts models are fitted with a coefficient R^2 superior to 0.80. Additionally, the proposed PUN model does not seem to fit well the data. Data normalization improves the coefficient R^2 for all the methods apart of the Hoffmann model. The large standard deviation for this model might imply that there are some cases where the fitting fails.

5.2.2.2 Detection of CaP using pharmacokinetic parameters

To study the potential benefit of our normalization, CaP are detected at a voxel level using pharmacokinetic parameters estimated from un-normalized and normalized DCE-MRI data. Each individual pharmacokinetic parameter is classified to evaluate their individual discriminative power to detect CaP. Therefore, a RF classifier is used in conjunction with a leave-one-patient-out cross-validation (LOPO

5. NORMALIZATION/STANDARDIZATION OF T2W-MRI AND DCE-MRI IMAGES

Table 5.2: AUC (i.e., $\mu (\pm\sigma)$) for each individual pharmacokinetic parameter using a RF classifier.

Features	Un-normalized data	Normalized data
Brix model		
A	0.540 (± 0.069)	0.555 (± 0.080)
k_{el}	0.549 (± 0.062)	0.577 (± 0.093)
k_{ep}	0.506 (± 0.032)	0.497 (± 0.019)
Hoffmann model		
A	0.516 (± 0.020)	0.508 (± 0.031)
k_{el}	0.545 (± 0.066)	0.529 (± 0.065)
k_{ep}	0.550 (± 0.063)	0.545 (± 0.060)
Tofts model with population AIF		
K_{trans}	0.556 (± 0.086)	0.565 (± 0.097)
k_{ep}	0.506 (± 0.026)	0.528 (± 0.038)
v_p	0.533 (± 0.064)	0.548 (± 0.082)
Tofts model with patient AIF		
K_{trans}	0.563 (± 0.077)	0.548 (± 0.060)
k_{ep}	0.492 (± 0.025)	0.491 (± 0.020)
v_p	0.530 (± 0.069)	0.495 (± 0.033)
PUN model		
a_0	0.521 (± 0.040)	0.530 (± 0.045)
r	0.550 (± 0.085)	0.573 (± 0.097)
β	0.531 (± 0.051)	0.549 (± 0.068)
Semi-quantitative analysis		
wash-in	0.587 (± 0.107)	0.533 (± 0.032)
wash-out	0.516 (± 0.037)	0.486 (± 0.035)
IAUC	0.506 (± 0.048)	0.513 (± 0.032)
τ	0.565 (± 0.104)	0.537 (± 0.089)
$S_M - S_0$	0.560 (± 0.083)	0.532 (± 0.029)

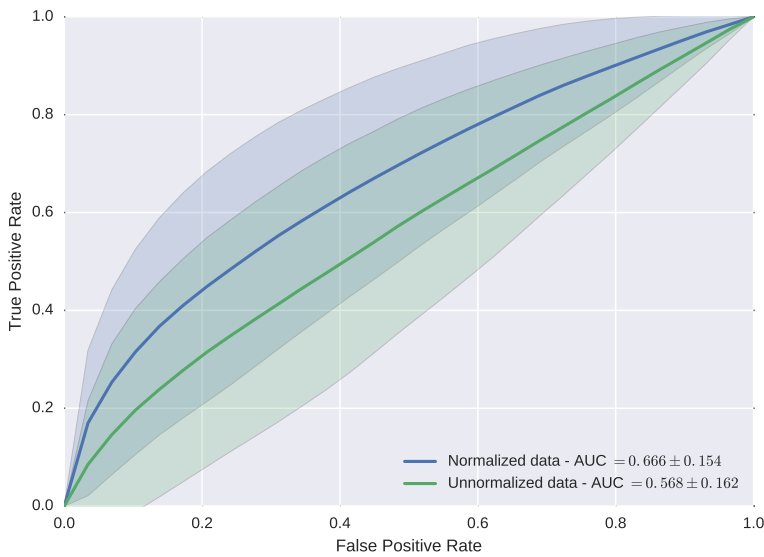


Figure 5.10: ROC analysis using the entire DCE-MRI signal with and without normalization in conjunction with a RF classifier.

CV). The use of RF is motivated since that it leads to the best performance in the state-of-the-art methods [137, 151]. Results are summarized in Table 5.2 in terms of AUC. Normalization can improve the detection of CaP; however, the benefit of normalization is more obvious by combining together the pharmacokinetic features of a given model (e.g., A , k_{ep} , and k_{el} for Brix model), as previously done in traditional CAD system [137]. For the latter configuration, results are summarized by performing a ROC analysis and computing the AUC, as reported in Fig. 5.9. Quantification using normalized data outperforms quantification using un-normalized data in terms of classification performance apart of Hoffmann and Tofts population-based AIF models. The reasons behind the decrease of the AUC might be related to: (i) a poor fitting as discussed in Sect. ?? (cf., Hoffmann model) and (ii) a small number of patients while estimating some parameters (cf., Tofts model). The best classification performance are obtained using the semi-quantitative approach with an AUC of 0.655.

5.2.2.3 Classification of the entire enhanced DCE-MRI signal

As stated in the introduction, the quantification methods are extracting a set of parameters characterizing the enhancement DCE-MRI signal. However, this extraction might lead to a loss of information. This experiment is performed to assess if making use of the whole DCE-MRI signal instead of the just the pharmacokinetic parameters can improve the classification performance. Therefore, each enhanced DCE-MRI signal, normalized and un-normalized, is classified using a RF classifier in a LOPO CV fashion. The ROC analysis and AUC are reported in Fig. 5.10. Classification without normalization lead to the worst performance, with an AUC of 0.568. However, data normalization in conjunction with the use of the whole DCE-MRI signal is the strategy which outperforms all others, with an AUC of 0.666.

5.2.3 Discussion and conclusion

The experiments conducted in the previous section can give rise to several discussions. In Tofts quantification, two different approaches have been used to infer the pharmacokinetic parameters: using a population-based or a patient-based AIF. The patient-based AIF approach leads to better classification performance. However, there are two shortcomings to take into account while advancing this fact: (i) T_{10} parameter has been fixed and not computed from a T_1 map and (ii) the population-based AIF has been estimated from a cohort of only 17 patients. These two limitations have to be considered while advancing that population-based AIF modelling is outperforming patient-based AIF modelling.

The best classification performance is reached by normalizing the DCE-MRI data and use the whole enhanced signal as feature, emphasizing the fact that a loss of information while extracting quantitative parameters. Furthermore, this normalization is a less complex process than all quantification methods. However, this strategy suffers from one drawback: the training time of the RF classifier increases since that from 3 to 5 features, the feature space becomes a 40 dimensions space.

Nevertheless, this study is performed on a small cohort of patients using a single MRI machine. Generalizing the results of this study on a larger dataset

5.2 Normalization of DCE-MRI images

acquired from different commercial systems have to be considered to study the robustness of the proposed approach.

In this work, we presented a new method for normalizing/standardizing DCE-MRI data. This method aimed at reducing the inter-patient variations occurring during data acquisition. A graph-based approach was used to correct intensity offset in conjunction with a model-based correction to reduce time offset as well as intensity scaling. We show the benefit of our normalization method prior to extract quantitative and semi-quantitative features, with a significant improvement of the classification performance. Nevertheless, we also show that using the whole normalized DCE-MRI signal outperforms all quantitative approaches.

As avenues for future research, this normalization has to be part of a mp-MRI CAD system in which DCE-MRI modality needs to be combined with other complementary modalities.

5. NORMALIZATION/STANDARDIZATION OF T2W-MRI AND DCE-MRI IMAGES

References

- [1] I. Agalliu, R. Gern, S. Lanza, and R. D. Burk. Associations of high-grade prostate cancer with BRCA1 and BRCA2 founder mutations. *Clin. Cancer Res.*, 15(3):1112–1120, Feb 2009. 3
- [2] N. Ahmed, T. Natarajan, and K. Rao. Discrete cosine transform. *Computers, IEEE Transactions on*, C-23(1):90–93, 1974. ISSN 0018-9340. 58
- [3] M. A. Aizerman, E. A. Braverman, and L. Rozonoer. Theoretical foundations of the potential function method in pattern recognition learning. In *Automation and Remote Control*, number 25, pages 821–837, 1964. 68
- [4] O. Akin, E. Sala, C. S. Moskowitz, K. Kuroiwa, N. M. Ishill, D. Pucar, P. T. Scardino, and H. Hricak. Transition zone prostate cancers: features, detection, localization, and staging at endorectal MR imaging. *Radiology*, 239(3):784–792, Jun 2006. 10, 20
- [5] D. D. Alexander, P. J. Mink, C. A. Cushing, and B. Sceurman. A review and meta-analysis of prospective studies of red and processed meat intake and prostate cancer. *Nutr J*, 9:50, 2010. 3
- [6] M. Amadasun and R. King. Textural features corresponding to textural properties. *Systems, Man and Cybernetics, IEEE Transactions on*, 19(5):1264–1274, 1989. ISSN 0018-9472. 41
- [7] A. C. American Cancer Society. Cancer Facts and Figures 2010. <http://www.cancer.org/research/cancerfactsfigures>, 2010. URL <http://www.cancer.org/research/cancerfactsfigures>. Accessed: 2013-08-01.

REFERENCES

- [8] A. C. American Cancer Society. Cancer Facts and Figures 2013. <http://www.cancer.org/research/cancerfactsfigures>, 2013. Accessed: 2013-08-01. 3
- [9] D. Ampeliotis, A. Anonakoudi, K. Berberidis, and E. Z. Psarakis. Computer aided detection of prostate cancer using fused information from dynamic contrast enhanced and morphological magnetic resonance images. In *IEEE International Conference on Signal Processing and Communications*, pages 888–891, 2007. 24, 28, 40, 49, 53, 54, 55, 58, 60, 72, 83, 84
- [10] D. Ampeliotis, A. Anonakoudi, K. Berberidis, E. Z. Psarakis, and A. Kounoudes. A computer-aided system for the detection of prostate cancer based on magnetic resonance image analysis. In *International Symposium on Communications, Control and Signal Processing*, 2008. 24, 28, 40, 49, 53, 54, 55, 58, 60, 72, 83, 84, 85, 89
- [11] L. T. Amundadottir, P. Sulem, J. Gudmundsson, A. Helgason, A. Baker, B. A. Agnarsson, A. Sigurdsson, K. R. Benediktsdottir, J. B. Cazier, J. Sainz, M. Jakobsdottir, J. Kostic, D. N. Magnusdottir, S. Ghosh, K. Agnarsson, B. Birgisdottir, L. Le Roux, A. Olafsdottir, T. Blöndal, M. Andressdottir, O. S. Gretarsdottir, J. T. Bergthorsson, D. Gudbjartsson, A. Gylfason, G. Thorleifsson, A. Manolescu, K. Kristjansson, G. Geirsson, H. Isaksson, J. Douglas, J. E. Johansson, K. Balter, F. Wiklund, J. E. Montie, X. Yu, B. K. Suarez, C. Ober, K. A. Cooney, H. Gronberg, W. J. Catalona, G. V. Einarsson, R. B. Barkardottir, J. R. Gulcher, A. Kong, U. Thorsteinsdottir, and K. Stefansson. A common variant associated with prostate cancer in European and African populations. *Nat. Genet.*, 38(6):652–658, Jun 2006. 3
- [12] G. L. Andriole, E. D. Crawford, R. L. Grubb, S. S. Buys, D. Chia, T. R. Church, M. N. Fouad, E. P. Gelmann, P. A. Kvale, D. J. Reding, J. L. Weissfeld, L. A. Yokochi, B. O'Brien, J. D. Clapp, J. M. Rathmell, T. L. Riley, R. B. Hayes, B. S. Kramer, G. Izmirlian, A. B. Miller, P. F. Pinsky, P. C. Prorok, J. K. Gohagan, and C. D. Berg. Mortality results from a randomized Prostate-cancer screening trial. *New England Journal of Medicine*, 360(13):1310–1319, 2009. 4, 5

- [13] T. Antic, Y. Peng, Y. Jiang, M. L. Giger, S. Eggener, and A. Oto. A study of T2-weighted MR image texture features and diffusion-weighted MR image features for computer-aided diagnosis of prostate cancer. In *Proc. SPIE 8670, Medical Imaging 2013: Computer-Aided Diagnosis*, pages 86701H–86701H–6, 2013. 24, 53, 56, 58, 72, 73, 84, 85, 89
- [14] Y. Artan, D. Langer, M. Haider, T. H. Van der Kwast, A. Evans, M. Wernick, and I. Yetik. Prostate cancer segmentation with multispectral MRI using cost-sensitive Conditional Random Fields. In *Biomedical Imaging: From Nano to Macro, 2009. ISBI '09. IEEE International Symposium on*, pages 278–281, 2009. 24, 32, 40, 44, 51, 53, 54, 55, 62, 72, 80, 84, 85, 90, 97
- [15] Y. Artan, M. A. Haider, D. L. Langer, T. H. van der Kwast, A. J. Evans, Y. Yang, M. N. Wernick, J. Trachtenberg, and I. S. Yetik. Prostate cancer localization with multispectral MRI using cost-sensitive support vector machines and conditional random fields. *IEEE Trans Image Process*, 19(9):2444–2455, Sep 2010. 24, 32, 40, 44, 51, 53, 54, 55, 62, 72, 80, 84, 85, 90, 97
- [16] H. M. Awwad, J. Geisel, and R. Obeid. The role of choline in prostate cancer. *Clin. Biochem.*, 45(18):1548–1553, Dec 2012. 17, 18, 20
- [17] J. O. Barentsz, J. Richenberg, R. Clements, P. Choyke, S. Verma, G. Villeirs, O. Rouviere, V. Logager, and J. J. Futterer. ESUR prostate MR guidelines 2012. *Eur Radiol*, 22(4):746–757, Apr 2012. 4, 9, 10, 15, 16, 19, 20
- [18] M. Belkin and P. Niyogi. Laplacian eigenmaps and spectral techniques for embedding and clustering. In *Advances in Neural Information Processing Systems 14*, pages 585–591. MIT Press, 2001. 43, 68
- [19] S. Belongie, J. Malik, and J. Puzicha. Shape matching and object recognition using shape contexts. *Pattern Analysis and Machine Intelligence, IEEE Transactions on*, 24(4):509–522, 2002. ISSN 0162-8828. 59
- [20] A. Benassi, S. Cohen, and J. Istas. Identifying the multifractional function of a Gaussian process. *Statistics & Probability Letters*, 39(4):337 – 345, 1998. ISSN 0167-7152. 56

REFERENCES

- [21] M. A. Bernstein, D. M. Thomasson, and W. H. Perman. Improved detectability in low signal-to-noise ratio magnetic resonance images by means of a phase-corrected real reconstruction. *Medical Physics*, 16(5):813–817, 1989. 99
- [22] C. M. Bishop. *Pattern recognition and machine learning*. Springer-Verlag New York, Inc., Secaucus, NJ, USA, 2006. ISBN 0387310738. 71, 79, 80
- [23] F. L. Bookstein. Principal warps: thin-plate splines and the decomposition of deformations. *Pattern Analysis and Machine Intelligence, IEEE Transactions on*, 11(6):567–585, 1989. ISSN 0162-8828. 41
- [24] B. E. Boser, I. M. Guyon, and V. N. Vapnik. A training algorithm for optimal margin classifiers. In *Proceedings of the Fifth Annual Workshop on Computational Learning Theory*, COLT '92, pages 144–152, New York, NY, USA, 1992. ACM. ISBN 0-89791-497-X. 80
- [25] A. Bourdoumis, A. G. Papatsoris, M. Chrisofos, E. Efstathiou, A. Skolarikos, and C. Deliveliotis. The novel prostate cancer antigen 3 (PCA3) biomarker. *Int Braz J Urol*, 36(6):665–668, 2010. 5
- [26] L. Breiman. Random forests. *Machine Learning*, 45(1):5–32, 2001. 76
- [27] L. Breiman, J. Friedman, R. Olshen, and C. Stone. *Classification and regression trees*. Wadsworth and Brooks, Monterey, CA, 1984. 75, 76
- [28] J. Brenner, A. Chinnaiyan, and S. Tomlins. ETS fusion genes in prostate cancer. In D. J. Tindall, editor, *Prostate Cancer*, volume 16 of *Protein Reviews*, pages 139–183. Springer New York, 2013. ISBN 978-1-4614-6827-1. 5
- [29] G. Brix, W. Semmler, R. Port, L. R. Schad, G. Layer, and W. J. Lorenz. Pharmacokinetic parameters in cns gd-dtpa enhanced mr imaging. *Journal of computer assisted tomography*, 15(4):621–628, 1991. 105, 112
- [30] A. Buades, B. Coll, and J. Morel. A review of image denoising algorithms, with a new one. *Simul*, 4:490–530, 2005. 26

- [31] D. L. Buckley, C. Roberts, G. J. Parker, J. P. Logue, and C. E. Hutchinson. Prostate cancer: evaluation of vascular characteristics with dynamic contrast-enhanced T1-weighted MR imaging—initial experience. *Radiology*, 233(3):709–715, Dec 2004. 12
- [32] R. H. Byrd, P. Lu, J. Nocedal, and C. Zhu. A limited memory algorithm for bound constrained optimization. *SIAM J. Sci. Comput.*, 16(5):1190–1208, Sept. 1995. ISSN 1064-8275. 49, 74
- [33] A. Cameron, A. Modhafar, F. Khalvati, D. Lui, M. J. Shafiee, A. Wong, and M. Haider. Multiparametric mri prostate cancer analysis via a hybrid morphological-textural model. In *2014 36th Annual International Conference of the IEEE Engineering in Medicine and Biology Society*, pages 3357–3360. IEEE, 2014. 24, 51, 52, 53, 54, 55, 56, 58, 59, 60, 72, 75, 84, 85, 90
- [34] A. Cameron, F. Khalvati, M. A. Haider, and A. Wong. Maps: a quantitative radiomics approach for prostate cancer detection. *IEEE Transactions on Biomedical Engineering*, 63(6):1145–1156, 2016. 24, 51, 52, 53, 54, 55, 56, 58, 59, 60, 72, 75, 84, 85, 90
- [35] P. Carmeliet and R. K. Jain. Angiogenesis in cancer and other diseases. *Nature*, 407(6801):249–257, Sep 2000. 12
- [36] C. L. Carroll, F. G. Sommer, J. E. McNeal, and T. A. Stamey. The abnormal prostate: MR imaging at 1.5 T with histopathologic correlation. *Radiology*, 163(2):521–525, May 1987. 3
- [37] P. Castorina, P. P. Delsanto, and C. Guiot. Classification scheme for phenomenological universalities in growth problems in physics and other sciences. *Phys. Rev. Lett.*, 96:188701, May 2006. 62
- [38] H. P. Chan, B. Sahiner, M. A. Helvie, N. Petrick, M. A. Roubidoux, T. E. Wilson, D. D. Adler, C. Paramagul, J. S. Newman, and S. Sanjay-Gopal. Improvement of radiologists’ characterization of mammographic masses by

REFERENCES

- using computer-aided diagnosis: an ROC study. *Radiology*, 212(3):817–827, Sep 1999. 6
- [39] I. Chan, W. Wells, R. V. Mulkern, S. Haker, J. Zhang, K. H. Zou, S. E. Maier, and C. M. Tempany. Detection of prostate cancer by integration of line-scan diffusion, T2-mapping and T2-weighted magnetic resonance imaging; a multichannel statistical classifier. *Med Phys*, 30(9):2390–2398, Sep 2003. 24, 53, 55, 56, 72, 73, 80, 84, 85, 89
- [40] J. Chappelow, B. N. Bloch, N. Rofsky, E. Genega, R. Lenkinski, W. DeWolf, and A. Madabhushi. Elastic registration of multimodal prostate MRI and histology via multiattribute combined mutual information. *Med Phys*, 38(4):2005–2018, Apr 2011. 48, 50
- [41] J. Chen, J. Yao, and D. Thomasson. Automatic determination of arterial input function for dynamic contrast enhanced mri in tumor assessment. In *International Conference on Medical Image Computing and Computer-Assisted Intervention*, pages 594–601. Springer, 2008. doi: 10.1007/978-3-540-85988-8_71. 113
- [42] L. Chen, Z. Weng, L. Goh, and M. Garland. An efficient algorithm for automatic phase correction of {NMR} spectra based on entropy minimization . *Journal of Magnetic Resonance*, 158(12):164 – 168, 2002. ISSN 1090-7807. 35, 39
- [43] Y. J. Choi, J. K. Kim, N. Kim, K. W. Kim, E. K. Choi, and K. S. Cho. Functional MR imaging of prostate cancer. *Radiographics*, 27:63–75, 2007. 2, 12, 14, 15, 16, 17, 19
- [44] R. Chou, J. M. Croswell, T. Dana, C. Bougatsos, I. Blazina, R. Fu, K. Gleitsmann, H. C. Koenig, C. Lam, A. Maltz, J. B. Rugge, and K. Lin. Screening for prostate cancer: a review of the evidence for the U.S. Preventive Services Task Force. *Ann. Intern. Med.*, 155(11):762–771, Dec 2011. 4
- [45] A. Chung, F. Khalvati, M. Shafiee, M. Haider, and A. Wong. Prostate cancer detection via a quantitative radiomics-driven conditional random field

- framework. *IEEE Access*, 3:2531–2541, 2015. 24, 53, 55, 56, 58, 64, 66, 72, 80, 84, 90, 92
- [46] F. V. Coakley and H. Hricak. Radiologic anatomy of the prostate gland: a clinical approach. *Radiol. Clin. North Am.*, 38:15–30, Jan 2000. 1
- [47] R. J. Cohen, B. A. Shannon, M. Phillips, R. E. Moorin, T. M. Wheeler, and K. L. Garrett. Central zone carcinoma of the prostate gland: a distinct tumor type with poor prognostic features. *J. Urol.*, 179(5):1762–1767, May 2008. 3
- [48] R. Coifman and M. Wickerhauser. Entropy-based algorithms for best basis selection. *Information Theory, IEEE Transactions on*, 38(2):713–718, 1992. ISSN 0018-9448. 64
- [49] T. Coleman and Y. Li. An interior trust region approach for nonlinear minimization subject to bounds. Technical report, Cornell University, 1993. 63
- [50] T. F. Cootes, C. J. Taylor, D. H. Cooper, and J. Graham. Active shape models—Their training and application. *Comput. Vis. Image Underst.*, 61(1):38–59, Jan. 1995. ISSN 1077-3142. 42
- [51] C. Cortes and V. Vapnik. Support-Vector networks. *Machine Learning*, 20(3):273–297, 1995. ISSN 0885-6125. 79
- [52] L. C. Costello and R. B. Franklin. The clinical relevance of the metabolism of prostate cancer; zinc and tumor suppression: connecting the dots. *Mol. Cancer*, 5:17, 2006. 17, 18, 20
- [53] M. Cruz, K. Tsuda, Y. Narumi, Y. Kuroiwa, T. Nose, Y. Kojima, A. Okuyama, S. Takahashi, K. Aozasa, J. O. Barentsz, and H. Nakamura. Characterization of low-intensity lesions in the peripheral zone of prostate on pre-biopsy endorectal coil MR imaging. *Eur Radiol*, 12(2):357–365, Feb 2002. 10

REFERENCES

- [54] N. Dalal and B. Triggs. Histograms of oriented gradients for human detection. In *Computer Vision and Pattern Recognition, 2005. CVPR 2005. IEEE Computer Society Conference on*, volume 1, pages 886–893 vol. 1, 2005. 59
- [55] J. G. Daugman. Uncertainty relation for resolution in space, spatial frequency, and orientation optimized by two-dimensional visual cortical filters. *J Opt Soc Am A*, 2(7):1160–1169, Jul 1985. 55
- [56] G. Davis, S. Mallat, and M. Avellaneda. Adaptive greedy approximations. *Constructive approximation*, 13(1):57–98, 1997. 70
- [57] J. C. Dean and C. C. Ilvento. Improved cancer detection using computer-aided detection with diagnostic and screening mammography: prospective study of 104 cancers. *AJR Am J Roentgenol*, 187(1):20–28, Jul 2006. 6
- [58] N. B. Delongchamps, M. Peyromaure, A. Schull, F. Beuvon, N. Bouazza, T. Flam, M. Zerbib, N. Muradyan, P. Legman, and F. Cornud. Prebiopsy magnetic resonance imaging and prostate cancer detection: comparison of random and targeted biopsies. *J. Urol.*, 189(2):493–499, Feb 2013. 5
- [59] C. Delpierre, S. Lamy, M. Kelly-Irving, F. Molinie, M. Velten, B. Tretarre, A. S. Woronoff, A. Buemi, B. Lapotre-Ledoux, S. Bara, A. V. Guizard, M. Colonna, and P. Grosclaude. Life expectancy estimates as a key factor in over-treatment: the case of prostate cancer. *Cancer Epidemiol*, 37(4):462–468, Aug 2013. 5
- [60] A. Devos, L. Lukas, J. A. Suykens, L. Vanhamme, A. R. Tate, F. A. Howe, C. Majos, A. Moreno-Torres, M. van der Graaf, C. Arus, and S. Van Huffel. Classification of brain tumours using short echo time ^1H MR spectra. *J. Magn. Reson.*, 170(1):164–175, Sep 2004. 38, 39
- [61] D. L. Donoho and J. M. Johnstone. Ideal spatial adaptation by wavelet shrinkage. *Biometrika*, 81(3):425–455, 1994. 28
- [62] K. W. Doo, D. J. Sung, B. J. Park, M. J. Kim, S. B. Cho, Y. W. Oh, Y. H. Ko, and K. S. Yang. Detectability of low and intermediate or high risk prostate

- cancer with combined T2-weighted and diffusion-weighted MRI. *Eur Radiol*, 22(8):1812–1819, Aug 2012. 16
- [63] B. Efron. Bootstrap methods: Another look at the jackknife. *The Annals of Statistics*, 7(1):1–26, 01 1979. 76
- [64] B. Efron. Estimating the error rate of a prediction rule: Improvement on cross-validation. *Journal of the American Statistical Association*, 78(382): pp. 316–331, 1983. ISSN 01621459. 85
- [65] M. Elad. *Sparse and redundant representations: from theory to applications in signal and image processing*. Springer Publishing Company, Incorporated, 1st edition, 2010. 70
- [66] J. I. Epstein, W. C. Allsbrook, M. B. Amin, and L. L. Egevad. The 2005 International Society of Urological Pathology (ISUP) Consensus Conference on Gleason Grading of Prostatic Carcinoma. *Am. J. Surg. Pathol.*, 29(9): 1228–1242, Sep 2005. 4
- [67] R. Etzioni, D. F. Penson, J. M. Legler, D. di Tommaso, R. Boer, P. H. Gann, and E. J. Feuer. Overdiagnosis due to prostate-specific antigen screening: lessons from U.S. prostate cancer incidence trends. *J. Natl. Cancer Inst.*, 94 (13):981–990, Jul 2002. 4
- [68] F. M. Fennessy, A. Fedorov, T. Penzkofer, K. W. Kim, M. S. Hirsch, M. G. Vangel, P. Masry, T. A. Flood, M.-C. Chang, C. M. Tempany, et al. Quantitative pharmacokinetic analysis of prostate cancer dce-mri at 3t: comparison of two arterial input functions on cancer detection with digitized whole mount histopathological validation. *Magnetic resonance imaging*, 33(7):886–894, 2015. doi: 10.1016/j.mri.2015.02.008. 113, 115
- [69] J. Ferlay, H. R. Shin, F. Bray, D. Forman, C. Mathers, and D. M. Parkin. Estimates of worldwide burden of cancer in 2008: GLOBOCAN 2008. *Int. J. Cancer*, 127(12):2893–2917, Dec 2010. 3
- [70] I. Fodor. A survey of dimension reduction techniques, 2002. 67

REFERENCES

- [71] A. Fred and A. Jain. Combining multiple clusterings using evidence accumulation. *Pattern Analysis and Machine Intelligence, IEEE Transactions on*, 27(6):835–850, 2005. ISSN 0162-8828. 73
- [72] M. L. Freedman, C. A. Haiman, N. Patterson, G. J. McDonald, A. Tandon, A. Waliszewska, K. Penney, R. G. Steen, K. Ardlie, E. M. John, I. Oakley-Girvan, A. S. Whittemore, K. A. Cooney, S. A. Ingles, D. Altshuler, B. E. Henderson, and D. Reich. Admixture mapping identifies 8q24 as a prostate cancer risk locus in African-American men. *Proc. Natl. Acad. Sci. U.S.A.*, 103(38):14068–14073, Sep 2006. 3
- [73] Y. Freund and R. Schapire. A decision-theoretic generalization of on-line learning and an application to boosting. *Journal of Computer and System Sciences*, 55(1):119 – 139, 1997. ISSN 0022-0000. 75
- [74] J. Friedman. Regularized discriminant analysis. *Journal of the American Statistical Association*, 84(405):pp. 165–175, 1989. ISSN 01621459. 73
- [75] J. Friedman, T. Hastie, and R. Tibshirani. Additive logistic regression: a statistical view of boosting. *Annals of Statistics*, 28:2000, 1998. 76
- [76] D. Gabor. Theory of communication. Part 1: The analysis of information. *Electrical Engineers - Part III: Radio and Communication Engineering, Journal of the Institution of*, 93(26):429–441, 1946. 55
- [77] C. Gasparovic, T. Song, D. Devier, H. J. Bockholt, A. Caprihan, P. G. Mullins, S. Posse, R. E. Jung, and L. A. Morrison. Use of tissue water as a concentration reference for proton spectroscopic imaging. *Magnetic resonance in medicine*, 55(6):1219–1226, 2006. 64
- [78] Geckomedia. Natom Anatomy, 06 2011. URL <http://www.natomshop.com/>. 2
- [79] S. Ghose, A. Oliver, R. Marti, X. Llado, J. C. Vilanova, J. Freixenet, J. Mitra, D. Sidibe, and F. Meriaudeau. A survey of prostate segmentation

methodologies in ultrasound, magnetic resonance and computed tomography images. *Comput Methods Programs Biomed*, 108(1):262–287, Oct 2012. 40

- [80] V. Giannini, A. Vignati, S. Mazzetti, M. De Luca, C. Bracco, M. Stasi, F. Russo, E. Armando, and D. Regge. A prostate CAD system based on multiparametric analysis of DCE T1-w, and DW automatically registered images. In *Proc. SPIE 8670, Medical Imaging 2013: Computer-Aided Diagnosis*, pages 86703E–86703E–6, 2013. 24, 49, 50, 51, 53, 54, 55, 62, 72, 75, 84, 85, 89, 90
- [81] V. Giannini, S. Mazzetti, A. Vignati, F. Russo, E. Bollito, F. Porpiglia, M. Stasi, and D. Regge. A fully automatic computer aided diagnosis system for peripheral zone prostate cancer detection using multi-parametric magnetic resonance imaging. *Computerized Medical Imaging and Graphics*, 46: 219–226, 2015. doi: 10.1016/j.compmedimag.2015.09.001. 24, 30, 34, 40, 43, 44, 49, 50, 53, 54, 55, 60, 62, 72, 80, 85, 89, 115
- [82] P. Gibbs, D. J. Tozer, G. P. Liney, and L. W. Turnbull. Comparison of quantitative T2 mapping and diffusion-weighted imaging in the normal and pathologic prostate. *Magn Reson Med*, 46(6):1054–1058, Dec 2001. 11, 20
- [83] M. L. Giger, H. P. Chan, and J. Boone. Anniversary paper: History and status of CAD and quantitative image analysis: the role of Medical Physics and AAPM. *Med Phys*, 35(12):5799–5820, Dec 2008. 6, 21
- [84] E. Giovannucci, Y. Liu, E. A. Platz, M. J. Stampfer, and W. C. Willett. Risk factors for prostate cancer incidence and progression in the health professionals follow-up study. *Int. J. Cancer*, 121(7):1571–1578, Oct 2007. 3
- [85] G. F. Giskeodegard, H. Bertilsson, K. M. Selnaes, A. J. Wright, T. F. Bathen, T. Viset, J. Halgunset, A. Angelsen, I. S. Gribbestad, and M. B. Tessem. Spermine and citrate as metabolic biomarkers for assessing prostate cancer aggressiveness. *PLoS ONE*, 8(4):e62375, 2013. 17, 18, 19, 20

REFERENCES

- [86] D. F. Gleason. *Urologic pathology: The prostate*, chapter The Veteran’s Administration Cooperative Urologic Research Group: histologic grading and clinical staging of prostatic carcinoma, page 171198. Lea and Febiger., 1977. 4
- [87] A. Gliozzi, S. Mazzetti, P. P. Delsanto, D. Regge, and M. Stasi. Phenomenological universalities: a novel tool for the analysis of dynamic contrast enhancement in magnetic resonance imaging. *Physics in medicine and biology*, 56(3):573, 2011. 105, 106, 115
- [88] S. N. Goodman. Toward evidence-based medical statistics. 1: The P value fallacy. *Ann. Intern. Med.*, 130(12):995–1004, Jun 1999. 65
- [89] I. Gribbestad, K. Gjesdal, G. Nilsen, S. Lundgren, M. Hjelstuen, and A. Jackson. An introduction to dynamic contrast-enhanced MRI in oncology. In A. Jackson, D. Buckley, and G. Parker, editors, *Dynamic Contrast-Enhanced Magnetic Resonance Imaging in Oncology*, Medical Radiology, pages 1–22. Springer Berlin Heidelberg, 2005. ISBN 978-3-540-42322-5. 11, 12
- [90] E. Haacke, R. Brown, M. Thompson, and R. Venkatesan. *Magnetic resonance imaging: Physical principles and sequence design*. Wiley, 1999. ISBN 9780471351283. 18
- [91] G. P. Haas, N. B. Delongchamps, R. F. Jones, V. Chandan, A. M. Serio, A. J. Vickers, M. Jumbelic, G. Threatte, R. Korets, H. Lilja, and G. de la Roza. Needle biopsies on autopsy prostates: sensitivity of cancer detection based on true prevalence. *J. Natl. Cancer Inst.*, 99(19):1484–1489, Oct 2007. 5
- [92] T. Hambrock, D. M. Somford, H. J. Huisman, I. M. van Oort, J. A. Witjes, C. A. Hulsbergen-van de Kaa, T. Scheenen, and J. O. Barentsz. Relationship between apparent diffusion coefficients at 3.0-T MR imaging and Gleason grade in peripheral zone prostate cancer. *Radiology*, 259(2):453–461, May 2011. 16, 20

- [93] T. Hambrock, P. C. Vos, C. A. Hulsbergen-van de Kaa, J. O. Barentsz, and H. J. Huisman. Prostate cancer: computer-aided diagnosis with multiparametric 3-T MR imaging—effect on observer performance. *Radiology*, 266(2):521–530, Feb 2013. 6
- [94] N. Hara, M. Okuizumi, H. Koike, M. Kawaguchi, and V. Bilim. Dynamic contrast-enhanced magnetic resonance imaging (DCE-MRI) is a useful modality for the precise detection and staging of early prostate cancer. *Prostate*, 62(2):140–147, Feb 2005. 4
- [95] R. Haralick, K. Shanmugam, and I. Dinstein. Textural features for image classification. *Systems, Man and Cybernetics, IEEE Transactions on*, SMC-3 (6):610–621, 1973. ISSN 0018-9472. 56, 57
- [96] H. He, E. Garcia, et al. Learning from imbalanced data. *Knowledge and Data Engineering, IEEE Transactions on*, 21(9):1263–1284, 2009. 93
- [97] J. V. Hegde, R. V. Mulkern, L. P. Panych, F. M. Fennessy, A. Fedorov, S. E. Maier, and C. M. Tempany. Multiparametric MRI of prostate cancer: an update on state-of-the-art techniques and their performance in detecting and localizing prostate cancer. *J Magn Reson Imaging*, 37(5):1035–1054, May 2013. 6, 11
- [98] A. Heidenreich, P. A. Abrahamsson, W. Artibani, J. Catto, F. Montorsi, H. Van Poppel, M. Wirth, and N. Mottet. Early detection of prostate cancer: European Association of Urology recommendation. *Eur. Urol.*, 64(3):347–354, Sep 2013. 4
- [99] M. Heilmann, F. Kiessling, M. Enderlin, and L. R. Schad. Determination of pharmacokinetic parameters in dce mri: consequence of nonlinearity between contrast agent concentration and signal intensity. *Investigative radiology*, 41 (6):536–543, 2006. doi: 10.1097/01.rli.0000209607.99200.53. 105
- [100] A. Hero, B. Ma, O. Michel, and J. Gorman. Applications of entropic spanning graphs. *Signal Processing Magazine, IEEE*, 19(5):85–95, 2002. ISSN 1053-5888. 48

REFERENCES

- [101] C. M. Hoeks, J. O. Barentsz, T. Hambrock, D. Yakar, D. M. Somford, S. W. Heijmink, T. W. Scheenen, P. C. Vos, H. Huisman, I. M. van Oort, J. A. Witjes, A. Heerschap, and J. J. Futterer. Prostate cancer: multiparametric MR imaging for detection, localization, and staging. *Radiology*, 261(1):46–66, Oct 2011. 4, 5, 10, 12, 13, 14, 18
- [102] R. M. Hoffman, F. D. Gilliland, J. W. Eley, L. C. Harlan, R. A. Stephenson, J. L. Stanford, P. C. Albertson, A. S. Hamilton, W. C. Hunt, and A. L. Potosky. Racial and ethnic differences in advanced-stage prostate cancer: the Prostate Cancer Outcomes Study. *J. Natl. Cancer Inst.*, 93(5):388–395, Mar 2001. 3
- [103] U. Hoffmann, G. Brix, M. V. Knopp, T. Heβ, and W. J. Lorenz. Pharmacokinetic mapping of the breast: a new method for dynamic mr mammography. *Magnetic resonance in medicine*, 33(4):506–514, 1995. doi: 10.1002/mrm.1910330408. 112
- [104] H. Hricak, R. D. Williams, D. B. Spring, K. L. Moon, M. W. Hedgcock, R. A. Watson, and L. E. Crooks. Anatomy and pathology of the male pelvis by magnetic resonance imaging. *AJR Am J Roentgenol*, 141(6):1101–1110, Dec 1983. 7, 9, 10, 20
- [105] H. Hricak, G. C. Dooms, J. E. McNeal, A. S. Mark, M. Marotti, A. Avallone, M. Pelzer, E. C. Proctor, and E. A. Tanagho. MR imaging of the prostate gland: normal anatomy. *AJR Am J Roentgenol*, 148:51–58, Jan 1987. 1, 10, 20
- [106] R. A. Huch Boni, J. A. Boner, U. M. Lutolf, F. Trinkler, D. M. Pestalozzi, and G. P. Krestin. Contrast-enhanced endorectal coil MRI in local staging of prostate carcinoma. *J Comput Assist Tomogr*, 19(2):232–237, 1995. 7
- [107] J. Hugosson, S. Carlsson, G. Aus, S. Bergdahl, A. Khatami, P. Lodding, C. G. Pihl, J. Stranne, E. Holmberg, and H. Lilja. Mortality results from the Göteborg randomised population-based prostate-cancer screening trial. *Lancet Oncol.*, 11(8):725–732, Aug 2010. 4, 5

- [108] H. Huisman, P. Vos, G. Litjens, T. Hambrock, and J. Barentsz. Computer aided detection of prostate cancer using T2, DWI and DCE MRI: methods and clinical applications. In *Proceedings of the 2010 international conference on Prostate cancer imaging: computer-aided diagnosis, prognosis, and intervention*, MICCAI'10, pages 4–14, Berlin, Heidelberg, 2010. Springer-Verlag. ISBN 3-642-15988-5, 978-3-642-15988-6. 43
- [109] H. J. Huisman, M. R. Engelbrecht, and J. O. Barentsz. Accurate estimation of pharmacokinetic contrast-enhanced dynamic mri parameters of the prostate. *Journal of Magnetic Resonance Imaging*, 13(4):607–614, 2001. doi: 10.1002/jmri.1085. 106, 116
- [110] T. A. Huisman. Diffusion-weighted imaging: basic concepts and application in cerebral stroke and head trauma. *Eur Radiol*, 13(10):2283–2297, Oct 2003. 15, 20
- [111] L. Ibanez, W. Schroeder, L. Ng, and J. Cates. The itk software guide. 2005. 118
- [112] Y. Itou, K. Nakanishi, Y. Narumi, Y. Nishizawa, and H. Tsukuma. Clinical utility of apparent diffusion coefficient (ADC) values in patients with prostate cancer: can ADC values contribute to assess the aggressiveness of prostate cancer? *J Magn Reson Imaging*, 33(1):167–172, Jan 2011. 16, 20
- [113] G. J. Jager, E. T. Ruijter, C. A. van de Kaa, J. J. de la Rosette, G. O. Oosterhof, J. R. Thornbury, S. H. Ruijs, and J. O. Barentsz. Dynamic TurboFLASH subtraction technique for contrast-enhanced MR imaging of the prostate: correlation with histopathologic results. *Radiology*, 203(3): 645–652, Jun 1997. 13
- [114] I. T. Jolliffe. *Principal Component Analysis*. Springer, second edition, Oct. 2002. ISBN 0387954422. 67
- [115] M. Jungke, W. Von Seelen, G. Bielke, S. Meindl, M. Grigat, and P. Pfannenstiel. A system for the diagnostic use of tissue characterizing parameters in

REFERENCES

- NMR-tomography. In *Proc. of Information Processing in Medical Imaging*, volume 87, pages 471–481, 1987. 29
- [116] Y. Kaji, J. Kurhanewicz, H. Hricak, D. L. Sokolov, L. R. Huang, S. J. Nelson, and D. B. Vigneron. Localizing prostate cancer in the presence of postbiopsy changes on MR images: role of proton MR spectroscopic imaging. *Radiology*, 206(3):785–790, Mar 1998. 19
- [117] Z. Kato and T. Pong. A Markov random field image segmentation model using combined color and texture features. In W. Skarbek, editor, *Computer Analysis of Images and Patterns*, volume 2124 of *Lecture Notes in Computer Science*, pages 547–554. Springer Berlin Heidelberg, 2001. ISBN 978-3-540-42513-7. 83, 84
- [118] Z. Kato and J. Zerubia. *Markov Random Fields in Image Segmentation. Collection Foundation and Trends in Signal Processing*. Now Editor, World Scientific, Sept. 2012. 84
- [119] B. M. Kelm, B. H. Menze, C. M. Zechmann, K. T. Baudendistel, and F. A. Hamprecht. Automated estimation of tumor probability in prostate magnetic resonance spectroscopic imaging: pattern recognition vs quantification. *Magn Reson Med*, 57(1):150–159, Jan 2007. 24, 36, 40, 51, 54, 63, 72, 74, 76, 78, 84, 85
- [120] S. Kety. The theory and applications of the exchange of inert gas at the lungs and tissues. *Pharmacol. Rev.*, 3(1):1–41, Mar 1951. 13
- [121] F. Khalvati, A. Wong, and M. A. Haider. Automated prostate cancer detection via comprehensive multi-parametric magnetic resonance imaging texture feature models. *BMC medical imaging*, 15(1):27, 2015. 24, 51, 53, 55, 56, 58, 64, 66, 72, 80, 84, 85, 89, 90, 92
- [122] J. K. Kim, S. S. Hong, Y. J. Choi, S. H. Park, H. Ahn, C. S. Kim, and K. S. Cho. Wash-in rate on the basis of dynamic contrast-enhanced MRI: usefulness for prostate cancer detection and localization. *J Magn Reson Imaging*, 22(5):639–646, Nov 2005. 13

- [123] A. P. Kirkham, M. Emberton, and C. Allen. How good is MRI at detecting and characterising cancer within the prostate? *Eur. Urol.*, 50(6):1163–1174, Dec 2006. 10, 17
- [124] R. Kirsch. Computer determination of the constituent structure of biological images . *Computers and Biomedical Research*, 4(3):315 – 328, 1971. ISSN 0010-4809. 55
- [125] D. M. Koh and D. J. Collins. Diffusion-weighted MRI in the body: applications and challenges in oncology. *AJR Am J Roentgenol*, 188(6):1622–1635, Jun 2007. 14
- [126] J. Kurhanewicz, D. B. Vigneron, H. Hricak, P. Narayan, P. Carroll, and S. J. Nelson. Three-dimensional H-1 MR spectroscopic imaging of the in situ human prostate with high (0.24-0.7-cm3) spatial resolution. *Radiology*, 198(3):795–805, Mar 1996. 7
- [127] D. L. Langer, T. H. van der Kwast, A. J. Evans, J. Trachtenberg, B. C. Wilson, and M. A. Haider. Prostate cancer detection with multi-parametric MRI: logistic regression analysis of quantitative T2, diffusion-weighted imaging, and dynamic contrast-enhanced MRI. *J Magn Reson Imaging*, 30(2):327–334, Aug 2009. 24, 53, 54, 55, 62, 72, 85, 89, 91
- [128] T. R. Langerak, U. A. van der Heide, A. N. Kotte, M. A. Viergever, M. van Vulpen, and J. P. Pluim. Label fusion in atlas-based segmentation using a selective and iterative method for performance level estimation (simple). *IEEE Transactions on Medical Imaging*, 29(12):2000–2008, 2010. 41
- [129] H. B. Larsson, T. Fritz-Hansen, E. Rostrup, L. Sondergaard, P. Ring, and O. Henriksen. Myocardial perfusion modeling using MRI. *Magn Reson Med*, 35(5):716–726, May 1996. 13
- [130] T. Laudadio, N. Mastronardi, L. Vanhamme, P. V. Hecke, and S. V. Huf-fel. Improved Lanczos algorithms for blackbox {MRS} data quantitation. *Journal of Magnetic Resonance*, 157(2):292 – 297, 2002. ISSN 1090-7807. 37

REFERENCES

- [131] D. Le Bihan, E. Breton, D. Lallemand, P. Grenier, E. Cabanis, and M. Laval-Jeantet. MR imaging of intravoxel incoherent motions: application to diffusion and perfusion in neurologic disorders. *Radiology*, 161(2):401–407, Nov 1986. 15, 16
- [132] D. Le Bihan, E. Breton, D. Lallemand, M. L. Aubin, J. Vignaud, and M. Laval-Jeantet. Separation of diffusion and perfusion in intravoxel incoherent motion MR imaging. *Radiology*, 168(2):497–505, Aug 1988. 14
- [133] J. Lehaire, R. Flamary, O. Rouvière, and C. Lartizien. Computer-aided diagnostic system for prostate cancer detection and characterization combining learned dictionaries and supervised classification. In *2014 IEEE International Conference on Image Processing (ICIP)*, pages 2251–2255. IEEE, 2014. 24, 34, 40, 44, 51, 53, 54, 55, 56, 58, 60, 62, 64, 66, 69, 72, 74, 80, 84, 85, 89, 92
- [134] K. H. Leissner and L. E. Tisell. The weight of the human prostate. *Scand. J. Urol. Nephrol.*, 13(2):137–142, 1979. 1
- [135] G. Lemaître. Absolute quantification at 3 T. Master’s thesis, Université de Bourgogne, Heriot-Watt University, Universitat de Girona, 2011. 18, 19
- [136] G. Lemaitre. lemaitre-2016-nov: 0.1.1, Sept. 2016. URL <http://dx.doi.org/10.5281/zenodo.61612>. 118
- [137] G. Lemaitre, R. Marti, J. Freixenet, J. C. Vilanova, P. M. Walker, and F. Mériauveau. Computer-aided detection and diagnosis for prostate cancer based on mono and multi-parametric mri: A review. *Computers in Biology and Medicine*, 60:8–31, 2015. 105, 112, 121
- [138] G. Lemaitre, M. R. Dastjerdi, J. Massich, J. C. Vilanova, P. M. Walker, J. Freixenet, A. Meyer-Baese, F. Mériauveau, and R. Marti. Normalization of t2w-mri prostate images using rician a priori. In *SPIE Medical Imaging*, pages 978529–978529. International Society for Optics and Photonics, 2016. doi: 10.1117/12.2216072. 107

- [139] G. Lemaitre, R. Martí, and F. Meriaudeau. DCE-MRI prostate images, Aug. 2016. URL <http://dx.doi.org/10.5281/zenodo.61163>. 118
- [140] T. Leung and J. Malik. Representing and recognizing the visual appearance of materials using three-dimensional textons. *International journal of computer vision*, 43(1):29–44, 2001. 58
- [141] F. Li, M. Aoyama, J. Shiraishi, H. Abe, Q. Li, K. Suzuki, R. Engelmann, S. Sone, H. Macmahon, and K. Doi. Radiologists’ performance for differentiating benign from malignant lung nodules on high-resolution CT using computer-estimated likelihood of malignancy. *AJR Am J Roentgenol*, 183(5):1209–1215, Nov 2004. 6
- [142] H. Li, M. L. Giger, O. I. Olopade, A. Margolis, L. Lan, and M. R. Chinander. Computerized texture analysis of mammographic parenchymal patterns of digitized mammograms. *Acad Radiol*, 12(7):863–873, Jul 2005. 41
- [143] Q. Li, S. Sone, and K. Doi. Selective enhancement filters for nodules, vessels, and airway walls in two- and three-dimensional CT scans. *Med Phys*, 30(8):2040–2051, Aug 2003. 51
- [144] S. Z. Li. Robustizing robust M-estimation using deterministic annealing. *Pattern Recognition*, 29:159–166, 1996. 30
- [145] C. A. Lieber and A. Mahadevan-Jansen. Automated method for subtraction of fluorescence from biological Raman spectra. *Appl Spectrosc*, 57(11):1363–1367, Nov 2003. 38
- [146] G. P. Liney, A. J. Knowles, D. J. Manton, L. W. Turnbull, S. J. Blackband, and A. Horsman. Comparison of conventional single echo and multi-echo sequences with a fast spin-echo sequence for quantitative T2 mapping: application to the prostate. *J Magn Reson Imaging*, 6(4):603–607, 1996. 11
- [147] G. P. Liney, M. Lowry, L. W. Turnbull, D. J. Manton, A. J. Knowles, S. J. Blackband, and A. Horsman. Proton MR T2 maps correlate with the citrate concentration in the prostate. *NMR Biomed*, 9(2):59–64, Apr 1996. 11, 20

REFERENCES

- [148] G. P. Liney, L. W. Turnbull, M. Lowry, L. S. Turnbull, A. J. Knowles, and A. Horsman. In vivo quantification of citrate concentration and water T2 relaxation time of the pathologic prostate gland using 1H MRS and MRI. *Magn Reson Imaging*, 15(10):1177–1186, 1997. 11, 20
- [149] H. Ling and A. C. Bovik. Smoothing low-snr molecular images via anisotropic median-diffusion. *IEEE Transactions on Medical Imaging*, 21(4):377–384, 2002. 27
- [150] G. Litjens, O. Debats, W. van de Ven, N. Karssemeijer, and H. Huisman. A pattern recognition approach to zonal segmentation of the prostate on MRI. *Med Image Comput Comput Assist Interv*, 15(Pt 2):413–420, 2012. 41
- [151] G. Litjens, O. Debats, J. Barentsz, N. Karssemeijer, and H. Huisman. Computer-aided detection of prostate cancer in MRI. *Medical Imaging, IEEE Transactions on*, 33(5):1083–1092, May 2014. ISSN 0278-0062. 24, 41, 44, 51, 53, 54, 55, 58, 59, 72, 76, 84, 87, 88, 89, 91, 92, 121
- [152] G. Litjens, R. Toth, W. van de Ven, C. Hoeks, S. Kerkstra, B. van Ginneken, G. Vincent, G. Guillard, N. Birbeck, J. Zhang, R. Strand, F. Malmberg, Y. Ou, C. Davatzikos, M. Kirschner, F. Jung, J. Yuan, W. Qiu, Q. Gao, P. E. Edwards, B. Maan, F. van der Heijden, S. Ghose, J. Mitra, J. Dowling, D. Barratt, H. Huisman, and A. Madabhushi. Evaluation of prostate segmentation algorithms for MRI: the PROMISE12 challenge. *Med Image Anal*, 18(2):359–373, Feb 2014. 41
- [153] G. J. S. Litjens, P. C. Vos, J. O. Barentsz, N. Karssemeijer, and H. J. Huisman. Automatic computer aided detection of abnormalities in multi-parametric prostate MRI. In *Proc. SPIE 7963, Medical Imaging 2011: Computer-Aided Diagnosis*, pages 79630T–79630T–7, 2011. 24, 43, 44, 51, 52, 53, 54, 55, 58, 72, 80, 84, 85, 91
- [154] G. J. S. Litjens, J. O. Barentsz, N. Karssemeijer, and H. J. Huisman. Automated computer-aided detection of prostate cancer in MR images: from a

- whole-organ to a zone-based approach. In *Proc. SPIE 8315, Medical Imaging 2012: Computer-Aided Diagnosis*, pages 83150G–83150G–6, 2012. 24, 41, 44, 51, 52, 53, 54, 55, 58, 59, 71, 72, 80, 84, 85, 92
- [155] P. Liu, S. Wang, B. Turkbey, K. Grant, P. Pinto, P. and Choyke, B. J. Wood, and R. M. Summers. A prostate cancer computer-aided diagnosis system using multimodal magnetic resonance imaging and targeted biopsy labels. In *Proc. SPIE 8670, Medical Imaging 2013: Computer-Aided Diagnosis*, pages 86701G–86701G–6, 2013. 24, 33, 53, 54, 58, 59, 72, 80, 85, 89, 91
- [156] W. Liu, B. Turkbey, J. Senegas, S. Remmele, S. Xu, J. Kruecker, M. Bernardo, B. J. Wood, P. A. Pinto, and P. L. Choyke. Accelerated T2 mapping for characterization of prostate cancer. *Magn Reson Med*, 65(5):1400–1406, May 2011. 11, 20
- [157] X. Liu, D. L. Langer, M. A. Haider, Y. Yang, M. N. Wernick, and I. S. Yetik. Prostate cancer segmentation with simultaneous estimation of Markov random field parameters and class. *IEEE Trans Med Imaging*, 28(6):906–915, Jun 2009. 24, 51, 53, 54, 55, 62, 72, 84, 85, 90
- [158] R. Lopes, A. Ayache, N. Makni, P. Puech, A. Villers, S. Mordon, and N. Be- trouni. Prostate cancer characterization on MR images using fractal features. *Med Phys*, 38(1):83–95, Jan 2011. 24, 28, 40, 51, 53, 54, 56, 60, 72, 76, 80, 85, 89, 90
- [159] G. L. Lu-Yao, P. C. Albertsen, D. F. Moore, W. Shih, Y. Lin, R. S. DiPaola, M. J. Barry, A. Zietman, M. O’Leary, E. Walker-Corkery, and S. L. Yao. Outcomes of localized prostate cancer following conservative management. *JAMA*, 302(11):1202–1209, Sep 2009. 3
- [160] D. Lv, X. Guo, X. Wang, J. Zhang, and J. Fang. Computerized characterization of prostate cancer by fractal analysis in MR images. *J Magn Reson Imaging*, 30(1):161–168, Jul 2009. 24, 31, 33, 40, 53, 54, 60, 71, 72, 85, 89, 98

REFERENCES

- [161] R. W. Ma and K. Chapman. A systematic review of the effect of diet in prostate cancer prevention and treatment. *J Hum Nutr Diet*, 22(3):187–199, Jun 2009. 3
- [162] A. Madabhushi and J. K. Udupa. New methods of MR image intensity standardization via generalized scale. *Med Phys*, 33(9):3426–3434, Sep 2006. 33
- [163] A. Madabhushi, J. Udupa, and A. Souza. Generalized scale: Theory, algorithms, and application to image inhomogeneity correction . *Computer Vision and Image Understanding*, 101(2):100 – 121, 2006. ISSN 1077-3142. 31
- [164] J. B. Maintz and M. A. Viergever. A survey of medical image registration. *Med Image Anal*, 2(1):1–36, Mar 1998. 45
- [165] S. Mallat. *A wavelet tour of signal processing, Third Edition: The sparse way*. Academic Press, 3rd edition, 2008. ISBN 0123743702, 9780123743701. 28
- [166] S. G. Mallat and Z. Zhang. Matching pursuits with time-frequency dictionaries. *Signal Processing, IEEE Transactions on*, 41(12):3397–3415, 1993. 70
- [167] J. V. Manjon, J. Carbonell-Caballero, J. J. Lull, G. Garcia-Marti, L. Marti-Bonmati, and M. Robles. MRI denoising using non-local means. *Med Image Anal*, 12(4):514–523, Aug 2008. 26
- [168] L. Matulewicz, J. F. Jansen, L. Bokacheva, H. A. Vargas, O. Akin, S. W. Fine, A. Shukla-Dave, J. A. Eastham, H. Hricak, J. A. Koutcher, and K. L. Zakian. Anatomic segmentation improves prostate cancer detection with artificial neural networks analysis of ^1H magnetic resonance spectroscopic imaging. *Journal of Magnetic Resonance Imaging*, pages n/a–n/a, 2013. ISSN 1522-2586. 24, 40, 44, 51, 54, 59, 63, 72, 82, 85, 90

- [169] S. Mazzetti, M. De Luca, C. Bracco, A. Vignati, V. Giannini, M. Stasi, F. Russo, E. Armando, S. Agliozzo, and D. Regge. A CAD system based on multi-parametric analysis for cancer prostate detection on DCE-MRI. In *Proc. SPIE 7963, Medical Imaging 2011: Computer-Aided Diagnosis*, pages 79633Q–79633Q–7, 2011. 24, 51, 54, 60, 62, 72, 75, 84, 85, 89, 90
- [170] J. E. McNeal. The zonal anatomy of the prostate. *Prostate*, 2:35–49, 1981. 1
- [171] J. E. McNeal, E. A. Redwine, F. S. Freiha, and T. A. Stamey. Zonal distribution of prostatic adenocarcinoma. Correlation with histologic pattern and direction of spread. *Am. J. Surg. Pathol.*, 12(12):897–906, Dec 1988. 3
- [172] R. Meng, S. D. Chang, E. C. Jones, S. L. Goldenberg, and P. Kozlowski. Comparison between population average and experimentally measured arterial input function in predicting biopsy results in prostate cancer. *Academic radiology*, 17(4):520–525, 2010. doi: 10.1016/j.acra.2009.11.006. 113, 115
- [173] C. E. Metz. Receiver operating characteristic analysis: a tool for the quantitative evaluation of observer performance and imaging systems. *J Am Coll Radiol*, 3(6):413–422, Jun 2006. 86
- [174] J. Mitra. *Multimodal image registration applied to magnetic resonance and ultrasound prostatic images*. PhD thesis, Universitat de Girona and Université de Bourgogne, 2012. 49
- [175] J. Mitra, R. Marti, A. Oliver, X. Llado, J. C. Vilanova, and F. Meriaudeau. A comparison of thin-plate splines with automatic correspondences and B-splines with uniform grids for multimodal prostate registration. In *Society of Photo-Optical Instrumentation Engineers (SPIE) Conference Series*, volume 7964 of *Society of Photo-Optical Instrumentation Engineers (SPIE) Conference Series*, Mar. 2011. 47
- [176] J. Mitra, Z. Kato, R. Marti, A. Oliver, X. Llado, D. Sidibe, S. Ghose, J. C. Vilanova, J. Comet, and F. Meriaudeau. A spline-based non-linear diffeomorphism for multimodal prostate registration. *Med Image Anal*, 16(6):1259–1279, Aug 2012. 47

REFERENCES

- [177] J. Mohan, V. Krishnaveni, and Y. Guo. A survey on the magnetic resonance image denoising methods. *Biomedical Signal Processing and Control*, 9(0): 56 – 69, 2014. ISSN 1746-8094. 26
- [178] C. M. Moore, A. Ridout, and M. Emberton. The role of MRI in active surveillance of prostate cancer. *Curr Opin Urol*, 23(3):261–267, May 2013. 5
- [179] R. Morgan, A. Boxall, A. Bhatt, M. Bailey, R. Hindley, S. Langley, H. C. Whitaker, D. E. Neal, M. Ismail, H. Whitaker, N. Annels, A. Michael, and H. Pandha. Engrailed-2 (EN2): a tumor specific urinary biomarker for the early diagnosis of prostate cancer. *Clin. Cancer Res.*, 17(5):1090–1098, Mar 2011. 5
- [180] J. A. Nelder and R. Mead. A simplex method for function minimization. *The Computer Journal*, 7(4):308–313, 1965. 35
- [181] E. Niaf, O. Rouvire, and C. Lartizien. Computer-aided diagnosis for prostate cancer detection in the peripheral zone via multisequence MRI. In *Proc. SPIE 7963, Medical Imaging 2011: Computer-Aided Diagnosis*, 2011. xv, 24, 34, 35, 40, 44, 53, 54, 55, 56, 58, 60, 62, 64, 65, 66, 71, 72, 73, 75, 80, 84, 85, 89, 92
- [182] E. Niaf, O. Rouviere, F. Mege-Lechevallier, F. Bratan, and C. Lartizien. Computer-aided diagnosis of prostate cancer in the peripheral zone using multiparametric MRI. *Phys Med Biol*, 57(12):3833–3851, Jun 2012. xv, 24, 34, 35, 40, 44, 53, 54, 55, 56, 58, 60, 62, 64, 65, 66, 71, 72, 73, 75, 80, 84, 85, 89, 92
- [183] M. Noguchi, T. A. Stamey, J. E. McNeal, and C. M. Yemoto. Relationship between systematic biopsies and histological features of 222 radical prostatectomy specimens: lack of prediction of tumor significance for men with nonpalpable prostate cancer. *J. Urol.*, 166(1):104–109, Jul 2001. 5
- [184] R. Nowak. Wavelet-based Rician noise removal for magnetic resonance imaging. *Image Processing, IEEE Transactions on*, 8(10):1408–1419, 1999. ISSN 1057-7149. 26, 28

- [185] L. G. Nyul and J. K. Udupa. On standardizing the MR image intensity scale. *Magn Reson Med*, 42(6):1072–1081, Dec 1999. 32
- [186] L. G. Nyul, J. K. Udupa, and X. Zhang. New variants of a method of MRI scale standardization. *IEEE Trans Med Imaging*, 19(2):143–150, Feb 2000. xv, 33, 34, 98
- [187] T. Ojala, M. Pietikäinen, and D. Harwood. A comparative study of texture measures with classification based on featured distributions. *Pattern Recognition*, 29(1):51–59, Jan. 1996. ISSN 00313203. 41, 59
- [188] M. Osorio-Garcia, A. Croitor Sava, D. M. Sima, F. Nielsen, U. Himmelreich, and S. Van Huffel. *Magnetic Resonance Spectroscopy*, chapter Quantification improvements of ^1H MRS Signals, pages 1–27. InTech, March 2012. 35, 36, 39
- [189] G. Oster, L. Lamerato, A. G. Glass, K. E. Richert-Boe, A. Lopez, K. Chung, A. Richhariya, T. Dodge, G. G. Wolff, A. Balakumaran, and J. Edelsberg. Natural history of skeletal-related events in patients with breast, lung, or prostate cancer and metastases to bone: a 15-year study in two large US health systems. *Support Care Cancer*, 21(12):3279–3286, Dec 2013. 3
- [190] N. Otsu. A threshold selection method from gray-level histograms. *Automatica*, 11(285-296):23–27, 1975. 43
- [191] S. Ozer, M. Haider, D. L. Langer, T. H. Van der Kwast, A. Evans, M. Wernick, J. Trachtenberg, and I. Yetik. Prostate cancer localization with multispectral MRI based on Relevance Vector Machines. In *Biomedical Imaging: From Nano to Macro, 2009. ISBI '09. IEEE International Symposium on*, pages 73–76, 2009. 25, 27, 32, 40, 44, 51, 53, 54, 55, 62, 72, 80, 84, 85, 90, 97
- [192] S. Ozer, D. L. Langer, X. Liu, M. A. Haider, T. H. van der Kwast, A. J. Evans, Y. Yang, M. N. Wernick, and I. S. Yetik. Supervised and unsupervised methods for prostate cancer segmentation with multispectral MRI. *Med*

REFERENCES

- Phys*, 37(4):1873–1883, Apr 2010. 25, 27, 32, 40, 44, 51, 53, 54, 55, 62, 72, 80, 84, 85, 90, 91, 97
- [193] A. R. Padhani. Dynamic contrast-enhanced MRI in clinical oncology: current status and future directions. *J Magn Reson Imaging*, 16(4):407–422, Oct 2002. 11
- [194] A. R. Padhani. Integrating multiparametric prostate MRI into clinical practice. *Cancer Imaging*, 11 Spec No A:27–37, 2011. 15
- [195] S. Parfait. *Classification de spectres et recherche de biomarqueurs en spectroscopie par résonnance magnétique nucléaire du proton dans les tumeurs prostatiques*. PhD thesis, Université de Bourgogne, 2010. 1, 4, 18
- [196] S. Parfait, P. Walker, G. Change, X. Tizon, and J. Mitran. Classification of prostate magnetic resonance spectra using Support Vector Machine . *Biomedical Signal Processing and Control*, 7(5):499 – 508, 2012. ISSN 1746-8094. 25, 35, 38, 39, 40, 51, 54, 63, 72, 80, 82, 84, 85, 90
- [197] G. J. Parker, C. Roberts, A. Macdonald, G. A. Buonaccorsi, S. Cheung, D. L. Buckley, A. Jackson, Y. Watson, K. Davies, and G. C. Jayson. Experimentally-derived functional form for a population-averaged high-temporal-resolution arterial input function for dynamic contrast-enhanced mri. *Magnetic resonance in medicine*, 56(5):993–1000, 2006. doi: 10.1002/mrm.21066. 115
- [198] Y. C. Pati, R. Rezaifar, and P. Krishnaprasad. Orthogonal matching pursuit: Recursive function approximation with applications to wavelet decomposition. In *Signals, Systems and Computers, 1993. 1993 Conference Record of The Twenty-Seventh Asilomar Conference on*, pages 40–44. IEEE, 1993. 70
- [199] K. Pearson. On lines and planes of closest fit to systems of points in space. *Philosophical Magazine*, 2(6):559–572, 1901. 42

- [200] H. Peng, F. Long, and C. Ding. Feature selection based on mutual information criteria of max-dependency, max-relevance, and min-redundancy. *Pattern Analysis and Machine Intelligence, IEEE Transactions on*, 27(8):1226–1238, 2005. ISSN 0162-8828. 66
- [201] Y. Peng, Y. Jiang, C. Yang, J. Brown, T. Antic, I. Sethi, C. Schmid-Tannwald, M. Giger, S. Eggener, and A. Oto. Quantitative analysis of multiparametric prostate MR images: differentiation between prostate cancer and normal tissue and correlation with Gleason score—a computer-aided diagnosis development study. *Radiology*, 267(1):787–796, June 2013. 16, 20, 25, 53, 54, 58, 72, 80, 84, 85, 89, 90, 91
- [202] N. Petrick, M. Haider, R. M. Summers, S. C. Yeshwant, L. Brown, E. M. Iuliano, A. Louie, J. R. Choi, and P. J. Pickhardt. CT colonography with computer-aided detection as a second reader: observer performance study. *Radiology*, 246(1):148–156, Jan 2008. 6
- [203] W. Pijnappel, A. van den Boogaart, R. de Beer, and D. van Ormondt. SVD-based quantification of magnetic resonance signals . *Journal of Magnetic Resonance (1969)*, 97(1):122 – 134, 1992. ISSN 0022-2364. 36, 37
- [204] A. Pizurica. *Image denoising using wavelets and spatial context modeling*. PhD thesis, Universiteit Gent, 2002. 28
- [205] A. Pizurica, W. Philips, I. Lemahieu, and M. Acheroy. A versatile wavelet domain noise filtration technique for medical imaging. *IEEE Trans Med Imaging*, 22(3):323–331, Mar 2003. 28
- [206] J. Pluim, J. Maintz, and M. Viergever. Mutual-information-based registration of medical images: a survey. *IEEE Transcations on Medical Imaging*, 22(8):986–1004, 2003. 48
- [207] J. Prewitt. *Picture processing and psychohistories*, chapter Object enhancement and extraction. Academic Press, 1970. 55
- [208] S. W. Provencher. Estimation of metabolite concentrations from localized in vivo proton NMR spectra. *Magn Reson Med*, 30(6):672–679, Dec 1993. 63

REFERENCES

- [209] P. Puech, N. Betrouni, N. Makni, A. S. Dewalle, A. Villers, and L. Lemaitre. Computer-assisted diagnosis of prostate cancer using DCE-MRI data: design, implementation and preliminary results. *Int J Comput Assist Radiol Surg*, 4(1):1–10, Jan 2009. 25, 40, 44, 54, 60, 71, 72, 74, 84, 89, 90
- [210] J. Quinlan. Induction of decision trees. *Machine Learning*, 1(1):81–106, 1986. ISSN 0885-6125. 75
- [211] J. Quinlan. *C4.5: Programs for machine learning*. Morgan Kaufmann Publishers Inc., San Francisco, CA, USA, 1993. ISBN 1-55860-238-0. 75
- [212] J. Quinonero-Candela, A. Girard, and C. Rasmussen. Prediction at an Uncertain Input for Gaussian processes and relevance vector machines application to Multiple-Step ahead time-series forecasting. Technical report, DTU Informatics, 2002. 80
- [213] L. E. Quint, J. S. Van Erp, P. H. Bland, S. H. Mandell, E. A. Del Buono, H. B. Grossman, G. M. Glazer, and P. W. Gikas. Carcinoma of the prostate: MR images obtained with body coils do not accurately reflect tumor volume. *AJR Am J Roentgenol*, 156(3):511–516, Mar 1991. 10
- [214] A. Rampun, P. Malcolm, and R. Zwiggelaar. Detection and localisation of prostate cancer within the peripheral zone using scoring algorithm. In *Irish Machine Vision and Image Processing*, 2014. 41
- [215] A. Rampun, L. Zheng, P. Malcolm, and R. Zwiggelaar. Classifying benign and malignant tissues within the prostate peripheral zone using textons. In *Medical Image Understanding and Analysis (MIUA 2015)*, 2015. 25, 27, 32, 40, 41, 44, 51, 53, 55, 64, 70, 72, 75, 76, 84, 85, 92
- [216] A. Rampun, L. Zheng, P. Malcolm, and R. Zwiggelaar. Computer aided diagnosis of prostate cancer within the peripheral zone in t2-weighted mri. In *Medical Image Understanding and Analysis (MIUA 2015)*, 2015. 32, 40, 41, 44, 51, 53, 55, 56, 58, 64, 72, 74, 75, 76, 84, 85, 92

- [217] A. Rampun, B. Tiddeman, R. Zwiggelaar, and P. Malcolm. Computer aided diagnosis of prostate cancer: A texton based approach. *Medical Physics*, 43(10):5412–5425, 2016. 25, 27, 32, 40, 41, 44, 51, 53, 55, 64, 70, 71, 72, 75, 76, 84, 85, 89, 91, 92
- [218] A. Rampun, L. Wang, P. Malcolm, and R. Zwiggelaar. A quantitative study of texture features across different window sizes in prostate t2-weighted mri. *Procedia Computer Science*, 90:74–79, 2016. 25, 27, 32, 40, 41, 44, 51, 53, 55, 56, 58, 84, 85
- [219] A. Rampun, L. Zheng, P. Malcolm, B. Tiddeman, and R. Zwiggelaar. Computer-aided detection of prostate cancer in t2-weighted mri within the peripheral zone. *Physics in medicine and biology*, 61(13):4796–4825, 2016. 25, 27, 32, 40, 41, 44, 51, 53, 55, 56, 58, 64, 72, 75, 76, 82, 84, 85, 89, 92
- [220] C. Rasmussen and C. Williams. *Gaussian processes for machine learning*. The MIT Press, 2005. ISBN 026218253X. 78
- [221] H. Ratiney, M. Sdika, Y. Coenradie, S. Cavassila, D. van Ormondt, and D. Graveron-Demilly. Time-domain semi-parametric estimation based on a metabolite basis set. *NMR Biomed*, 18(1):1–13, Feb 2005. 63
- [222] I. Rish. An empirical study of the naive Bayes classifier. In *IJCAI 2001 workshop on empirical methods in artificial intelligence*, volume 3, pages 41–46, 2001. 74
- [223] C. Rodriguez, S. J. Freedland, A. Deka, E. J. Jacobs, M. L. McCullough, A. V. Patel, M. J. Thun, and E. E. Calle. Body mass index, weight change, and risk of prostate cancer in the Cancer Prevention Study II Nutrition Cohort. *Cancer Epidemiol. Biomarkers Prev.*, 16(1):63–69, Jan 2007. 3
- [224] A. B. Rosenkrantz, A. Sabach, J. S. Babb, B. W. Matza, S. S. Taneja, and F. M. Deng. Prostate cancer: comparison of dynamic contrast-enhanced MRI techniques for localization of peripheral zone tumor. *AJR Am J Roentgenol*, 201(3):W471–478, Sep 2013. 13

REFERENCES

- [225] S. T. Roweis and L. K. Saul. Nonlinear dimensionality reduction by locally linear embedding. *Science*, 290(5500):2323–2326, 2000. 68
- [226] R. Rubinstein, M. Zibulevsky, and M. Elad. Efficient implementation of the k-svd algorithm using batch orthogonal matching pursuit. *CS Technion*, 40(8):1–15, 2008. 69
- [227] D. Rueckert, L. I. Sonoda, C. Hayes, D. L. Hill, M. O. Leach, and D. J. Hawkes. Nonrigid registration using free-form deformations: application to breast MR images. *IEEE Trans Med Imaging*, 18(8):712–721, Aug 1999. 50
- [228] D. E. Rumelhart, G. E. Hinton, and R. J. Williams. Learning internal representations by error propagation. In J. A. Anderson and E. Rosenfeld, editors, *Neurocomputing: foundations of research*, chapter Learning Internal Representations by Error Propagation, pages 673–695. MIT Press, Cambridge, MA, USA, 1988. ISBN 0-262-01097-6. 82
- [229] Y. Saeys, I. Inza, and P. Larrañaga. A review of feature selection techniques in bioinformatics. *Bioinformatics*, 23(19):2507–2517, 2007. 65
- [230] G. Samarasinghe, A. Sowmya, and D. A. Moses. Semi-quantitative analysis of prostate perfusion mri by clustering of pre and post contrast enhancement phases. In *Biomedical Imaging (ISBI), 2016 IEEE 13th International Symposium on*, pages 943–947. IEEE, 2016. 25, 27, 34, 40, 54, 60, 72, 76, 85, 90
- [231] M. C. Schabel and D. L. Parker. Uncertainty and bias in contrast concentration measurements using spoiled gradient echo pulse sequences. *Physics in medicine and biology*, 53(9):2345, 2008. doi: 10.1088/0031-9155/53/9/010. 114
- [232] J. Scheidler, H. Hricak, D. B. Vigneront, K. K. Yu, D. L. Sokolov, L. R. Huang, C. J. Zaloudek, S. J. Nelson, P. R. Carroll, and J. Kurhanewicz. Prostate cancer: localization with three-dimensional proton MR spectroscopic imaging–clinicopathologic study. *Radiology*, 213(2):473–480, Nov 1999. 19

- [233] J. Scheidler, R. Petsch, U. Muller-Lisse, A. Heuck, and M. Reiser. Echo-planar diffusion-weighted MR imaging of the prostate. In *Proceedings of the 7th Annual Meeting of ISMRM Philadelphia*, page 1103, 1999. 7, 10, 14
- [234] H. P. Schlemmer, J. Merkle, R. Grobholz, T. Jaeger, M. S. Michel, A. Werner, J. Rabe, and G. van Kaick. Can pre-operative contrast-enhanced dynamic MR imaging for prostate cancer predict microvessel density in prostatectomy specimens? *Eur Radiol*, 14(2):309–317, Feb 2004. 13
- [235] F. H. Schroder, H. B. Carter, T. Wolters, R. C. van den Bergh, C. Gosselaar, C. H. Bangma, and M. J. Roobol. Early detection of prostate cancer in 2007. Part 1: PSA and PSA kinetics. *Eur. Urol.*, 53(3):468–477, Mar 2008. 5
- [236] F. H. Schröder, J. Hugosson, M. J. Roobol, T. L. Tammela, S. Ciatto, V. Neelen, M. Kwiatkowski, M. Lujan, H. Lilja, M. Zappa, L. J. Denis, F. Recker, A. Pez, L. Määttänen, C. H. Bangma, G. Aus, S. Carlsson, A. Villers, X. Rebillard, T. van der Kwast, P. M. Kujala, B. G. Blijenberg, U.-H. Stenman, A. Huber, K. Taari, M. Hakama, S. M. Moss, H. J. de Koning, and A. Auvinen. Prostate-cancer mortality at 11 years of follow-up. *New England Journal of Medicine*, 366(11):981–990, 2012. 4, 5
- [237] D. Shanbhag, S. N. Gupta, K. Rajamani, Y. Zhu, and R. Mullick. A generalized methodology for detection of vascular input function with dynamic contrast enhanced perfusion data. In *ISMRM*, volume 12, page 10, 2012. 113
- [238] L. G. Shapiro and G. C. Stockman. *Computer vision*. Prentice Hall, Upper Saddle River, NJ, 2001. ISBN 0-13-030796-3. 31
- [239] J. Shi and J. Malik. Normalized cuts and image segmentation. *Pattern Analysis and Machine Intelligence, IEEE Transactions on*, 22(8):888–905, 2000. ISSN 0162-8828. 43, 68
- [240] R. Shimofusa, H. Fujimoto, H. Akamata, K. Motoori, S. Yamamoto, T. Ueda, and H. Ito. Diffusion-weighted imaging of prostate cancer. *J Comput Assist Tomogr*, 29(2):149–153, 2005. 15

REFERENCES

- [241] R. Siegel, D. Naishadham, and A. Jemal. Cancer statistics, 2013. *CA Cancer J Clin*, 63(1):11–30, Jan 2013. 3
- [242] J. Sivic and A. Zisserman. Video google: a text retrieval approach to object matching in videos. In *IEEE ICCV*, pages 1470–1477, 2003. 70
- [243] J. G. Sled, A. P. Zijdenbos, and A. C. Evans. A nonparametric method for automatic correction of intensity nonuniformity in MRI data. *IEEE Trans Med Imaging*, 17(1):87–97, Feb 1998. 30, 31
- [244] I. Sobel. Camera models and machine perception. Technical report, DTIC Document, 1970. 55
- [245] D. M. Somford, J. J. Futterer, T. Hambrock, and J. O. Barentsz. Diffusion and perfusion MR imaging of the prostate. *Magn Reson Imaging Clin N Am*, 16(4):685–695, Nov 2008. 14
- [246] D. C. Sorensen. Newton’s method with a model trust region modification. *SIAM Journal on Numerical Analysis*, 19(2):409–426, 1982. doi: 10.1137/0719026. 115, 117
- [247] D. F. Specht. Probabilistic neural networks for classification, mapping, or associative memory. In *Neural Networks, 1988., IEEE International Conference on*, pages 525–532 vol.1, 1988. 82
- [248] A. Srivastava, E. Klassen, S. Joshi, and I. Jermyn. Shape analysis of elastic curves in euclidean spaces. *Pattern Analysis and Machine Intelligence, IEEE Transactions on*, 33(7):1415–1428, July 2011. 100, 101
- [249] K. S. St Lawrence and T. Y. Lee. An adiabatic approximation to the tissue homogeneity model for water exchange in the brain: I. Theoretical derivation. *J. Cereb. Blood Flow Metab.*, 18(12):1365–1377, Dec 1998. 13
- [250] T. A. Stamey, A. N. Donaldson, C. E. Yemoto, J. E. McNeal, S. Sozen, and H. Gill. Histological and clinical findings in 896 consecutive prostates treated only with radical retropubic prostatectomy: epidemiologic significance of annual changes. *J. Urol.*, 160(6 Pt 2):2412–2417, Dec 1998. 3

- [251] M. Staring, U. A. van der Heide, S. Klein, M. A. Viergever, and J. P. Pluim. Registration of cervical MRI using multifeature mutual information. *IEEE Trans Med Imaging*, 28(9):1412–1421, Sep 2009. 48
- [252] G. D. Steinberg, B. S. Carter, T. H. Beaty, B. Childs, and P. C. Walsh. Family history and the risk of prostate cancer. *Prostate*, 17(4):337–347, 1990. 3
- [253] S. Strum and D. Pogliano. What every doctor who treats male patients should know. PCRI Insights vol. 8, no. 2, May 2005. 3
- [254] M. Styner and G. Gerig. Evaluation of 2D/3D bias correction with 1+1ES-optimization. Technical report, ETH Zürich, 1997. 30
- [255] M. Styner, C. Brechbuhler, G. Szckely, and G. Gerig. Parametric estimate of intensity inhomogeneities applied to MRI. *Medical Imaging, IEEE Transactions on*, 19(3):153–165, 2000. ISSN 0278-0062. 29
- [256] Y. S. Sung, H. J. Kwon, B. W. Park, G. Cho, C. K. Lee, K. S. Cho, and J. K. Kim. Prostate cancer detection on dynamic contrast-enhanced MRI: computer-aided diagnosis versus single perfusion parameter maps. *AJR Am J Roentgenol*, 197(5):1122–1129, Nov 2011. 25, 51, 54, 60, 62, 72, 80, 85, 90
- [257] M. G. Swanson, D. B. Vigneron, T. K. Tran, N. Sailasuta, R. E. Hurd, and J. Kurhanewicz. Single-voxel oversampled J-resolved spectroscopy of in vivo human prostate tissue. *Magn Reson Med*, 45(6):973–980, Jun 2001. 7
- [258] A. V. Taira, G. S. Merrick, R. W. Galbreath, H. Andreini, W. Taubenslag, R. Curtis, W. M. Butler, E. Adamovich, and K. E. Wallner. Performance of transperineal template-guided mapping biopsy in detecting prostate cancer in the initial and repeat biopsy setting. *Prostate Cancer Prostatic Dis.*, 13(1):71–77, Mar 2010. 5
- [259] H. Tamura, S. Mori, and T. Yamawaki. Textural features corresponding to visual perception. *IEEE Transactions on Systems, Man, and Cybernetics*, 8(6):460–473, 1978. 56

REFERENCES

- [260] M. Tipping. Sparse Bayesian learning and the relevance vector machine. *Journal of Machine Learning Research*, 1:211–244, 2001. 80
- [261] P. Tiwari, A. Madabhushi, and M. Rosen. A hierarchical unsupervised spectral clustering scheme for detection of prostate cancer from magnetic resonance spectroscopy (MRS). *Med Image Comput Comput Assist Interv*, 10 (Pt 2):278–286, 2007. 25, 51, 54, 63, 64, 68, 71, 72, 92
- [262] P. Tiwari, M. Rosen, and A. Madabhushi. Consensus-locally linear embedding (C-LLE): application to prostate cancer detection on magnetic resonance spectroscopy. *Med Image Comput Comput Assist Interv*, 11(Pt 2): 330–338, 2008. 25, 51, 54, 64, 67, 69, 72, 73, 85, 90, 92
- [263] P. Tiwari, M. Rosen, and A. Madabhushi. A hierarchical spectral clustering and nonlinear dimensionality reduction scheme for detection of prostate cancer from magnetic resonance spectroscopy (MRS). *Med Phys*, 36(9):3927–3939, Sep 2009. 25, 43, 44, 51, 54, 63, 64, 67, 68, 71, 72, 84, 85, 92
- [264] P. Tiwari, M. Rosen, G. Reed, J. Kurhanewicz, and A. Madabhushi. Spectral embedding based probabilistic boosting tree (ScEPTre): classifying high dimensional heterogeneous biomedical data. *Med Image Comput Comput Assist Interv*, 12(Pt 2):844–851, 2009. 25, 51, 53, 54, 55, 56, 58, 63, 64, 68, 78, 84, 85, 89, 90, 91
- [265] P. Tiwari, J. Kurhanewicz, M. Rosen, and A. Madabhushi. Semi supervised multi kernel (SeSMiK) graph embedding: identifying aggressive prostate cancer via magnetic resonance imaging and spectroscopy. *Med Image Comput Comput Assist Interv*, 13(Pt 3):666–673, 2010. 25, 51, 53, 54, 55, 56, 58, 63, 64, 72, 78, 84, 85, 89, 92
- [266] P. Tiwari, S. Viswanath, J. Kurhanewicz, A. Sridhar, and A. Madabhushi. Multimodal wavelet embedding representation for data combination (MaWERiC): integrating magnetic resonance imaging and spectroscopy for prostate cancer detection. *NMR Biomed*, 25(4):607–619, Apr 2012. 25, 38, 39, 40, 51, 53, 54, 56, 60, 64, 67, 72, 76, 78, 80, 84, 85, 89, 91, 92

- [267] P. Tiwari, J. Kurhanewicz, and A. Madabhushi. Multi-kernel graph embedding for detection, Gleason grading of prostate cancer via MRI/MRS. *Med Image Anal*, 17(2):219–235, Feb 2013. 25, 51, 53, 54, 55, 56, 58, 63, 68, 72, 76, 84, 85, 88, 89, 91, 92
- [268] P. Tofts. T1-weighted DCE imaging concepts: modelling, acquisition and analysis. In *Magneton Flash*. Siemens, 2010. 13, 20
- [269] P. S. Tofts. Modeling tracer kinetics in dynamic Gd-DTPA MR imaging. *J Magn Reson Imaging*, 7(1):91–101, 1997. 13, 62
- [270] P. S. Tofts, B. Berkowitz, and M. D. Schnall. Quantitative analysis of dynamic gd-dtpa enhancement in breast tumors using a permeability model. *Magnetic Resonance in Medicine*, 33(4):564–568, 1995. doi: 10.1002/mrm.1910330416. 105
- [271] R. Toth, J. Chappelow, M. Rosen, S. Pungavkar, A. Kalyanpur, and A. Madabhushi. Multi-attribute non-initializing texture reconstruction based active shape model (MANTRA). *Med Image Comput Comput Assist Interv*, 11(Pt 1):653–661, 2008. 42, 47
- [272] R. Toth, S. Doyle, S. Pungavkar, A. Kalyanpur, and A. Madabhushi. A boosted ensemble scheme for accurate landmark detection for active shape models. In *SPIE Medical Imaging*, volume 7260, Orlando, FL, 2009. 42, 47
- [273] R. Trigui, J. Miteran, L. Sellami, P. Walker, and A. B. Hamida. A classification approach to prostate cancer localization in 3t multi-parametric mri. In *Advanced Technologies for Signal and Image Processing (ATSIP), 2016 2nd International Conference on*, pages 113–118. IEEE, 2016. 25, 35, 38, 39, 40, 44, 51, 53, 54, 55, 56, 60, 63, 72, 76, 82, 84, 85, 90, 91
- [274] R. Trigui, J. Mit  ran, P. Walker, L. Sellami, and A. B. Hamida. Automatic classification and localization of prostate cancer using multi-parametric mri/mrs. *Biomedical Signal Processing and Control*, 31:189–198, 2017. 25, 35, 38, 39, 40, 44, 51, 53, 54, 55, 60, 63, 72, 76, 80, 82, 84, 85, 90, 91

REFERENCES

- [275] Z. Tu. Probabilistic boosting-tree: learning discriminative models for classification, recognition, and clustering. In *Computer Vision, 2005. ICCV 2005. Tenth IEEE International Conference on*, volume 2, pages 1589–1596 Vol. 2, 2005. 76
- [276] J. D. Tucker, W. Wu, and A. Srivastava. Generative models for functional data using phase and amplitude separation. *Computational Statistics & Data Analysis*, 61:50–66, 2013. 102
- [277] B. Turkbey and P. L. Choyke. Multiparametric MRI and prostate cancer diagnosis and risk stratification. *Curr Opin Urol*, 22(4):310–315, Jul 2012. 9
- [278] M. van der Graaf, R. G. Schipper, G. O. Oosterhof, J. A. Schalken, A. A. Verhofstad, and A. Heerschap. Proton MR spectroscopy of prostatic tissue focused on the detection of spermine, a possible biomarker of malignant behavior in prostate cancer. *MAGMA*, 10(3):153–159, Jul 2000. 18, 20
- [279] C. G. van Niekerk, J. A. van der Laak, M. E. Borger, H. J. Huisman, J. A. Witjes, J. O. Barentsz, and C. A. Hulsbergen-van de Kaa. Computerized whole slide quantification shows increased microvascular density in pT2 prostate cancer as compared to normal prostate tissue. *Prostate*, 69(1):62–69, Jan 2009. 12
- [280] C. G. van Niekerk, J. A. Witjes, J. O. Barentsz, J. A. van der Laak, and C. A. Hulsbergen-van de Kaa. Microvascularity in transition zone prostate tumors resembles normal prostatic tissue. *Prostate*, 73(5):467–475, Apr 2013. 12, 13
- [281] L. Vanhamme, A. van den Boogaart, and S. Van Huffel. Improved method for accurate and efficient quantification of MRS data with use of prior knowledge. *J. Magn. Reson.*, 129:35–45, 1997. 63
- [282] V. Vapnik and A. Lerner. Pattern Recognition using Generalized Portrait Method. *Automation and Remote Control*, 24, 1963. 79
- [283] S. Verma, A. Rajesh, J. J. Futterer, B. Turkbey, T. W. Scheenen, Y. Pang, P. L. Choyke, and J. Kurhanewicz. Prostate MRI and 3D MR spectroscopy: how we do it. *AJR Am J Roentgenol*, 194(6):1414–1426, Jun 2010. 20

- [284] S. Verma, B. Turkbey, N. Muradyan, A. Rajesh, F. Cornud, M. A. Haider, P. L. Choyke, and M. Harisinghani. Overview of dynamic contrast-enhanced MRI in prostate cancer diagnosis and management. *AJR Am J Roentgenol*, 198(6):1277–1288, Jun 2012. 12, 13, 20
- [285] J. C. Vilanova, J. Comet, C. Barceló-Vidal, J. Barceló, E. López-Bonet, A. Maroto, M. Arzoz, À. Moreno, and J. Areal. Peripheral zone prostate cancer in patients with elevated PSA levels and low free-to-total PSA ratio: detection with MR imaging and MR spectroscopy. *Radiology*, 253(1):135–143, 2009. 19
- [286] A. Villers, A. Steg, and L. Boccon-Gibod. Anatomy of the prostate: review of the different models. *Eur. Urol.*, 20:261–268, 1991. 1
- [287] P. Viola and W. M. Wells, III. Alignment by maximization of mutual information. *Int. J. Comput. Vision*, 24(2):137–154, Sept. 1997. ISSN 0920-5691. 49
- [288] S. Viswanath, B. N. Bloch, E. Genega, N. Rofsky, R. Lenkinski, J. Chappelow, R. Toth, and A. Madabhushi. A comprehensive segmentation, registration, and cancer detection scheme on 3 Tesla *in vivo* prostate DCE-MRI. *Med Image Comput Comput Assist Interv*, 11(Pt 1):662–669, 2008. 25, 42, 44, 49, 50, 51, 60, 63, 64, 73, 85, 90, 92
- [289] S. Viswanath, P. Tiwari, M. Rosen, and A. Madabhushi. A meta-classifier for detecting prostate cancer by quantitative integration of *In Vivo* magnetic resonance spectroscopy and magnetic resonance imaging. In *Medical Imaging 2008: Computer-Aided Diagnosis*, volume 6915. SPIE, 2008. 25, 51, 53, 54, 55, 56, 58, 60, 64, 68, 73, 85, 90, 92
- [290] S. Viswanath, B. N. Bloch, M. Rosen, J. Chappelow, R. Toth, N. Rofsky, R. Lenkinski, E. Genega, A. Kalyanpur, and A. Madabhushi. Integrating structural and functional imaging for computer assisted detection of prostate cancer on multi-protocol *in vivo* 3 Tesla MRI. In *Society of Photo-Optical Instrumentation Engineers (SPIE) Conference Series*, volume 7260 of *Society*

REFERENCES

- of Photo-Optical Instrumentation Engineers (SPIE) Conference Series*, Feb. 2009. 25, 29, 33, 40, 42, 44, 49, 50, 51, 53, 56, 58, 72, 76, 84, 85, 89
- [291] S. Viswanath, B. N. Bloch, J. Chappelow, P. Patel, N. Rofsky, R. Lenkinski, E. Genega, and A. Madabhushi. Enhanced multi-protocol analysis via intelligent supervised embedding (EMPrAvISE): detecting prostate cancer on multi-parametric MRI. In *Proc. SPIE 7963, Medical Imaging 2011: Computer-Aided Diagnosis*, 2011. 25, 33, 40, 44, 49, 50, 51, 53, 55, 56, 58, 64, 68, 72, 78, 83, 84, 85, 88, 89, 91
- [292] S. E. Viswanath, N. B. Bloch, J. C. Chappelow, R. Toth, N. M. Rofsky, E. M. Genega, R. E. Lenkinski, and A. Madabhushi. Central gland and peripheral zone prostate tumors have significantly different quantitative imaging signatures on 3 Tesla endorectal, *in vivo* T2-weighted MR imagery. *J Magn Reson Imaging*, 36(1):213–224, Jul 2012. 25, 30, 33, 40, 42, 51, 53, 56, 58, 66, 72, 74, 84, 85, 89, 92, 98
- [293] P. C. Vos, T. Hambrock, J. O. Barentsz, and H. J. Huisman. Combining T2-weighted with dynamic MR images for computerized classification of prostate lesions. In *Medical Imaging 2008: Computer-Aided Diagnosis*, volume 6915. SPIE, 2008. 25, 40, 44, 49, 50, 53, 55, 64, 72, 80, 84, 85, 89
- [294] P. C. Vos, T. Hambrock, C. A. Hulsbergen-van de Kaa, J. J. Futterer, J. O. Barentsz, and H. J. Huisman. Computerized analysis of prostate lesions in the peripheral zone using dynamic contrast enhanced MRI. *Med Phys*, 35(3):888–899, Mar 2008. 25, 40, 44, 53, 58, 72, 80, 85, 89
- [295] P. C. Vos, T. Hambrock, J. O. Barentsz, and H. J. Huisman. Computer-assisted analysis of peripheral zone prostate lesions using T2-weighted and dynamic contrast enhanced T1-weighted MRI. *Phys Med Biol*, 55(6):1719–1734, Mar 2010. 25, 44, 49, 50, 52, 53, 58, 72, 80, 84, 85, 89
- [296] P. C. Vos, J. O. Barentsz, N. Karssemeijer, and H. J. Huisman. Automatic computer-aided detection of prostate cancer based on multiparametric magnetic resonance image analysis. *Phys Med Biol*, 57(6):1527–1542, Mar 2012. 25, 43, 44, 51, 53, 58, 64, 65, 72, 73, 80, 84, 85

- [297] U. Vovk, F. Pernus, and B. Likar. A review of methods for correction of intensity inhomogeneity in MRI. *Medical Imaging, IEEE Transactions on*, 26(3):405–421, 2007. ISSN 0278-0062. 29
- [298] P. Walker, G. Crehange, S. Parfait, A. Cochet, P. Maignon, L. Cormier, and F. Brunotte. Absolute quantification in 1H MRSI of the prostate at 3T. In *ISMRM Annual Meeting 2010*, 2010. 19
- [299] L. Wang, Y. Mazaheri, J. Zhang, N. M. Ishill, K. Kuroiwa, and H. Hricak. Assessment of biologic aggressiveness of prostate cancer: correlation of MR signal intensity with Gleason grade after radical prostatectomy. *Radiology*, 246(1):168–176, Jan 2008. 10, 20
- [300] S. K. Warfield, K. H. Zou, and W. M. Wells. Simultaneous truth and performance level estimation (STAPLE): an algorithm for the validation of image segmentation. *IEEE Trans Med Imaging*, 23(7):903–921, Jul 2004. 41
- [301] M. Wiart, L. Curiel, A. Gelet, D. Lyonnet, J. Y. Chapelon, and O. Rouviere. Influence of perfusion on high-intensity focused ultrasound prostate ablation: a first-pass MRI study. *Magn Reson Med*, 58(1):119–127, Jul 2007. 34
- [302] L. Ye, H. G. Kynaston, and W. G. Jiang. Bone metastasis in prostate cancer: molecular and cellular mechanisms (Review). *Int. J. Mol. Med.*, 20(1):103–111, Jul 2007. 3
- [303] B. Zelhof, M. Lowry, G. Rodrigues, S. Kraus, and L. Turnbull. Description of magnetic resonance imaging-derived enhancement variables in pathologically confirmed prostate cancer and normal peripheral zone regions. *BJU Int.*, 104(5):621–627, Sep 2009. 13
- [304] G. Zhao, T. Ahonen, J. Matas, and M. Pietikainen. Rotation-Invariant Image and Video Description With Local Binary Pattern Features. *Image Processing, IEEE Transactions on*, 21(4):1465–1477, 2012. ISSN 1057-7149. 59

REFERENCES

- [305] H. Zhu, R. Ouwerkerk, and P. B. Barker. Dual-band water and lipid suppression for MR spectroscopic imaging at 3 Tesla. *Magn Reson Med*, 63(6):1486–1492, Jun 2010. 36
- [306] Y. Zhu, M.-C. Chang, and S. Gupta. Automated determination of arterial input function for dce-mri of the prostate. In *SPIE Medical Imaging*, pages 79630W–79630W. International Society for Optics and Photonics, 2011. doi: 10.1117/12.878213. 113
- [307] B. Zitová and J. Flusser. Image registration methods: a survey. *Image and Vision Computing*, 21(11):977 – 1000, 2003. ISSN 0262-8856. 45

Declaration

I herewith declare that I have produced this paper without the prohibited assistance of third parties and without making use of aids other than those specified; notions taken over directly or indirectly from other sources have been identified as such. This paper has not previously been presented in identical or similar form to any other German or foreign examination board.

The thesis work was conducted from XXX to YYY under the supervision of PI at ZZZ.

CITY,